Universität Rostock

Traditio et Innovatio

Wave-Induced Vertical Turbulent Transport of a Passive Scalar Above Permeable Rippled Seabeds

Dissertation

zur Erlangung des akademischen Grades

Doktor-Ingenieur (Dr.-Ing.)

der Fakultät für Maschinenbau und Schiffstechnik

der Universität Rostock

vorgelegt von

Leonie Kandler

Rostock, 2024

https://doi.org/10.18453/rosdok_id00004804

Lehrstuhl Strömungsmechanik | Universität Rostock

1. Gutachter:	Prof. Dr.-Ing. habil. Sven Grundmann Lehrstuhl Strömungsmechanik, Universität Rostock
2. Gutachter:	Prof. Dr. rer. nat. habil. Hans Burchard Leibniz-Institut für Ostseeforschung Warnemünde
3. Gutachter:	Dr. rer. nat. Martin Brede Lehrstuhl Strömungsmechanik, Universität Rostock
Tag der Einreichung:	29. November 2024
Tag der Verteidigung:	02. April 2025

Abstract

Sandy sediments play a crucial role in shaping the ecological dynamics of coastal waters, acting as gateways for terrestrial and sediment-originated matter via submarine groundwater discharge (SGD) and pore water exchange. Under wave action, sand ripples form, shaping the seabed topography and significantly influencing solute transport, particularly through wave-topography interactions. This study investigates the complex interactions between rippled seabeds and wave conditions, examining their effects on the vertical transport of a discharging fluid. Using controlled wave tank experiments, the research replicates the transport processes of a tracer fluid emerging from various artificial rippled seabeds under different wave scenarios.

Synchronized particle image velocimetry (PIV) and laser-induced fluorescence (LIF) were employed to capture velocity and concentration fields, enabling a comprehensive analysis of vertical fluid transport near the sediment-water interface based on the spatial tracer fluid distribution, turbulent kinetic energy, vertical turbulent fluxes and turbulent mixing lengths. The study explores three key seabed characteristics: the general effects of rippled versus flat seabeds, the influence of the ripple shape, and the impact of ripple asymmetry. Additionally, three distinct wave scenarios were applied to assess the influence of varying wave conditions as a second variable.

The findings highlight the relationship between seabed topography and oscillating flow in driving turbulence generation, a key factor for influencing fluid transport and local concentration values. The results reveal that the transition from calm to stormy wave conditions significantly enhances the vertical transport of fluid above the rippled seabeds, surpassing the effects of minor topographical variations, such as changes in ripple shape or symmetry factor. Moreover, flow separation and vortex formation occurring at the downstream slope of the ripples under strong oscillating flow were identified as critical factors influencing tracer discharge patterns and vertical transport. The ripple shape and the symmetry factor were observed to impact the location and timing of flow separation, as well as the spatial extent of the separation vortices.

Notably, this research is the first to quantify vertical turbulent fluxes and turbulent mixing lengths specifically for tracer transport above permeable rippled seabeds, providing parameters for modelling this process in numerical simulations. The results underscore the importance of incorporating seabed topography into fluid dynamics and solute transport models. The implications of this study extend to environmental management, contributing to the refinement of models that predict the dispersion of pollutants and nutrients in coastal aquatic systems.

Kurzfassung

Sandige Sedimente spielen eine zentrale Rolle in der ökologischen Dynamik von Küstengewässern, da sie als Schnittstelle für den Transport von terrestrischen und sedimentgebundenen Stoffen durch submarinen Grundwasseraustritt (SGD) und Porenwasseraustausch dienen. Durch Welleneinwirkung entstehen Sandrippel, die die Topografie des Meeresbodens prägen, und durch ihre Wechselwirkung mit Wellen den Stofftransport beeinflussen. In der vorliegenden Studie werden die komplexen Interaktionen zwischen Bodenrippeln und unterschiedlichen Wellenbedingungen untersucht, um deren Auswirkungen auf den Vertikaltransport von austretenden Fluiden zu analysieren. Mithilfe von Wellenkanalexperimenten wurde der Transport einer Tracerflüssigkeit, die aus unterschiedlichen künstlichen Bodenrippeln austritt, unter verschiedenen Wellenszenarien nachgebildet.
Zur Erfassung von Geschwindigkeits- und Konzentrationsfeldern wurden synchron Particle Image Velocimetry (PIV) und Laser-Induced Fluorescence (LIF) eingesetzt. Dies ermöglichte eine Analyse des vertikalen Fluidtransports nahe der Sediment-Wasser-Grenzschicht, basierend auf der räumlichen Tracerverteilung, der turbulenten kinetischen Energie, den vertikalen turbulenten Flüssen und den turbulenten Mischungsweglängen. Es wurden drei Merkmale der Meeresbodentopographie untersucht: der generelle Einfluss von Bodenrippeln im Vergleich zu flachen Böden, der Einfluss der Rippelkontur und die Auswirkungen von Rippelasymmetrie. Zudem wurden drei unterschiedliche Wellenszenarien verwendet, um den Einfluss der Wellenbedingungen als weitere Variable zu untersuchen.
Die Ergebnisse verdeutlichen die entscheidende Rolle, die die Bodentopografie und die oszillierende Strömung bei der Erzeugung von Turbulenz und damit beim Fluidtransport und der lokalen Konzentrationsverteilung spielen. Besonders die Steigerung von ruhigen zu stürmischen Wellenbedingungen erhöht den vertikalen Fluidtransport über den Bodenrippeln erheblich und übertrifft dabei die Auswirkungen geringfügiger topographischer Variationen wie Änderungen der Rippelform oder des Rippelsymmetrie-Faktors. Strömungsablösung und Wirbelbildung, die bei starker oszillierender Strömung an den leeseitigen Rippelflanken auftreten, wurden als zentrale Einflussfaktoren in Hinblick auf den Traceraustritt und den vertikalen Transport identifiziert. Es wurde beobachtet, dass die Rippelform und der Rippelsymmetrie-Faktor den Ort und Zeitpunkt der Strömungsablösung sowie die räumliche Ausdehnung der Ablösewirbel beeinflussen.
Die vorliegende Arbeit liefert erstmals quantitative Daten zu vertikalen turbulenten Flüssen und Mischungsweglängen hinsichtlich des passiven Skalartransports über durchlässigen Bodenrippeln und stellt damit wichtige Parameter für die Modellierung solcher Prozesse in numerischen Simulationen bereit. Die Ergebnisse unterstreichen die Notwendigkeit, die Meeresbodentopografie in strömungsmechanische Modelle des Stofftransports zu integrieren. Die Erkenntnisse können zur Verfeinerung von Modellen beitragen, die die Ausbreitung von Schadstoffen und Nährstoffen in küstennahen Gewässern vorhersagen.

Danksagung - Acknowledgments

An dieser Stelle möchte ich mich ganz besonders bei Prof. Dr.-Ing. habil. Sven Grundmann, Dr. rer. nat. Martin Brede und PD Dr. Stefan Forster für die Bereitstellung des interessanten und herausfordernden Themas sowie für ihren fachlichen Rat und ihre Unterstützung bedanken, ohne die diese Arbeit nicht möglich gewesen wäre. Hierbei hat mich Martin Brede als mein Erstbetreuer mit seiner technischen und fachlichen Expertise unter anderem bei der Vorbereitung der Messungen sowie bei der Abstimmung zum methodischen Vorgehen im Rahmen dieser Arbeit unterstützt. Gleichzeitig stand mir mein Zweitbetreuer Stefan Forster insbesondere bei interdisziplinären Fragestellungen zur Seite.

Ein großer Dank gilt auch meinen Kolleginnen und Kollegen, den technischen, administrativen und wissenschaftlichen Mitarbeitenden des Lehrstuhls Strömungsmechanik, die mich in vielen Situationen tatkräftig unterstützt haben. Der Austausch mit den anderen Doktorandinnen und Doktoranden war stets bereichernd und hat nicht nur fachlich meine Arbeit vorangebracht, sondern mir auch bei der Bewältigung herausfordernder Phasen geholfen. Die langen Stunden im Labor, wären ohne Matthias und Tobias nur halb so kurzweilig und produktiv gewesen.

Ein ganz besonderer Dank geht an meine geschätzte Kollegin Helena. Die tiefgehenden fachlichen Diskussionen und die zahlreichen wertvollen Kommentare waren für die Fertigstellung dieser Dissertation unersetzlich.

I would also like to express my sincere thanks to my graduate school Baltic TRANSCOAST. The warm and collaborative atmosphere, along with the international perspective, encouraged me to expand my horizons. I am especially grateful to Anna, Daniel, and Erwin for the invaluable theoretical and practical support I received from you.

Ein weiterer Dank gilt M. Schönke und P. Feldens vom IOW, ohne deren Unterstützung die mikrotopografischen Messungen nicht möglich gewesen wären.

Von ganzem Herzen danke ich meiner Familie – meinen Eltern, meiner Schwester und dem restlichen Familienkreis – für ihre Unterstützung und ihre stete Ermutigung.

Ein herzlicher Dank geht auch an meine Freundinnen und Freunde, die mir in dieser Zeit stets mit Verständnis zur Seite standen und mir halfen, den nötigen Ausgleich zu finden sowie die Herausforderungen dieser Arbeit mit einem positiven Blick zu meistern.

Zu guter Letzt möchte ich meinem Lebensgefährten Steffen danken, dessen Verständnis und Unterstützung mir immer den Rücken gestärkt und mich durch die Höhen und Tiefen der Promotion begleitet haben.

This research was conducted at the Chair of Fluid Mechanics within the Faculty of Mechanical Engineering and Marine Technology at the University of Rostock, as part of the DFG-funded Research Training Group "Baltic TRANSCOAST" (GRK 2000, Subproject H4).

"To any one who, for the first time, sees a great stretch of sandy shore covered with innumerable ridges and furrows, as if combed with a giant comb, a dozen questions must immediately present themselves..."

– Hertha Marks Ayrton, 1910

Contents

Chapter 1

Introduction

Maintaining the balance of the oceans is essential for sustaining Earth's ecosystems. The ocean plays a critical role in regulating climate and ensuring food security, making the preservation of this balance crucial for the future stability of global ecosystems [Cooley et al., 2023]. Understanding the underlying processes that contribute to this balance is key to environmental conservation.
In this context, coastal zones are of particular interest due to their unique role as interfaces between terrestrial and marine environments. These transitional areas, where terrestrial and marine ecosystems merge, support high biodiversity and include sensitive habitats such as estuaries, salt marshes, and coral reefs. As a result, coastal zones are highly susceptible to pollution and eutrophication. [Luijendijk et al., 2020].
A key pathway for beneficial or harmful substances to enter coastal water bodies is through sediment-originated matter flux, which reaches the water layer directly above the seabed, known as the benthic boundary layer, via submarine groundwater discharge. This process is particularly significant in sandy sediments, which cover more than 45% of the global inner continental shelf [Hall, 2002] and facilitate high flow rates across the sediment-water interface due to their pronounced permeability. Consequently, substances such as new or recycled nutrients, carbon, metals, and various solutes are introduced into the oceans through the coastal sediment e.g. [Burnett et al., 2003], [Santos et al., 2012].
One aspect is to quantify the net matter flux, whereas another approach is to examine the distribution and local concentrations of discharging substances within the water column to understand biological and biogeochemical processes within the benthic boundary layer. Therefore, the aim of this study is to enhance the fluid mechanical understanding of the discharging process and the vertical transport dynamics of passive scalars in the coastal benthic environment.

The research questions addressed in this thesis focus on how seabed topography affects the vertical transport of a fluid emerging from a permeable seabed, with the fluid injected at the seabed's bottom at a constant volumetric flow rate. The underlying hypothesis is that the interaction between the seabed topography and an oscillating flow generates varying degrees of turbulence. This turbulence, in turn, governs the transport of the emerging fluid, thereby influencing its local concentration values within the water column.
The specific subjects of investigation are as follows:

1. Influence of a rippled seabed compared to a flat seabed: How does the presence of a generic rippled seabed surface affect these processes, as compared to a generic flat seabed?

2. Effect of the ripple shape: How does the shape of seabed ripples influence these processes? This is examined by comparing a generic sinusoidal rippled bed to a more naturally rippled bed with sharper crests and broader troughs, assessing the impact of ripple geometry.
3. Impact of ripple asymmetry: How does the asymmetry of seabed ripples influence these processes? This question examines the differences in fluid behaviour arising from an asymmetric compared to a symmetric ripple geometry.

The scope of this thesis includes the investigation of different seabed geometries interacting with varying oscillating flow fields and their effects on the transport and mixing of a tracer fluid within the near-bottom boundary layer. Therefore, a series of wave tank experiments with a tracer fluid emerging from an artificial seabed were conducted. The experimental setup included three distinct wave scenarios adopted from [Karow, 2019], each designed to replicate different oscillatory flow conditions. To capture a comprehensive range of seabed influences, four seabed models made of foam were designed: a flat bed, a sinusoidal rippled bed, and two naturally rippled beds based on field data — one symmetric and one asymmetric. The combination of these two parameters resulted in a total of twelve measurement configurations.
The main measurement campaign employed simultaneous particle image velocimetry (PIV) and laser-induced fluorescence (LIF) measurements to gather detailed time-resolved data of the velocity field and the concentration field of the discharging tracer fluid. The turbulent transport characteristics were assessed through several key metrics, including time-averaged vertical profiles of concentration, turbulent kinetic energy, and the vertical turbulent flux. Additionally, phase-resolved maps of these three quantities were analyzed to understand the cyclic variations in the flow dynamics. The study also included the evaluation of mixing length profiles to further characterize the transport processes above the different seabed models under all three wave scenarios.

This thesis is an outcome of the sub-project "H4: Waves and turbulence on wavy coastal seabeds inducing vertical scalar transport" within the Research Training Group Baltic TRANSCOAST, funded by the DFG (Deutsche Forschungsgemeinschaft - German Research Foundation). Baltic TRANSCOAST aims to contribute to understanding coastal marine-terrestrial water and matter exchange processes by addressing various geochemical, biological, and hydrodynamic processes [Jurasinski et al., 2018]. At the start of sub-project H4, N. Karow developed the experimental setup which was used for the main measurement campaign of this work. [Karow, 2019] investigated the effects of seabed permeability and slope on tracer propagation and turbulent transport. This study serves as a follow-up to his work and is succeeded by the work of H. Stirnweiß, formerly Klettke. [Klettke et al., 2023], [Stirnweiß et al., 2024a] and [Stirnweiß et al., 2024b] primarily focus on flow dynamics and turbulent transport of a passive scalar above gravelly sands.

This document is structured as follows: Chapter 2 provides an overview of the geophysical principles essential for understanding the factors that influence the transport processes

examined in this study. Chapter 3 outlines the fluid mechanical fundamentals necessary for characterizing and analyzing the turbulent transport observed in the laboratory experiments. Chapter 4 offers a detailed description of the experimental wave tank setup, the boundary conditions, the measurement procedure, and the analysis of the velocity and concentration field data obtained. The results of this analysis are presented in Chapter 5 and discussed in Chapter 6. Here, the observed processes above the various seabed models were systematically compared in pairs: the flat seabed with the sinusoidal rippled seabed, the sinusoidal rippled seabed - representing a simplified ripple profile - with the naturally rippled (symmetric) seabed developed based on field data, and the symmetric naturally rippled seabed with the asymmetric naturally rippled seabed. Chapter 7 summarizes the key findings regarding the broader significance of the research and suggest future research directions.

Chapter 2

Geophysical Background

This chapter provides a foundational overview of key geophysical aspects essential for understanding the processes investigated in this thesis. It covers the topics of submarine groundwater discharge and pore water exchange, sediment properties, the benthic boundary layer, ocean waves, sand ripples, as well as fluxes and flow at a rippled sediment-water interface. The complex interplay between these factors shapes the phenomena observed in the conducted laboratory experiments.

2.1 Submarine Groundwater Discharge and Pore Water Exchange

Submarine groundwater discharge (SGD) has been a recognized phenomenon for centuries, but it has gained significant scientific attention since the late seventies, when [Kohout, 1979] observed geothermal submarine springs at the southwestern shore of Florida using thermal infrared and Landsat imagery to analyse NASA data and [Lee, 1977] developed a device called seepage meter for measuring groundwater seepage flux into lakes and estuaries. This device was then used by [Bokuniewicz, 1980] to measure seepage fluxes into the Great South Bay of New York. [Johannes, 1980] firstly summarized several scattered scientific contributions concerning SGD and emphasised its ecological significance. Notably, [Moore, 1996] observed a massive enrichment of ^{226}Ra (Radium isotope) in coastal waters of the South Atlantic Bight (United States) and hypothesized that groundwater discharge is the main source of this. [Taniguchi et al., 2002] stated that SGD may be both volumetrically and chemically important to coastal water and chemical budgets and, therefore, greater attention should be given to this phenomenon when considering water and dissolved material budgets at both local and global scales.

The classical definition of SGD "as any and all flow of water on continental margins from the seabed to the coastal ocean, regardless of fluid composition or driving force" was given by [Burnett et al., 2003]. [Moore, 2010] specified this definition by differentiating between large and small-scale processes. He stated that SGD should be referred to as processes on a scale from meters to kilometres, whereas smaller-scale processes, termed pore water exchange (PWE), should be considered separately although they are technically a type of SGD. [Taniguchi et al., 2019] refer to SGD and PWE as "different but overlapping processes".

Another aspect of SGD that must be considered is the source of the discharging fluid. Therefore, SGD can be distinguished into fresh (or terrestrial) SGD and recirculated (or marine) SGD.

Fresh submarine groundwater discharge (FSGD) can directly transport land-originated substances such as nutrients, carbon or metals into coastal water bodies. [Luijendijk et al., 2020] state, that although FSGD is not significant for the ocean water and chemical budget on a global scale, it can have severe effects on a local scale. Particularly in coastal regions, FSGD can cause or enhance eutrophication and pollution due to high nutrient and solute loads of terrestrially derived groundwater. Therefore, it can directly lead to harmful algal blooms, the spread of pollutants or coral reef degradation [Luijendijk et al., 2020]. On the other hand, FSGD can be an important nutrient or even a freshwater source. According to [Moosdorf and Oehler, 2017], it is locally used for drinking, hygiene, or even agricultural irrigation.
Recirculated SGD, on the other hand, is characterized by its residence in subterranean mixing zones of terrestrial groundwater and seawater, also termed subterranean estuaries (STE), and, thus, carries products of biogeochemical reactions between terrestrially and marine-derived substances as well as sediment components [Burnett et al., 2003], [Moore, 2010], [Taniguchi et al., 2019], [Moosdorf et al., 2021]. Therefore, the differentiation between terrestrial and marine SGD is of great importance regarding the composition of the discharging fluid.
PWE refers to the direct exchange of fluid at the sediment-water interface on comparably small scales (millimetres to meters) [Moore, 2010], [Taniguchi et al., 2019], characterized by a zero net water flux, which should not be confused with a zero net tracer flux [Cook et al., 2018]. A common example is the advection of oxygen-rich sea water into the sediment. Within the sediment, oxygen is consumed by aerobic decomposition of organic matter, animal respiration or oxidation of reduced product of anaerobic decay [Berg et al., 2003]. This biological and biogeochemical reaction zone spreads over several centimetres and significantly affects the metal and nutrient distribution in permeable sands [Huettel et al., 2014]. Furthermore, the reaction and decomposition products, as well as anoxic pore water, are released into the water column and, therefore, affect matter distribution within the benthic boundary layer.
Regardless of whether interfacial water flux occurs due to FSGD, recycled SGD, or PWE, it constitutes a pathway for various substances into and out of the sediment and thus affects the biology and biogeochemistry within near-seafloor water layers. The described mechanisms are different but intersecting phenomena, which can occur at the same place and time [Taniguchi et al., 2019].
In their review paper [Santos et al., 2012] identified twelve driving forces of pore and groundwater flow in permeable coastal sediments, which are:

1. Terrestrial hydraulic gradients
2. Seasonal changes in the aquifer level on land moving the location of the STE
3. Wave setup and tidal pumping
4. Water level differences across permeable barriers
5. Flow- and topography-induced pressure gradients
6. Wave pumping
7. Ripple and other bed form migration

8. Fluid shear
9. Density-driven convection
10. Bioirrigation and bioturbation
11. Gas bubble upwelling
12. Sediment compaction

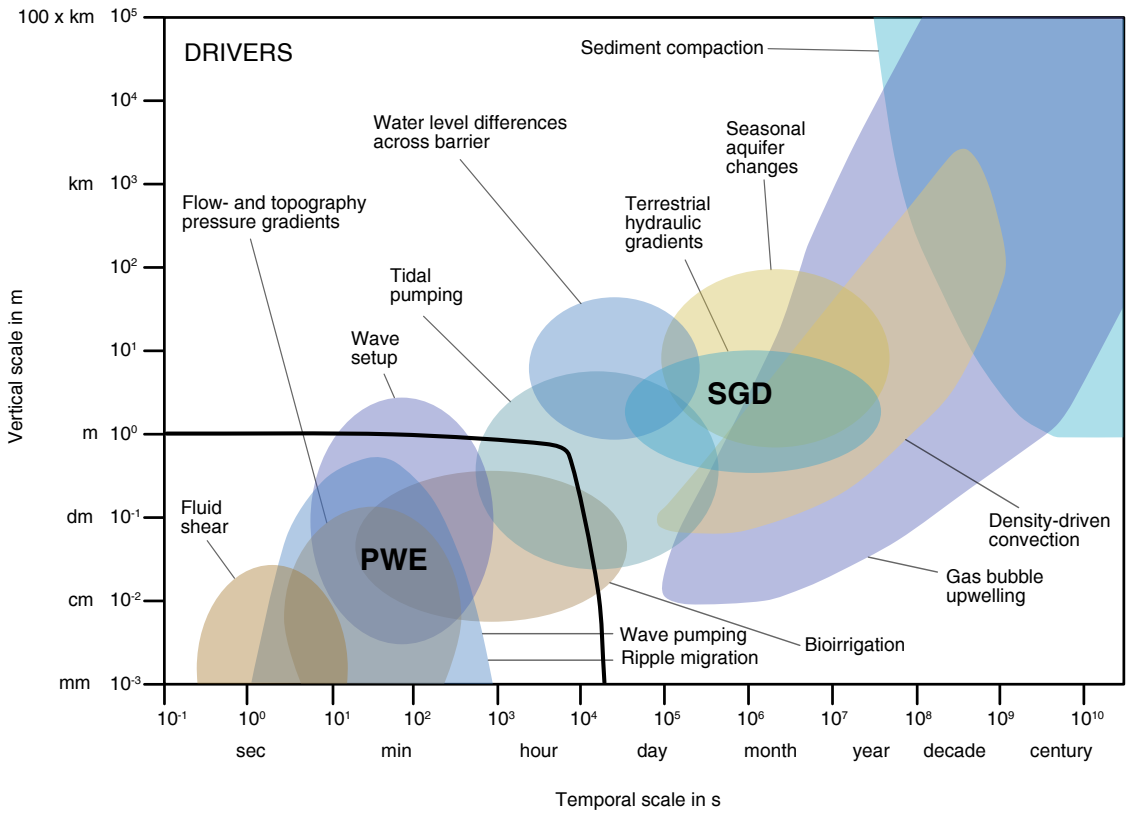

Figure 2.1: Distinction between PWE and SGD based on spatial and temporal scales adapted from [Taniguchi et al., 2019]: Multiple overlapping geophysical drivers influence fluid flow across a range of scales from millimetres to kilometres and seconds to years. Processes such as wave pumping, topographically-induced pressure gradients, and fluid shear drive PWE on smaller spatial (< 1 m) and temporal scales (< 1 hour), while larger scale processes like tidal pumping and wave setup may be classified as either PWE or SGD depending on the context and measurement methods. The distinction between PWE and SGD is highlighted by the thick boundary line, building on the interpretation of [Moore, 2010]

All of these mechanisms induce flow across the sediment-water interface, consequently impacting the influx of both new and recycled nutrients into seawater on different spatial and temporal scales, as illustrated in Figure 2.1. Additionally, they can affect the release and absorption of harmful substances from the seabed [Santos et al., 2012]. However, since this thesis focuses on wave-induced turbulent transport of discharging water above rippled seabeds on relatively small scales (constrained by the experimental wave tank setup) the scope includes the driving forces 5 (Flow- and topography-induced pressure gradients), 6 (Wave pumping) and 8 (Fluid Shear), as summarized in Figure 2.2.

Topographical features such as sand ripples, benthic organisms, stones, or shells cause flow obstruction and acceleration and therefore local increases as well as decreases in the pressure field, which in turn lead to PWE, as further described in Section 2.6.
The phenomenon of wave pumping originates from pressure gradients created by variances in hydrostatic pressures beneath wave crests and troughs. These oscillating pressures transmit through the permeable seabed, where the effect of damping reduces their magnitude and induces a phase shift with increasing sediment depth. The resulting pressure gradients drive PWE. The intensity of wave pumping is proportional to wave amplitude as well as the sediment permeability, and depth. The effect of wave pumping is especially relevant in shallow and intermediate waters, see Section 2.4.
Fluid shear at the sediment-water interface induces PWE by extending the water column flow velocity profile into the permeable bed, forming a layer known as the Brinkman layer, see Section 2.3. Within this layer, pore water flows parallel to the sediment surface, with velocities decreasing exponentially with depth. This shear-induced pore water flow can penetrate several millimetres into sandy sediments. Factors such as fluid shear, sediment complexity, and the downward decrease in velocities contribute to flow dispersion and enhanced vertical fluid exchange with the overlying water. This shear-driven PWE occurs in both flat and rippled sediment surfaces.
The driving forces 1-4 as well as 9, 11 and 12 relate to large-scale boundary conditions and might thus be more suitable objects of investigation for numerical simulations than for laboratory experiments; The investigation of ripple and other bed form migration (7) requires an actual sand bed. Utilising the available wave tank to conduct dye experiments to measure turbulent fluxes above authentic sand or sand equivalent beds is suboptimal, as a large volume of sand must be replaced after each experiment. The effects of bioirrigation and bioturbation could be fields for further investigations as addressed in Chapter 7.
Flow- and topography-induced pressure gradients, wave pumping, and fluid shear are directly forced by the prevailing small-scale flow conditions. However, discharge can only occur, if the seabed interface allows for fluid exchange.

2.2 Sediment Properties

Most of the inner continental shelf is covered by sandy sediments [Hall, 2002], including the coastal sites investigated by the Baltic TRANSCOAST project. These sediments are characterized by being comparatively permeable.
Permeable media can be defined by multiple parameters, including pore density, porosity, and permeability, each offering distinct insights into their structure and behaviour. Although not directly convertible, these parameters are related to one another, as depicted in Figure 2.3.
Porosity, for instance, quantifies the proportion of pore volume relative to the total volume within a specified body. As per [Dean and Dalrymple, 2001], the porosity of sand typically ranges between 0.3 to 0.4, a value subject to variations influenced by sand composition and grain size. Moreover, dynamic forces such as waves and currents exert notable effects on sand porosity. Initially, freshly deposited sand exhibits high porosity; however, as a

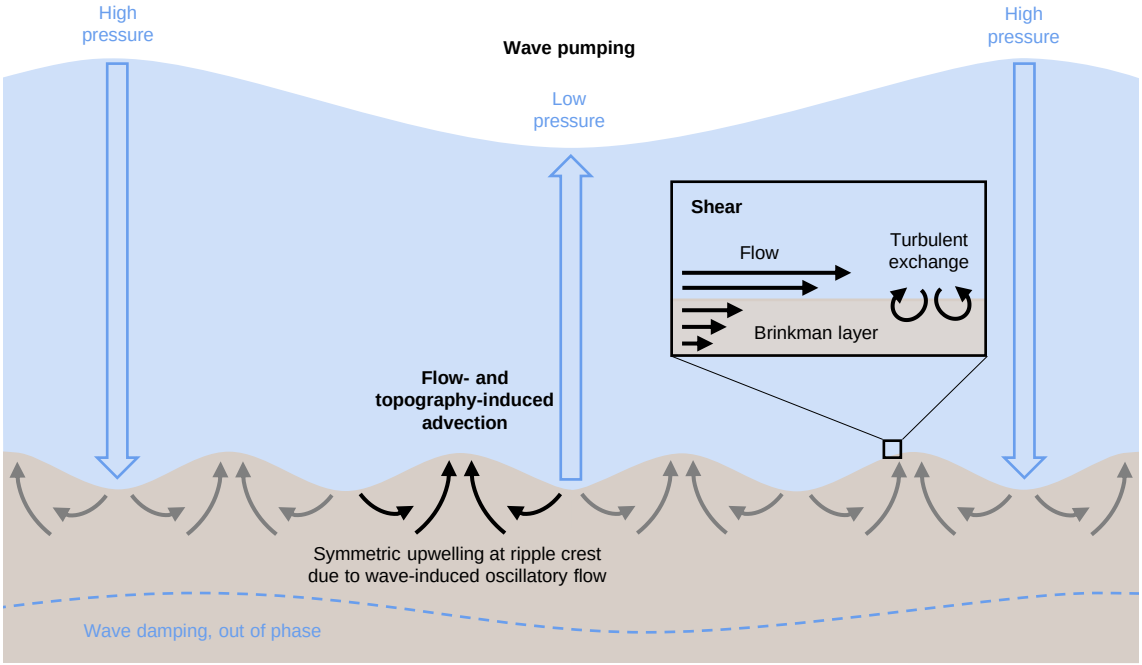

Figure 2.2: Driving forces for SGD and PWE after [Santos et al., 2012], assumed to be particularly relevant to the scope of this thesis: Wave pumping, flow- and topography-induced advection, and shear at the sediment-water interface inducing turbulent exchange

consequence of wave and current-induced movements, a more compact and stable structure evolves, leading to a decrease in porosity.

Conversely, pore density describes the number of pores within a given volume. Notably, while porosity and pore density provide crucial metrics for understanding media structure, they do not inherently convey information about pore shape or dimensions, which for sediments depends on e.g. grain size, shape, or sorting [McLachlan and Turner, 1994].

In the context of this project's experimental requirements and objectives, the pivotal characteristic is permeability, owing to its fundamental association with perfusion velocity, commonly referred to as the Darcy velocity u_D. This parameter directly impacts both pore water flux and the velocity profile within the open channel flow. Permeability K quantifies the ability of a permeable medium to transmit a fluid under a given pressure gradient. As is evident from equation 2.1, it is a function of the fluid's viscosity η, the volumetric flow rate Q, the cross-sectional area A, and the pressure gradient $\Delta p/L$ [Hölting and Coldewey, 2019].

$$K = \eta \cdot \frac{Q}{A} \cdot \frac{1}{\Delta p/L} \tag{2.1}$$

In the context of PWE, [Huettel et al., 2014] define permeable sediments as those with a permeability greater than 10^{-12} m^2. Once this threshold is attained, there is a notable deviation in interfacial solute fluxes from fluxes due to molecular diffusive transport. Following [Bear, 1988], the permeability of sand spans a range of 10^{-12} m^2 to 10^{-9} m^2. During her doctoral research within the Baltic TRANSCOAST project, [Schade, 2019] measured sediment permeabilities ranging from $1.36 \cdot 10^{-12}$ m^2 to $1.13 \cdot 10^{-10}$ m^2 in the

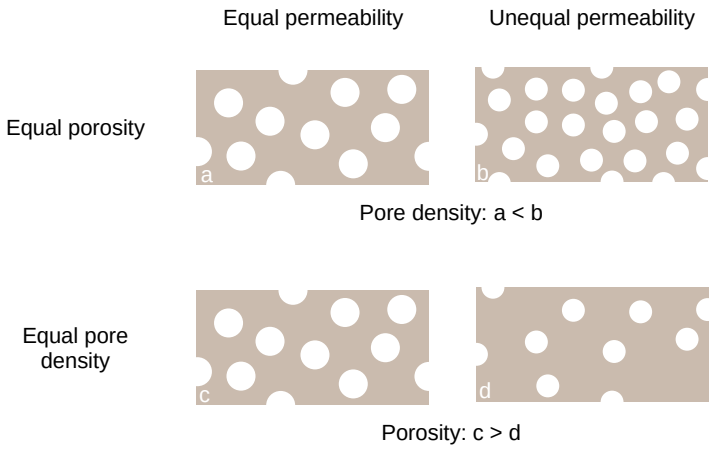

Figure 2.3: Schematic representation of the relationship between porosity, pore density, and permeability: Equal porosity and equal pore density can both lead to different permeability since these parameters do not consider grain size, shape or sorting, and thus the structure of the media, which is relevant for hydraulic conductivity

vicinity of the Hütelmoor. For the laboratory experiments, [Karow, 2019] employed two foam mats, each five centimetres thick, with varying permeabilities. One mat featured a permeability of $2.35 \cdot 10^{-10}$ m^2 and a pore density of 45 pores per inch, while the other had a permeability of $3.47 \cdot 10^{-9}$ m^2 with a pore density of 10 pores per inch. For this thesis, experiments were conducted with foam mats, which exhibited a permeability of $5.8 \cdot 10^{-10}$ m^2 in falling head permeability measurements, see section 4.2.3.
The permeability and accordingly the Darcy velocity influences the velocity profile at the sediment-water interface known as the benthic boundary layer.

2.3 Benthic Boundary Layer

The benthic boundary layer (BBL) is the part of the water column and the surficial seabed that is affected by the sediment-water-interface [Boudreau and Jørgensen, 2001]. Particularly in shelf environments, the BBL plays an important role in both biological and biogeochemical processes. It acts as a crucial interface facilitating nutrient cycling and habitat formation [Gili et al., 2020]. Also from a physical perspective, the BBL is a highly dynamic zone connecting the sediment-water interface with the overlying water column and amplifying turbulence-induced mixing and transport processes [Grant and Madsen, 1986].
With a thickness typically on the order of tens of meters, this layer is determined by bottom stress and the effects of Earth's rotation (Coriolis forces), remaining relatively small in comparison to the average ocean depth of approximately 4000 m. Nevertheless, in coastal intermediate, or shallow regions, the BBL can extend over larger portions or even encompass most of the water column.
The BBL's profile is primarily governed by the mean flow $\overline{u}(z)$, which decreases towards the bottom due to friction. Depending on the dominating forces, the BBL can be separated into distinct layers, as illustrated in Figure 2.4.

The uppermost segment of the BBL, known as the Ekman layer, signifies the part of the water column where pressure gradient, friction, and Coriolis forces achieve equilibrium. With decreasing bottom distance, the impact of earth rotation diminishes.
This results in the logarithmic layer, where turbulent friction, induced by the bottom stress, and the pressure gradient become the dominating forces, causing velocity to logarithmically increase with growing bottom distance.
In proximity to the seabed - approximately 1 mm-, friction arises from molecular effects, meaning that momentum is transferred by molecular diffusion rather than by turbulence since vertical velocity fluctuations are suppressed by the seabed surface. This layer only develops above very smooth bottoms and is known as the linear viscous boundary layer, as it is governed by viscosity resulting in a linear increase of velocity [Lueck et al., 2019].
Considering the permeability of the ocean sediment, see Section 2.2, a transition zone to the pressure-driven Darcy flow within the sediment, termed the Brinkman layer, will occur. Within the Brinkman layer, shear-driven diffusion of momentum from the overlying turbulent fluid flow affects the underlying Darcy flow [Boudreau and Jørgensen, 2001].
In a wave-dominated environment, the logarithmic velocity profile transitions to a wave boundary layer profile, as also illustrated in Figure 2.4. Compared to a unidirectional current of similar intensity, the bed shear stress in an oscillating flow is significantly stronger, leading to a thinner boundary layer. This is due to the limited vertical growth of wave-generated turbulence within the wave boundary layer, constrained by the flow direction reversals [Boudreau and Jørgensen, 2001], [Pomeroy et al., 2017]. The thickness of the wave boundary layer is proportional to the duration of a wave cycle, the wave period T [Southard, 2024]. Instantaneous (or phase-averaged) velocity profiles exhibit a change of amplitude and relative phase dependent on the seabed distance. The velocity close to the sediment-water interface and the bed shear stress are ahead of the free stream velocity [Nielsen, 1992]. The frictional effects near the bed dampen the motion of the water and slow it down, but not enough to fully compensate for inertia effects. Therefore, during the positive acceleration phases, the water reaches a higher velocity than the surrounding free-stream velocity, causing a velocity overshoot. The oscillating nature of a wave-induced flow will be explained in the following.

2.4 Ocean Waves

On a small temporal and spatial scale wave motion is the dominating motion of ocean water in the coastal zone.
In the domains of physics, mathematics, engineering, and allied disciplines, a wave refers to the progressive, dynamic disturbance — a deviation from equilibrium — of one or more measurable quantities e.g.[Tipler et al., 2019]. Electromagnetic waves align with disturbances or oscillations in electrical or magnetic fields, while mechanical waves encompass disruptions in any medium or substance - gas, liquid, solid.
The simplest mathematical description of a wave is based on the linear wave theory according to [Airy, 1845], which is illustrated in Figure 2.5. This theory assumes an incompressible fluid, irrotational fluid motion (implying the neglect of viscous effects), an

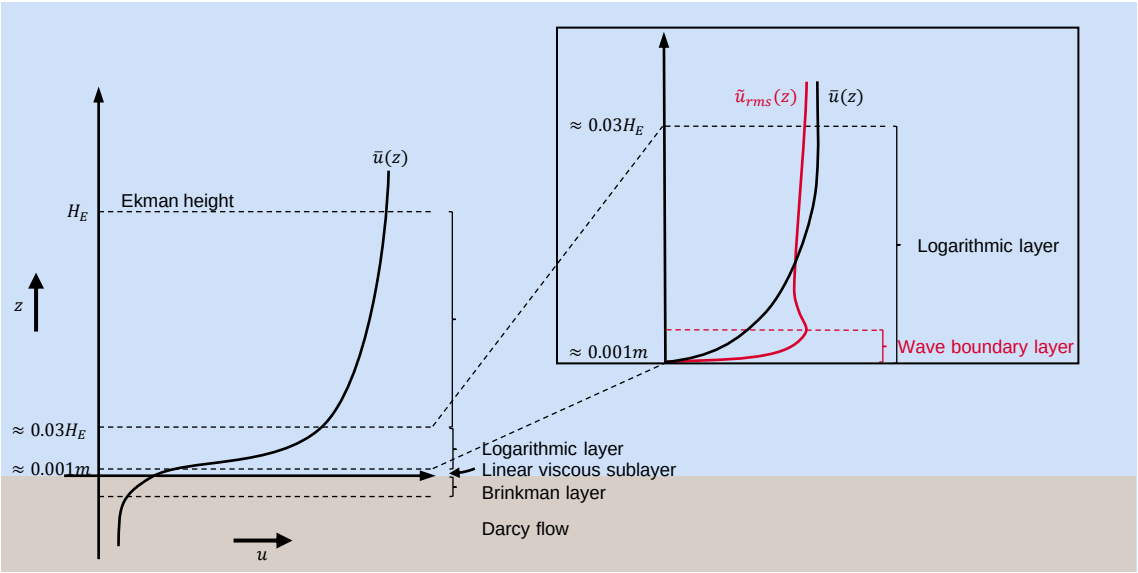

Figure 2.4: Sublayers of the benthic boundary layer adapted from [Boudreau and Jørgensen, 2001], [Lueck et al., 2008] and [Pomeroy et al., 2017]. In the Ekman layer, the pressure-gradient, turbulent friction and Coriolis forces are balanced. In the Logarithmic layer, the impact of Coriolis forces is neglectable. In the linear viscous layer - typically on the order of 10^{-3} meters thick, though the thickness depends on viscosity and friction velocity - friction is induced by molecular effects rather than turbulence. Within the sediment, the Brinkman layer serves as the transitional zone between the Darcy flow and the shear flow near the seabed; Under oscillating flow conditions, the logarithmic profile evolves into a wave boundary layer profile characterized by a significantly thinner boundary layer and overshooting velocity.

impermeable flat bottom, and very small wave amplitudes. The wave height H equals twice the wave amplitude a. The water depth d defines the still position of the water surface at $z = 0$ and the bed location at $z = -d$. The wave phase angle $\varphi(t)$ measures a point's position within a wave cycle at a given time. It specifies the wave's periodical displacement relative to a reference point, typically at time $t = 0$ or the spatial coordinate $x = 0$. The phase angle describes the state of oscillation of the wave at any instant. The displacement of the water surface $\zeta(x, t)$ is given by Equation 2.2.

$$\zeta(x,t) = \frac{H}{2}\cos\left(k(x - u_W t)\right) = a\cos\left(kx - \omega t\right) \tag{2.2}$$

Given that the wave motion is assumed to be periodic in the wave direction $+x$, the wave number k is introduced to ensure that the cosine function repeats over the distance λ, which is the wavelength. Thus, the wave number is defined as $k = 2\pi/\lambda$. For periodicity in time, meaning the wave repeats every T seconds, the wave's angular frequency is defined as $\omega = 2\pi/T$, with T denoting the wave period. Finally, u_W is the speed at which the wave form propagates, given by $u_W = \lambda/T = \omega/k$ [Dean and Dalrymple, 2001].
Many waves persist after their formation due to a restoring force that overcompensates and therefore induces oscillation.
Ocean waves, a subset of mechanical waves, are disturbances that transfer energy through seawater. Their defining features include the disturbing force, the restoring force, and their characteristic wavelength range. These waves can occur within the water column as

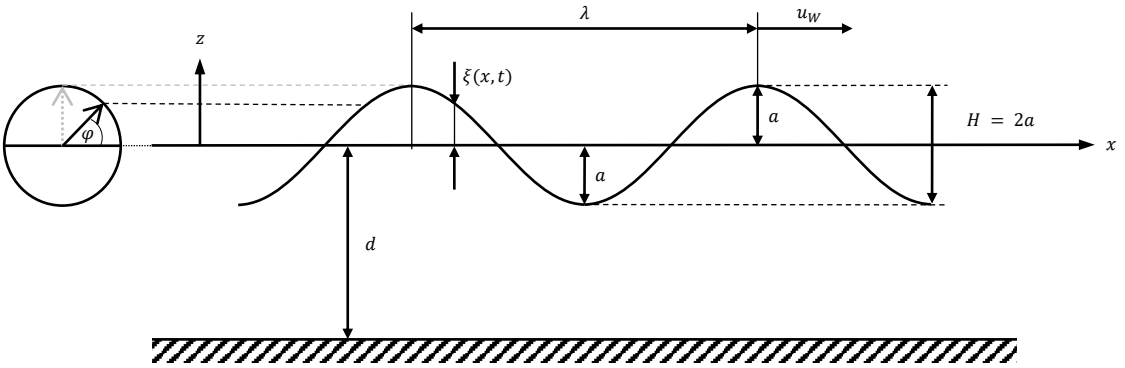

Figure 2.5: Schematic representation of a wave propagating with the wave speed u_W in the $+x$ direction, following [Airy, 1845]'s linear wave theory. The wave has a wavelength λ, an amplitude a, and a wave height $H = 2a$. The vertical displacement of the wave surface is denoted by $\zeta(x,t)$. The water depth is represented by d. The phase angle $\varphi(t)$ measures the current wave displacement relative to time $t = 0$ or the coordinate origin at $x = 0$ [Dean and Dalrymple, 2001]

internal waves or at the surface as surface waves. Internal waves form at the boundaries between layers of different densities and can be caused by tidal forces, current changes, or other disturbances. Surface waves visibly propagate energy across the ocean surface covering a wide spectrum of scales based on their wavelength and restoring forces. Capillary waves, with the shortest wavelengths up to 1.73 cm, are typically generated by wind disturbing the water surface and are restored by the surface tension and cohesion of water molecules. Larger waves, with wavelengths ranging from $60 - 150$ m, are restored by gravity and are therefore termed gravity waves. They originate from wind, referred to as wind waves, from seismic disturbances that generate tsunamis with wavelengths of approximately 200 km, or from tides, which produce tidal waves with wavelengths equal to half the Earth's circumference [Garrison and Ellis, 2018]. Gravity waves on the air-sea interface of the ocean are called surface gravity waves. This is the most prevalent type in the open ocean. However, the actual ocean surface is an irregular mixture of numerous waves of varying speeds and sizes, interfering to form a wave spectrum. Non-linear effects, such as wave shoaling and breaking, additionally contribute to the complexity of this spectrum. AConsequently, Airy's linear wave theory is rarely sufficient for describing ocean waves. Stokes's wave theory supplements Airy's theory with non-linear terms and is commonly used for calculating waves in intermediate and deep water regions. This is further detailed in [Karow, 2019] and revisited in Section 4.2.1 of this thesis.

As fluid elements oscillate about their equilibrium position due to surface gravity waves, they describe closed or nearly closed paths known as orbitals. The shape of these orbitals is determined by the relationship between a wave's wavelength and the water depth, which is depicted in Figure 2.6. Consequently, the behaviour of a wave is profoundly influenced by the depth of the water through which it traverses. The relationship between a wave's wavelength and water depth defines its type.

If the water is deeper than half the wavelength, the wave is classified as a deep-water wave. In this case, the seafloor is unaffected by the wave motion, and vice versa: the waves do not interact with the sea floor. Deep-water waves exhibit nearly circular orbitals, where the maximum horizontal and maximum vertical orbital velocities are approximately equal. As

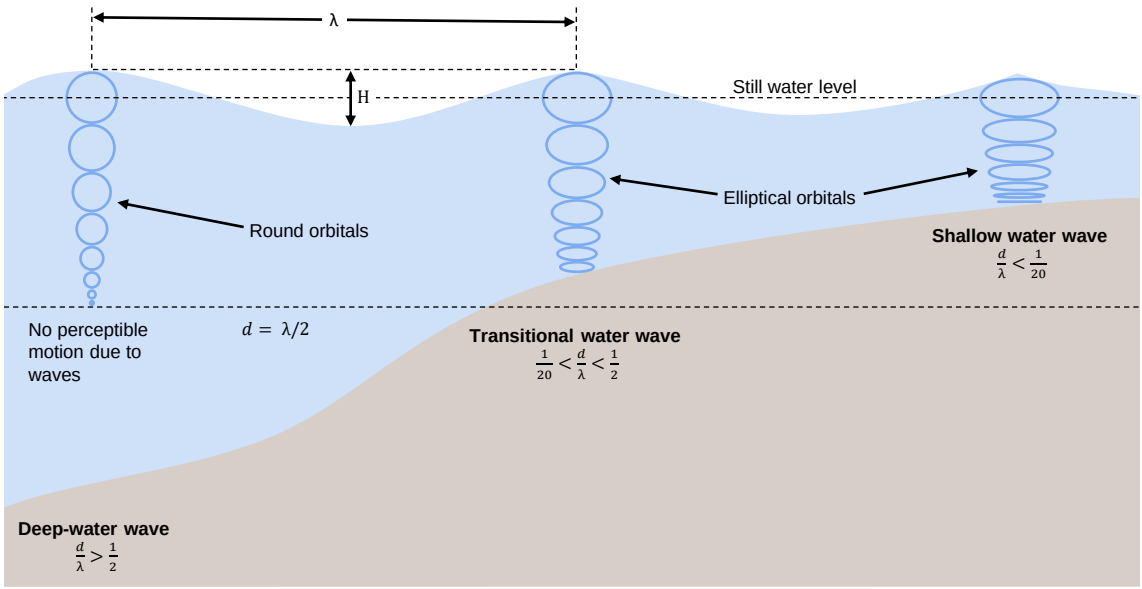

Figure 2.6: Schematic illustration of deep, intermediate and shallow water waves being an outcome of the relationship between water depth d and wavelength λ: Only for $d/\lambda < 1/2$ the wave is affected by the bottom and vice versa

waves propagate deeper into the water, their energy is distributed over a larger volume. The circular motion of water particles decreases with depth because the wave's energy diminishes as it penetrates the water column. By the time a depth equal to half the wavelength is reached, the motion of the water particles becomes minimal and essentially negligible.

When the water depth is less than one-twentieth of the wavelength, the wave is classified as a shallow-water wave, which interacts with the sea floor and alters the shape of its orbitals to ellipsoids.

Intermediate water waves, also termed transitional water waves, occur when the water depth falls between half and one-twentieth of the wavelength. In this state, the wave begins to be affected by the bottom, resulting in sharpened wave crests and a decrease in wave speed [Garrison and Ellis, 2018].

[Karow, 2019] thoroughly described how the wave scenarios, which were also used for the measurements conducted in this project, were developed based on field measurements using the third-order Stokes wave theory, which implicates non-linear effects occurring in the coastal zone. All three wave scenarios conform to intermediate water waves and will be further specified in Section 4.2.1.

As ocean waves approach the coast, the wave's interaction with the seabed becomes essential. As explained in Section 2.1, wave pumping due to wave-generated pressure gradients drives pore water flow. Furthermore, the oscillating bottom boundary layer interacting with the seabed induces complex hydrodynamic patterns facilitating the exchange of momentum, matter, and energy. This interplay significantly influences pore and groundwater exchange, nutrient cycling, and the transport of solutes and sediment. Therefore, the interaction of the oscillating boundary layer with the seabed, in turn, influences the shape of the seabed itself.

2.5 Sand Ripples

According to the [Oxford English Dictionary, 2024], a ripple mark is "Each of a series of wavy ridges and furrows visible on sand, mud, or snow, or preserved on the bedding planes of sedimentary rocks, and formed by the action of waves, water currents, or wind". Accordingly, a ripple mark forms in sediments due to the influence of fluid flow. In regards to an aquatic environment, the respective fluid is water and the sediment is mainly sand. Sand ripples are categorized into asymmetric current and symmetric wave ripples. The latter are also known as oscillation or vortex ripples.

Geometrically, ripples are characterised by their spacing, described by the ripple wavelength λ_R, their height h_R, and the relationship between these two parameters. This relationship is expressed as steepness, h_R/λ_R, or its reciprocal, the ripple index, λ_R/h_R, as illustrated in Figure 2.7.

In case a (superimposed) current causes ripples to be asymmetric, they can be further described by the ripple symmetry index (RSI) $RSI = \alpha/\beta$, where α is the length of the stoss side and β is the length of the lee side. Thus, symmetric ripples have a symmetry index of $RSI = 1.0$, whereas asymmetric ripples exhibit a symmetry index of $RSI > 1.0$ with $\alpha > \beta$ [Tanner, 1967], [Clifton and Dingler, 1984].

Current ripples are characterized by asymmetric profiles with a low-angle stoss side and a steep-angle lee side. They form in unidirectional or superimposed flow fields e.g. river beds or tidal zones. The height of current ripples ranges from $h_R = 8$ to 33 mm, while their wave length spans from $\lambda_R = 0.08$ to 0.8 m. Stoss slopes range from $s_s = \arctan(h_R/\alpha) = 7$ to $9°$ and lee slopes range from $s_l = \arctan(h_R/\beta) = 10$ to $14°$. Current ripples migrate downstream at a rate of 0.3 to 0.4 mm/s [Amos et al., 2018] based on [Soulsby et al., 2012].

Wave ripples, also termed oscillation or vortex ripples, occur to have rather symmetric profiles with $RSI \approx 1.0$ and are formed by shallow or intermediate surface gravity waves [Selley, 2000]. The orbital movement of the near-bed water layer induces shear stress at the sediment-water interface and can therefore pick up and carry sediment particles under certain conditions (initial "rolling grain ripples" [Bagnold, 1946]). Over time, the process of erosion, transport, and deposition leads to the development of wave ripples. This was first described by [Darwin, 1883] who conducted experiments to understand the formation of ripple marks. The numerical study by [Leftheriotis and Dimas, 2022] provides an updated analysis of the dynamics of wave ripples under the influence of oscillatory flow and sediment transport, while also offering a comprehensive overview of the historical development and current state of research in this field. Wave ripples exhibit heights ranging from $h_R = 8$ to 50 mm and wavelengths spanning from $\lambda_R = 0.07$ to 0.55 m. They typically feature sharp crests and predominantly possess a two-dimensional structure, maintaining a constant shape in the transverse direction. These ripples tend to be stable in time [Amos et al., 2018] based on [Soulsby et al., 2012].

The exact evolution of ripple patterns is highly complex and nearly unpredictable. Numerous studies have been carried out with the aim of predicting ripple geometry and dimensions for given boundary conditions [Davies and Thorne, 2008], [Wiberg and Har-

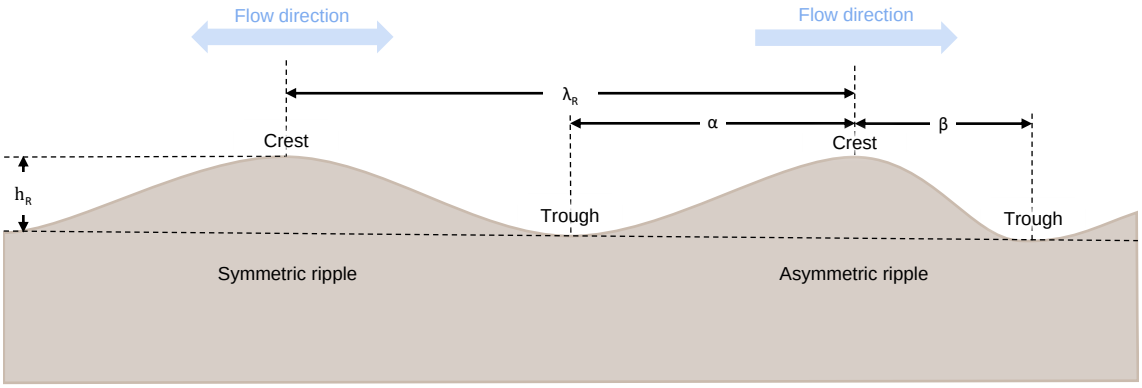

Figure 2.7: Geometrical features of symmetric (left) and asymmetric (right) ripples: The wavelength λ_R refers to the horizontal distance of two ripple crests. The ripple height h_R specifies the vertical distance between a ripple trough and a ripple crest. In case of asymmetry, α defines the length of the stoss and β the length of the lee side

ris, 1994]. They mainly considered the following parameters: the wave bottom orbital velocity, the wave period, the median sediment grain diameter, the sediment density, the density of the fluid, and gravity [Nelson et al., 2013]. This research question is challenging but not particularly relevant to this work. However, not only does the flow field influence the geometry of the ripple, but vice versa, the ripple's geometry also affects the flow field [Wiberg and Harris, 1994]. This in turn dominates the flow across and above the sediment water interface.

2.6 Fluxes and Flow at a Rippled Sediment-Water Interface

Transport processes within the sediment, across the sediment-water interface and in that part of the water column, that is directly affected by this interface have been studied from the perspective of multiple scientific fields and disciplines pursuing various research questions.

The review paper by [Huettel et al., 2014] comprehensively describes benthic exchange, including PWE, in permeable sediments from a biogeochemical perspective. [Huettel et al., 1996] investigated particle and solute fluxes at the sediment-water interface at a small mound under unidirectional flow conditions in a recirculation tank experiment tracing acrylic pigment grains of 1 to 10 µm diameter and a solute tracer (fluorescent red dye, Rhodamine WT). They observed that the pressure increase up and downstream of the mound leads to the intrusion of water carrying particles into the sediment, whereas the pressure drop on top of the mound and at the downstream slope causes upwelling from deeper sediment layers. They noted similar processes for sand ripples and concluded, that the bottom topography significantly increases interfacial particle and solute flux compared to a flat bed. [Huettel and Gust, 1992] emphasize that the permeability of the respective sediment is a key parameter influencing advective exchange processes.

The interaction of sand ripples with an oscillating boundary flow, which induces pressure gradients as a driving factor of PWE, was examined by [Precht and Huettel, 2003] conducting tracer experiments in a wave tank. They demonstrated, that shallow surface

gravity waves can significantly increase PWE by a multiple compared to the exchange by molecular diffusion. Furthermore, they calculated topography-related filtering rates in the wave tank, which substantially exceeded their estimations of solute exchange rates caused by hydrostatic wave pumping. Thus, the superposition of PWE due to wave pumping with PWE resulting from pressure gradients caused by the interaction of the flow with a rippled topography would consequently lead to an increase in the overall exchange rates. The effect of advective PWE on oxygen transport within the sediment was investigated by [Precht and Huettel, 2004]. They used a planar oxygen optode to quantify the spatial and temporal distribution of oxygen within the sediment and demonstrated the inflow of oxygen-rich water at the ripple trough and the outflow of anoxic water from deeper sediment layers at the ripple crest.

One-way coupled simulations of turbulent-oscillating flow in the water column, inducing porous media flow and solute transport, were conducted by [Cardenas et al., 2008] to model oxygen consumption, (de)nitrification, and ammonification within the sediment. The study aimed to link various flow and transport processes at the sediment-water interface, recognising that sediment permeability, topography, and bottom currents control denitrification rates. However, their interest was in transport processes within the sediment, and the matter distribution within the water column was not modelled.

[Berg et al., 2003] agree, that in shallow coastal areas, advection due to wave action and uneven seabeds is the dominant interfacial transport process. They asserted that vertical transport within the water column primarily arises from turbulent motion, as molecular diffusion is limited to very short distances and wave-induced velocities average out to zero over a complete wave period. Therefore, they adapted the eddy covariance measurement technique, which was commonly used in the atmospheric boundary layer, for aquatic environments to measure oxygen fluxes in the BBL. The principle of this technique is based on measuring turbulent fluctuations of the vertical velocity and the corresponding oxygen concentration simultaneously and at the same point above the sediment surface. By correlating these values, the average oxygen flux can be determined. This principle can be transferred to other scalar quantities, further explained in Section 3.2.2. For this purpose, measurements have to be conducted with a sufficiently high temporal resolution to capture these fluctuations and over a period extensive enough to yield a statistically robust representation of their variations. More details about aquatic eddy covariance measurement are extensively elaborated in [Berg et al., 2022].

As noted in Section 2.3, shear at the sediment-water interface induces turbulence within the BBL. Another source for turbulence formation can be flow separation and eddy formation due to topographical features such as sand ripples. Already within the scope of their experiments, [Darwin, 1883] and [Ayrton and Ayrton, 1910] visualized the phenomenon of vortex formation on the lee side of sand ripples. This observation was later confirmed by [Bagnold, 1946] and has since been the subject of numerous experimental and numerical studies, as detailed in [Davies and Thorne, 2005] and more recently in [Leftheriotis and Dimas, 2022]. However, the focus of most studies is on sediment transport.

Solute transport over an impermeable rippled bed in a sinusoidal flow was examined by [Shum, 1995], who conducted numerical simulations, excluding turbulence modelling and

assuming a constant concentration difference between the upper and lower boundaries. The resulting flow field was a combination of an oscillating rectilinear and periodic vortical flow. Vortices were observed to form at the lee side of the ripple crest and merge with one of two existing counter-rotating vortices near the bed during each half cycle of the wave period. In conclusion, it was noted that the vortical flow at the boundary induces significant advective solute transport perpendicular to the seabed, which greatly exceeds diffusional transport.

[Ourmières and Chaplin, 2004] observed different patterns forming over rigid impermeable ripple beds in visualization experiments, where they varied wave-induced flow regimes and ripple slopes (height to length ratio). The flow pattern above the ripple surface was found to be strongly influenced by the wave scenario and the ripple shape, with a dependency on the Taylor number, which, in turn, relies on the wave orbital amplitude, frequency, ripple height, and wavelength. The quotient of Taylor number and orbital amplitude to ripple wavelength ratio was identified as an indicator for different two- and three-dimensional flow patterns. However, strong flow oscillations inducing turbulent flow and therefore quick mixing of the dye were not within the scope of that study.

Turbulent oscillating flow over sand ripples was examined by [Barr, 2004] conducting three-dimensional direct numerical simulations based on a model developed by [Winters et al., 2000]. The results visually demonstrated that the presence of sand ripples enhances the dissipation rate of shoaling wave energy, as opposed to the flow over a flat bed. They showed the impact of the ripple shape (here: sinusoidal, Gaussian, and "steep") to modify the mean flow field, influencing both the induced drag and the rates of energy loss. Furthermore, they observed, that when the flow reverses, shear instabilities close to the boundary, resulting in vortex formation behind the ripple crest, lead to a continuously turbulent boundary layer. The presence of ripples therefore induces significantly higher turbulence levels and dissipation rates in the boundary layer compared to flows over a smooth boundary.

The spatial and temporal structure of flow, turbulence, and stress over equilibrium state, and thus temporally stable, sand ripples under oscillating flow conditions was investigated by [Hare et al., 2014] using a Doppler profiler in a laboratory wave tank experiment. The measurements were used to explore how the lee vortex, turbulent kinetic energy, Reynolds stress, and turbulence production coevolve across different phases. The presented phase-averaged results were derived from velocity fluctuations. Among their conclusions was the finding that turbulence production over a ripple wavelength originated from both the bottom and the lee vortex, which acted as sources of turbulence.

Hence, in addition to shear, which is also present at a flat sediment-water interface, flow separation and vortex formation at a rippled seabed contribute significantly to the production of turbulence within the flow field. This turbulence drives turbulent transport, which, following the argumentation of [Berg et al., 2003], predominantly determines the vertical distribution of discharging scalar quantities within the water column. Figure 2.8 summons the phenomena that, based on the literature reviewed above, affect the flow across and above a rigid permeable, rippled sediment-water interface under oscillating

flow conditions, considering the temporal and spatial scales addressed in this study.

This thesis hypothesizes that the local concentration values within the water column are not solely reliant on discharge rates; rather they are substantially influenced by turbulent transport and mixing within the boundary layer. Consequently, investigating bottom topography as a critical factor in turbulence formation and turbulent transport is of particular interest for experimental investigations. An established method to capture high-resolution (temporal and spatial) velocity fields and thereby velocity fluctuations is PIV, which was used to characterize oscillating flow above rippled seabeds in various laboratory studies [Malarkey et al., 2015], [Yuan and Wang, 2018], [Yuan and Wang, 2019]or even in the field [Nayak et al., 2015]. To quantify the turbulent transport of a passive scalar by turbulent fluxes, measurements of the concentration (fluctuations) are required additionally. Therefore, LIF measurements will be obtained simultaneously as applied e.g. in the chemical engineering studies on turbulent mass transfer and mixing by [Hjertager et al., 2003] or [Hjertager Osenbroch et al., 2008] or in the study by [Reidenbach et al., 2010], who used combined PIV and LIF measurements to investigate the transport of a passive scalar under unidirectional flow conditions over rough beds by calculating vertical turbulent fluxes and turbulent kinetic energy.
The subsequent chapter will provide the fundamental fluid mechanical knowledge to understand the definition and mathematical determination of turbulent fluxes, turbulent kinetic energy and the above-mentioned experimental methods that were utilized to obtain the respective necessary quantities.

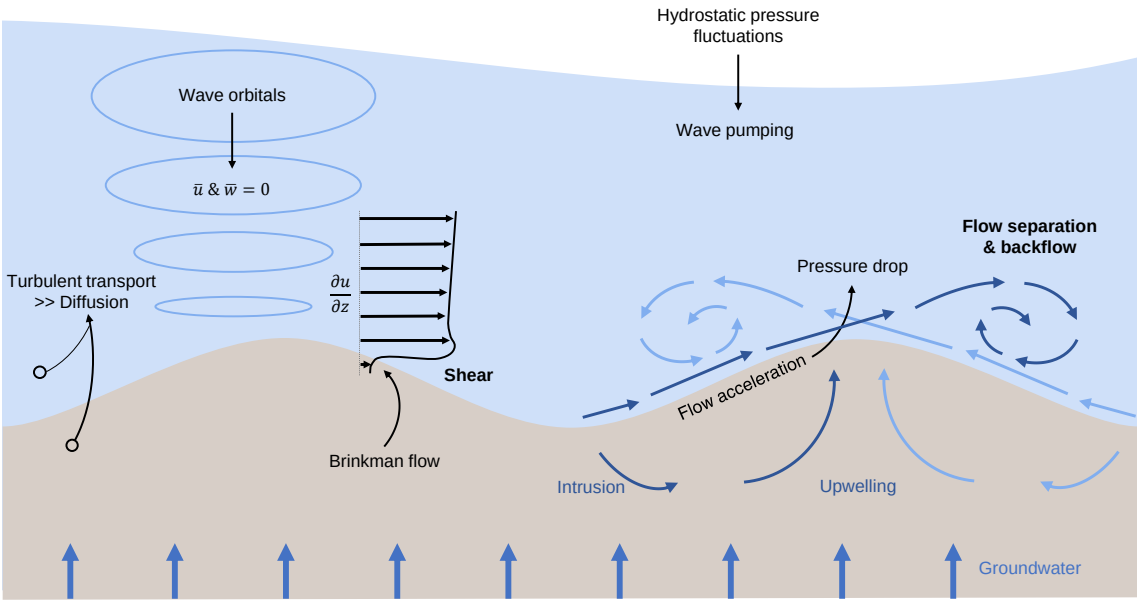

Figure 2.8: Graphical summary of phenomena affecting the flow across and above a permeable rippled sediment-water interface under oscillating flow conditions: On very small spatial scales, diffusion occurs in the sediment and the water column; Wave orbital motion averages out to zero over a complete wave period and does therefore not contribute to vertical net transport within the water column, but wave induced hydrostatic pressure fluctuations cause periodical pore and groundwater discharge from the permeable seabed (wave pumping); Shear - induced by velocity differences at the sediment-water interface - contributes to the production of turbulence in the bottom boundary layer; Flow acceleration at the ripple stoss side and deceleration at the lee side induce pressure variations driving intrusion and upwelling of pore and groundwater through the permeable seabed; Flow separation and vortex formation at the downstream slope induce additional advective transport and contribute to the production of turbulence, which in turn promotes turbulent transport.

Chapter 3

Fluid Mechanical Fundamentals

Most transport and mixing processes in engineering applications and the environment are driven by fluid flows. The physics of flowing fluids, referred to as fluid dynamics, along with the physics of stationary fluids, referred to as fluid statics, constitute the field of fluid mechanics. The term "fluid" encompasses all substances that continuously deform under the influence of shear forces, and are therefore capable of flowing: liquids, gases, and plasma. In fluid mechanics, the flowing fluid is considered a continuum, meaning that the molecular structure of the flowing medium is disregarded, as the molecules' mean free path is small compared to the macroscopic dimensions of the flow field. The characteristic physical quantities of the flow field, such as the velocity vector $\mathbf{u} = u_i = [u, v, w]^T$, pressure p, density ρ, and temperature, are assumed to be continuous functions of the position in Cartesian spatial coordinates $\mathbf{x} = x_i = [x, y, z]^T$ and time t. [Oertel et al., 2012]
When investigating the behaviour of a passive scalar within the flow field, these quantities can be supplemented with an additional variable to represent the scalar field.
The challenge of fluid mechanics lies in understanding, experimentally investigating, and predicting the behaviour of fluid quantities and their interactions.
This chapter aims to provide the mathematical and physical basis necessary to follow the determination of the quantities presented in Chapter 4 and the results presented in Chapter 5. It includes the fundamental equations of fluid mechanics, an explanation of turbulence as a driver of transport, and the measurement techniques employed in this study to capture the flow variables essential for investigating these phenomena.

3.1 Conservation Laws in Fluid Mechanics

The behaviour of fluids is governed by the conservation of mass, momentum, and energy stating that none of these quantities can be created or destroyed in a closed system. These fundamental physical principles are essential for describing and predicting fluid flow dynamics.
For incompressible, constant-density fluids, the law of conservation of mass, often referred to as the continuity equation, is given by Equation 3.1.

$$\nabla \cdot \mathbf{u} = \frac{\partial u_i}{\partial x_i} = 0 \tag{3.1}$$

The law of conservation of (thermal) energy is not relevant to the scope of this thesis, as the experiments were conducted at constant temperature and thus isothermal conditions. The conservation of momentum is described by the Navier-Stokes equations, which are derived from Newton's second law of motion. These equations mathematically account for

the forces acting on a fluid element, including pressure p, external forces f_i, and viscous forces arising within the fluid due to its viscosity ν. The Navier-Stokes-Equations for incompressible, Newtonian fluids in an unsteady flow are given by Equation 3.2.

$$\frac{Du_i}{Dt} = f_i - \frac{1}{\rho}\frac{\partial p}{\partial x_i} + \nu\frac{\partial^2 u_i}{\partial {x_j}^2} \tag{3.2}$$

The left side corresponds to the velocity's substantial derivative, also known as material derivative, which is defined by Equation 3.3. It describes the rate of change of the velocity component as experienced by a fluid parcel moving with the flow. [Spurk and Aksel, 2010], [Pope, 2000].

$$\frac{D}{Dt} \equiv \frac{\partial}{\partial t} + (\mathbf{u} \cdot \nabla) = \frac{\partial}{\partial t} + u_i\frac{\partial}{\partial x_i} \tag{3.3}$$

When additionally considering a passive scalar, the corresponding conservation equation for this variable is given by Equation 3.4 with D_m standing for the molecular diffusivity [Pope, 2000]. A scalar quantity is considered "passive", as its presence does not cause a change in the dynamics of the fluid motion [Socolofsky and Jirka, 2005]. In this study, the passive scalar field corresponds to the concentration field of a discharged tracer fluid and is therefore denoted by c.

$$\frac{Dc}{Dt} = \frac{\partial}{\partial x_j}\left(D_m\frac{\partial c}{\partial x_j}\right) \tag{3.4}$$

The conservation laws provide an exact description of how momentum and scalar quantities are transported and distributed within a fluid under the influence of various forces and flow conditions. However, when turbulence is present, directly solving the Navier-Stokes equations becomes highly challenging due to the need to resolve a wide range of spatial and temporal scales.

3.2 Turbulent Transport

In this thesis, the turbulent transport of a discharging tracer fluid was quantified. In general, transport refers to the movement of physical properties - such as momentum or heat - and substances - such as particles or solutes - from one location to another within a fluid medium. Mixing, on the other hand, describes the process of combining two or more substances to achieve a uniform distribution of their properties within a given volume of fluid. Therefore, transport mechanisms facilitate mixing. Both transport and mixing occur on different length scales and are driven by distinct forces and mechanisms. [Kraume, 2012]

Transport is typically quantified by a flux, which is derived from the product of the gradient of a physical quantity and the transport coefficient. The gradient represents the driving force, while the transport coefficient represents the medium's ability to conduct the transported quantity.

The driving force varies depending on the transported quantity. Momentum transport is driven by the transversal velocity gradient, while heat and mass transport are driven by temperature and concentration gradients, respectively.
The transport coefficient, however, additionally depends on the type of transport process, which can be either molecular, convective, or turbulent.
The molecular transport of momentum is enabled by the fluid's viscosity. Heat transport through molecular motion is facilitated by the thermal conductivity of the medium, which can be either fluid or solid. Mass transport by molecular motion is primarily determined by the diffusion coefficient. Diffusion results from the random motion of suspended particles (Brownian motion) and occurs in static and dynamic fluids. [Bird et al., 2007]
On macroscopic scales, the transport of momentum, heat, and mass is primarily driven by convection and turbulence.
Convective transport only occurs in flowing fluids and describes the bulk movement of the fluid, which carries momentum, heat, or mass along with the flow. In the direction of flow, convective transport significantly exceeds diffusive transport.
In turbulent flows, turbulent transport occurs alongside molecular diffusion and convective transport. The turbulent flow generates vortices, which travel relatively long distances, carrying fluid elements along with them and enhancing the mobility of individual molecular groups. Since the minimum vortex size is many times larger than the mean free molecular path length, the interfacial area between the two fluids expands. This promotes molecular diffusion and leads to a substantial increase in mixing efficiency [Kraume, 2012]
This reveals that turbulent transport and mixing are not isolated phenomena but interact with convective and molecular processes. To accurately quantify the transport attributed to turbulence, a deeper understanding of turbulent flows is essential.

3.2.1 Characteristics of Turbulent Flows

[Reynolds, 1883] demonstrated through his visualization experiments that fluid flows occur in two fundamentally distinct forms: laminar and turbulent. He injected a coloured liquid into a pipe flow through a fine tube. At low flow velocities, a thin coloured thread forms, floating parallel to the axis of the pipe. This characterizes laminar flow, where different layers of the fluid can flow alongside each other with minimal exchange of fluid elements. However, when the flow velocity exceeds a certain threshold, the experimental outcome is significantly different. The injected coloured thread exhibits strong irregular cross-movements, quickly leading to its complete disintegration. This observation is characteristic of turbulent flow, where the mean flow is super-positioned with strong irregular, and therefore random, fluctuation movements that result in intense mixing perpendicular to the flow direction.
These observations led to Reynold's derivation of the Reynolds-number Re. This metric describes the ratio of inertial to viscous forces and is defined by Equation 3.5, where u denotes a characteristic velocity of the flow, L corresponds to the characteristic length dimension of the body being flowed around or through. The fluid properties are given by the density ρ and the dynamic viscosity η or rather the kinematic viscosity $\nu = \eta/p$. At

low Reynolds numbers, a flow tends to be laminar, while at high Reynolds numbers, even small disturbances can lead to the development of turbulence, meaning that the flow is unstable. [Schlichting et al., 2006], [Oertel et al., 2012],[Sigloch, 2017], [Pope, 2000]

$$Re = \frac{\rho \cdot u \cdot L}{\eta} = \frac{u \cdot L}{\nu} \tag{3.5}$$

In a wave-dominated flow field, a wave Reynolds number Re_w is used to characterize the flow as being laminar or turbulent. Equation 3.6 defines the wave Reynolds number, where a corresponds to the wave amplitude and $\omega = 2\pi/T$ denotes the angular frequency. [Nielsen, 1992]

$$Re_w = \frac{a^2\omega}{\nu} = \frac{a^2 2\pi}{T\nu} \tag{3.6}$$

All of this means, that with increased dimensions, velocities, or decreased viscosity - and in the case of an oscillating flow field, with increased wave amplitude and frequency - a flow tends to transition from laminar to turbulent, and therefore from steady, regular and predictable to unsteady, irregular and predominantly unpredictable.
More precisely, turbulent flows are characterized by the following distinct features:

- Time-dependent: Turbulent flows are inherently unsteady/non-stationary. However, flows with unchanged mean velocity over time can be denoted as quasi-stationary.
- Irregular: Turbulent flows exhibit random, chaotic, and unpredictable fluctuations in velocity and pressure across both time and space.
- Involving rotation: Velocity gradients in turbulent flows generate vorticity, which is a measure of the local rotation in the fluid. Turbulence also involves the formation of eddies - swirling motions of fluid - that are inherently rotational and exist at various scales.
- Three-dimensional: In turbulent flows, energy is transferred from larger eddies to smaller ones through a process known as the energy cascade. This involves the breakdown of large-scale turbulent structures into progressively smaller structures, a process occurring in all spatial directions.
- Dissipative: At the smallest scales (Kolmogorov scales), kinetic energy is irreversibly converted into thermal energy due to viscous forces within the fluid.
- Intensively mixing: These characteristics collectively enhance fluid transport and mixing in turbulent flows compared to laminar flows.

Turbulence is prevalent in nature and technical applications. Yet, experimentally determining turbulence, simulating it computationally, or controlling it in practical applications remain substantial challenges in modern fluid mechanics. This is because the turbulent velocity components $u_i(x,t)$ behave as random variables, necessitating a statistical approach for their description and analysis. [Sigloch, 2017], [Pope, 2000]

This inherent complexity makes analytical solutions to the Navier-Stokes equations impossible for turbulent flows, requiring the use of numerical methods for their analysis and prediction. Direct numerical simulation (DNS) resolves all scales of motion within turbulent flows. However, it is computationally intensive in more complex scenarios. Alternatively, large eddy simulation (LES) focuses on accurately resolving large-scale flow movements while approximating small-scale motions with turbulence models. For specific quantitative properties, the Reynolds-averaged Navier-Stokes equations (RANS) equations provide a more efficient approach. By averaging the unsteady nature of turbulent flow over time, RANS introduces unknown terms that must be modelled, requiring less computational effort compared to DNS and LES, making it suitable for large domains [Ferziger and Perić, 2008].

3.2.2 Reynolds Decomposition

The Reynolds decomposition following [Reynolds, 1895] is a common method to mathematically describe turbulent flow fields. The superposition of the mean flow field quantities with the random fluctuation component is represented by Equations (3.7) and (3.8).

$$u_i(x_j,t) \equiv \overline{u_i}(x_j,t) + u_i'(x_j,t) \tag{3.7}$$

$$p(x_j,t) \equiv \overline{p}(x_j,t) + p'(x_j,t) \tag{3.8}$$

By applying the Reynolds decomposition to the Navier-Stokes equations for incompressible, unsteady flow (3.2) and then temporally averaging the resulting equations, this results in the RANS (3.9). Note that, through temporal averaging, the non-linear terms involving the fluctuation components are retained, while the linear terms of these fluctuations vanish.

$$\rho\frac{D\overline{u_i}}{Dt} = \rho\frac{\partial\overline{u_i}}{\partial t} + \rho\overline{u_j}\frac{\partial\overline{u_i}}{\partial x_j} = \rho k_i - \frac{\partial\overline{p}}{\partial x_j} + \eta\frac{\partial^2\overline{u_i}}{\partial {x_j}^2} - \frac{\partial\left(\rho\overline{u_i'u_j'}\right)}{\partial x_j} \tag{3.9}$$

The additional term arising at the right-hand side of the balance, represents the momentum transport induced by turbulence. This term includes the covariances of the velocity fluctuations $\rho\overline{u_i'u_j'}$ most commonly known as Reynolds stress tensor τ_{ij} detailed in Equation 3.10. [Spurk and Aksel, 2010], [Pope, 2000]

$$\boldsymbol{\tau} = \tau_{ij} = -\rho\overline{u_i'u_j'} = \rho\begin{bmatrix}\overline{u'^2} & \overline{u'v'} & \overline{u'w'}\\ \overline{v'u'} & \overline{v'^2} & \overline{v'w'}\\ \overline{w'u'} & \overline{w'v'} & \overline{w'^2}\end{bmatrix} \tag{3.10}$$

Half the trace of the Reynolds stress tensor gives the turbulent kinetic energy TKE quantifying the mean kinetic energy per unit mass in the fluctuating velocity field, as given by Equation 3.11 [Pope, 2000]. In the present study, this quantity serves as a measure of turbulence.

$$TKE = \frac{1}{2}\overline{u_i' u_i'} \tag{3.11}$$

The Reynolds stress tensor in Equation 3.10 introduces nine additional unknowns, which can be reduced to six unknown Reynolds stresses due to the symmetry of the tensor.

Analogous to the momentum conservation, the conservation equation for a passive scalar can also be derived from the Reynolds decomposition based on Equation 3.4. Equation 3.12 gives the Reynolds-averaged conservation law for the scalar field. Notably, a term that includes the unknown fluctuation values of the flow field u_i' and c' also arises here [Pope, 2000].

$$\frac{\partial \overline{c}}{\partial t} + \overline{u_i}\frac{\partial \overline{c}}{\partial x_j} = \frac{\partial}{\partial x_j}\left(D_m \frac{\partial \overline{c}}{\partial x_j}\right) - \frac{\partial(\overline{u_i' c'})}{\partial x_j} \tag{3.12}$$

The covariance of the velocity field fluctuations with the scalar field fluctuations results in a vector known as the turbulent scalar flux, also termed Reynolds flux, see Equation 3.13. It represents the flow rate per unit area of the scalar caused by the fluctuations of the velocity field in addition to the convective and diffusive fluxes [Pope, 2000], [Bird et al., 2007]. In other words, the turbulent scalar flux quantifies turbulent transport of the concentration c [Bonan, 2015] in the respective coordinate direction of the flow field and will hereafter be referred to as turbulent flux.

$$\mathrm{cov}(u_i, c) = \overline{u_i' c'} \tag{3.13}$$

The additional unknowns arising from the RANS equations lead to the issue that the number of variables exceeds the number of available equations, which is known as the closure problem as the system of equations is not closed. This issue remains unresolved and can only be addressed through significant simplifications and hypotheses. Consequently, the terms in the conservation equations involving unknown fluctuation quantities are modelled using empirical assumptions. [Oertel et al., 2012].

3.2.3 Turbulence Modelling

Turbulence models aim to establish a relationship between the fluctuating and the mean flow field quantities in the RANS equations to address the closure problem.
One commonly employed method in oceanographic simulations, implicating large computational domains, is the application of one-dimensional turbulence models based on the turbulent-viscosity and the gradient-diffusion hypotheses first introduced by [Boussinesq, 1878]. Momentum, heat, and mass transport occur at a microscopic scale due to molecular diffusion processes. These transport phenomena are characterized by their respective coefficients: viscosity, thermal conductivity, and diffusion coefficient. They are widely known as the stress-rate-of-strain relation for Newtonian fluids, Fourier's law of heat conduction and Fick's law of molecular diffusion.

Analogously, the turbulent viscosity, also termed eddy viscosity, the turbulent thermal conductivity, and the turbulent diffusivity, also termed eddy diffusivity, are introduced. These quantities are not directly measurable but serve as analogue quantities representing phenomenological relationships that are so far not precisely known. They describe a proportional relationship between the covariances of the flow field fluctuations and the mean flow field quantities.

For the turbulent-viscosity hypothesis, it is assumed that turbulent apparent stresses result from macroscopic momentum exchange in the same manner that viscous shear stresses arise from molecular momentum exchange. By introducing the turbulent viscosity, only this single parameter needs to be modelled as a function of the average flow, instead of the six unknown Reynolds stresses. Unlike molecular viscosity, turbulent viscosity is not an inherent property of the fluid material but rather a property of the turbulence within the flow system. [Pope, 2000], [Oertel et al., 2012], [Spurk and Aksel, 2010], [Sigloch, 2017]

For the two-dimensional turbulent boundary layers examined in this thesis and the respectively defined coordinate system with $x_1 = x$ as the horizontal direction and $x_2 = z$ for the vertical direction, the turbulent viscosity hypothesis is given by Equation 3.14 with $\nu_t = \eta_t/\rho$. This formula relates the Reynolds stresses $\overline{u'w'}$ to the vertical gradient of the horizontal velocity u through the turbulent viscosity ν_t. The gradient-diffusion hypothesis is given by Equation 3.15 relating the vertical turbulent flux $\overline{w'c'}$ to the vertical gradient of the concentration c through the turbulent diffusivity D_t. These simplifications are valid because the mean velocity in a turbulent boundary layer is primarily in the x_1-coordinate direction, while fluctuations in the mean quantities occur mainly in the x_2-coordinate direction. [Pope, 2000]

$$\overline{u'w'} = -\nu_t \frac{\partial \overline{u}}{\partial z} \tag{3.14}$$

$$\overline{w'c'} = -D_t \frac{\partial \overline{c}}{\partial z} \tag{3.15}$$

While these hypotheses provide a foundational understanding of turbulent flows, they rely on the assumption of constant turbulent viscosity and diffusivity, which cannot be valid in boundary-layer flows because the Reynolds stress and flux respectively must vanish as it approaches the wall [Spurk and Aksel, 2010]. To address this, Prandtl's mixing length hypothesis from 1925 introduces a length scale l_t that characterises the distance over which fluid parcels mix effectively due to turbulence [Pope, 2000].

This hypothesis assumes that the turbulent apparent stresses arise from macroscopic momentum exchange in the same way that viscous shear stresses arise from molecular momentum exchange. In kinetic gas theory, the kinematic viscosity ν is proportional to the mean free path of the molecules and the magnitude of their mean velocity. Prandtl's mixing length hypothesis transfers this concept to turbulent motion, supposing a corresponding relationship between the turbulent viscosity ν_t, a characteristic velocity $l_t|\partial\overline{u}/\partial z|$, and the turbulent mixing length l_t, as specified by Equation 3.16. This relationship ensures that the model depends on the velocity gradient and is illustrated in Figure 3.1.

$$\nu_t = {l_t}^2 \left| \frac{\partial \overline{u}}{\partial z} \right| \tag{3.16}$$

The concept of the mixing length hypothesis is based on the idea, that a fluid parcel's movement in a turbulent flow can be considered an enlarged version of the thermal molecular motion in gases. In addition to its primary motion in the flow direction $\overline{u}$, the fluid parcel exhibits disordered, statistically random secondary motions in all directions. In doing so, it extracts mechanical energy from the main flow, which, upon the parcel's decay, undergoes an energy cascade into progressively smaller units until it dissipates into heat. The turbulent mixing length l_t represents the distance over which the individual parcel travels as a relatively coherent structure until it loses its individuality through collisions and mixing with other fluid parcels. [Sigloch, 2017]

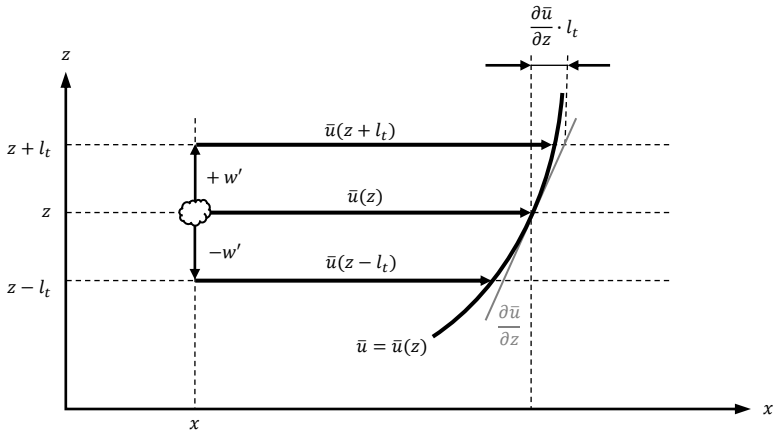

Figure 3.1: Scheme of the relationship between the characteristic velocity of a fluid parcel and its turbulent mixing length according to [Sigloch, 2017] : The parcel moves with w' in the z-direction and covers the turbulent mixing length l_t. Through its momentum, it causes a velocity fluctuation u', which has the magnitude of $l_t \left| \frac{\partial \bar{u}}{\partial z} \right|$

Extending this concept to the turbulent transport of a passive scalar, which in this study is represented by the concentration c, the mixing length similarly influences the turbulent diffusivity D_t, as given by Equation 3.17. Thus, the turbulent scalar flux can be expressed by Equation 3.18 [Bird et al., 2007]. The turbulent flux $\overline{w'c'}$ is given by the product of $-D_t$, analogous to a transport coefficient, and the concentration gradient in z-direction.

$$D_t = {l_c}^2 \left| \frac{\partial \overline{u}}{\partial z} \right| \tag{3.17}$$

$$\overline{w'c'} = -D_t \frac{\partial \overline{c}}{\partial z} = -{l_c}^2 \left| \frac{\partial \overline{u}}{\partial z} \right| \frac{\partial \overline{c}}{\partial z} \tag{3.18}$$

Consequently, the mixing length hypothesis not only refines the understanding of momentum and mass transfer in turbulent flows but also enhances the modelling of scalar transport, offering a comprehensive method for analysing both velocity and concentration fields in turbulent boundary layers. However, for modelling based on this semi-empirical turbulence theory, the mixing length must be determined experimentally.

3.2.4 Phase Averaging

As already pointed out in Section 3.2.1, turbulent flows are inherently non-stationary, but can be considered quasi-stationary if the mean velocity remains constant over time. However, in this study, the mean velocity oscillates due to wave motion, leading to periodic changes. Thus, the velocity is time-dependent or more precisely, phase-dependent.
Applying the Reynolds decomposition appropriately to this case, the instantaneous velocity $u_i(x_j,t)$ is expressed as the sum of the time-averaged velocity $\overline{u_i}(x_j)$, the time-dependent ordered component $\widetilde{u_i}(x_j,t)$, representing the periodic velocity variation, and the time-independent component $u_i'(x_j,t)$, representing the stochastic, turbulence-induced velocity fluctuations. The first two terms can be summarized as the phase-averaged velocity $\langle u_i(x_j,t)\rangle$, representing the average velocity within a distinct phase of the wave cycle, as shown in Equation 3.19. This relationship is graphically illustrated in Figure 3.2.

$$u_i(x_j,t) = \overline{u_i}(x_j) + \widetilde{u_i}(x_j,t) + u_i'(x_j,t) = \langle u_i(x_j,t)\rangle + u_i'(x_j,t) \tag{3.19}$$

To obtain the phase-averaged velocity $\langle u_i(x_j,t)\rangle$ from experimental data, the velocity field values $u_i(x,t)$ are averaged at the same phase within the wave cycle. [Schlichting et al., 2006]

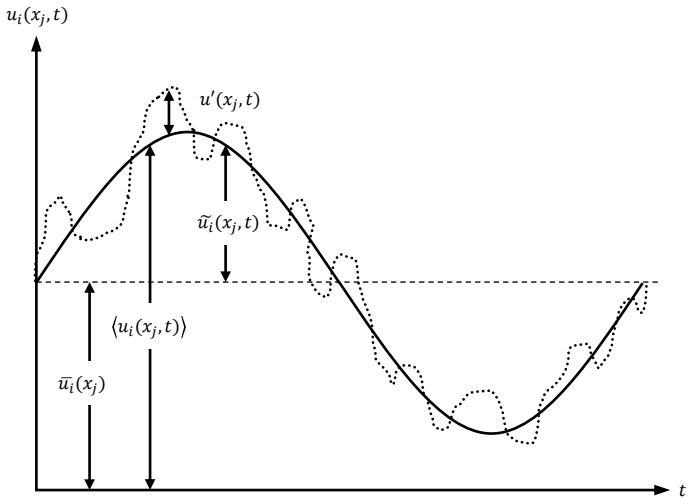

Figure 3.2: Graphical illustration of the Reynolds decomposition of a turbulent oscillating flow field quantity u_i measured over time t at a distinct position x_j, adapted from [Rodi, 1993]. The dotted line represents the instantaneous value $u_i(x_j,t)$, the solid line represents the phase average $\langle u_i(x_j,t)\rangle$, and the dashed line represents the time average $\overline{u_i}(x_j)$. The difference between the phase average and time average corresponds to the periodic velocity variation $\widetilde{u_i}(x_j,t)$ and the difference between the instantaneous value and the phase average corresponds to the stochastic turbulent fluctuation $u_i'(x_j,t)$.

To quantify turbulent fluxes according to 3.13, fluctuation values of the vertical velocity w and the concentration c must be calculated based on the experimental data. To further assess the occurrence of turbulence using the turbulent kinetic energy defined in Equation 3.11, fluctuation values of the horizontal velocity u are also required. For an oscillating flow field, the fluctuation values of these three quantities are calculated based on Equation 3.19 converting it to Equation 3.20, which is valid for an arbitrary quantity γ. The space-

and time-dependent fluctuation value $\gamma'(x_i, t)$ results from the difference between the instantaneous value of this quantity $\gamma(x_i, t)$ and the corresponding phase-averaged value $\langle\gamma(x_j, t)\rangle$. The application of this formula to the measurement data is extensively described in Section 4.4.

$$\gamma'(x_j, t) = \gamma(x_j, t) - \langle\gamma(x_j, t)\rangle \text{ with } \gamma \in \{u, w, c\} \tag{3.20}$$

3.3 Optical Measurement Techniques Employed

To quantify turbulent fluxes, it is essential to measure the time-resolved velocity and concentration fields within the mixing region with high temporal resolution. Therefore, the experimental method of simultaneous velocity and concentration field measurements using particle image velocimetry and laser-induced fluorescence, respectively, was chosen for this study.

3.3.1 Particle Image Velocimetry

Particle image velocimetry (PIV) is a laser optical measurement technique used for obtaining velocity fields by tracking the displacement of tracer particles over a defined time interval. Therefore, reflective particles, similar in density to the flowing fluid, are introduced into the investigated flow. This process is termed seeding. Proper seeding is crucial, as it ensures that the particles are uniformly distributed and accurately track the flow dynamics. Within the three-dimensional flow domain, a cross-sectional plane is established by a laser light sheet, defining the measurement area. A double laser pulse then illuminates the tracer particles as they pass through this region. The time gap between these light pulses Δt is adjusted according to the prevailing flow velocities. The scattered light from the particles is captured by a high-resolution charge-coupled device (CCD) camera, as illustrated in Figure 3.3, obtaining double-frame images for the subsequent analysis.
In post-processing, the acquired 2D double-frame images are divided into interrogation area (IA). For each IA, a displacement vector is computed by comparing particle positions between the two images of the double-frame, considering shifts in the x- and z-direction. Cross-correlation values R_{II} are calculated for each shift, as defined by Equation 3.21. $R_{II}(\Delta x, \Delta z)$ represents the cross-correlation value for a given shift $(\Delta x, \Delta z)$. The intensity value $I(m, n)$ corresponds to the pixel intensity at coordinates (m, n) within the IA in the first image of the double-frame, where m is the pixel index in the x-direction and n is the pixel index in the z-direction. $I'(m + \Delta x, n + \Delta z)$ represents the intensity at pixel coordinates $(m + \Delta x, n + \Delta z)$ within the corresponding IA in the second image, which has been shifted by $(\Delta x, \Delta z)$. The summation over m and n spans the entire IA, with M and N defining the number of pixels in the x- and z-directions, respectively, and thus determining the size of the IA.

$$R_{II}(\Delta x, \Delta z) = \sum_{m=0}^{M-1} \sum_{n=0}^{N-1} I(m, n) \cdot I'(m + \Delta x, n + \Delta z) \tag{3.21}$$

A high R_{II} value results from a displacement where the particle positions in the correlated IAs coincide. Thus, the cross-correlation function statistically quantifies the level of agreement at a specific displacement. The maximum correlation value identifies the displacement corresponding to the best alignment, facilitating the estimation of particle displacements. To relate the particle displacement in pixels to a metric length scale, a scaling factor must be determined through calibration. Combining the displacement vector with Δt yields the velocity vector for each IA. [Raffel et al., 2018], [Merzkirch, 2011]
The IA size significantly affects the accuracy and reliability of velocity vector calculations. Larger IAs capture more particles, thereby enhancing statistical reliability, but may average out small-scale flow features. The number and spacing of IAs are determined by the grid step size, which is defined as the number of pixels between the centres of adjacent IAs. The grid step size directly controls the spacing between vectors: smaller grid steps result in more computed vectors, thus increasing spatial resolution. However, this also demands greater computational power and is also limited by physical reasons such as the camera resolution. Furthermore, smaller grid steps reduce the number of particles within each IA, leading to less reliable correlation results. Additionally, decreasing the size of the IAs can worsen the signal-to-noise ratio, increasing the risk of inaccurate velocity vectors. Therefore, it's essential to balance spatial resolution with measurement accuracy to ensure reliable results.
If the grid step size is smaller than the IA size, the IAs will overlap. Increasing overlap is another approach to enhance the spatial resolution of the velocity field by providing more vectors and smoothing transitions between neighbouring vectors, though this also increases computational demands and excessive overlap can lead to a loss of independent information between neighbouring vectors.
Validation techniques are employed to prevent outliers from distorting velocity measurements. One such method is the peak height ratio validation, which calculates the ratio between the two highest correlation peaks in the image cross-correlation. This ratio compares the height of the main correlation peak, representing the most probable particle displacement, to the height of secondary peaks, which could be due to noise or spurious correlations. A higher peak-to-height ratio indicates a more reliable measurement, as the primary peak is more distinct from the background noise. For a vector to be validated, the peak height ratio must exceed a specified threshold. If this validation criterion is not met, the corresponding vector is rejected and replaced with the median of valid neighbouring vectors within a defined neighbourhood. This process improves the robustness of displacement measurements, particularly in regions with low particle density or poor image quality. However extensive neighbourhoods may excessively smooth the data, potentially hiding important displacement details, while an excessively high peak-to-height ratio threshold might eliminate valid vectors with smaller displacements, leading to incomplete or inaccurate velocity measurements. Therefore, carefully balancing the validation criteria is essential to ensure both accurate measurements and the preservation of important displacement details. [Dantec Dynamics A/S, 2021]

3.3.2 Laser-Induced Fluorescence

Laser-induced fluorescence (LIF) is an emission spectroscopy technique where fluorescence is induced by a laser pulse. Upon excitation of a fluorescent molecule, an electron transitions from its ground state to a higher-energy state. Subsequently, as the electron returns spontaneously to its ground state, it emits a photon. The emitted fluorescence light is captured and recorded using a CCD camera [Hugenschmidt, 2007].
To selectively capture light with the fluorescence-specific wavelength, optical bandpass filters are placed in front of the camera. LIF finds diverse applications, including the measurement of concentration distributions of a fluorescent tracer medium. In this context, the local fluorescence intensity F is proportional to the local concentration c of a dye, as shown in Equation 3.22. The proportionality factor depends on the excitation intensity I and the saturation intensity of the dye I_{sat}. When the excitation intensity is significantly below the dye's saturation intensity, an approximately linear relationship between fluorescence intensity and concentration can be assumed, as described in Equation 3.23 [Crimaldi, 2008].

$$F \sim \frac{I}{1 + \frac{I}{I_{sat}}} \cdot c \tag{3.22}$$

$$I \ll I_{sat} \rightarrow F \propto I \cdot c \tag{3.23}$$

The proportionality factor can be determined using a calibration curve. For this purpose, several measurement points are taken with known concentration values. The calibration curve is derived by linear regression of these measurement points. Consequently, each pixel brightness detected by the CCD camera can be associated with a concentration value during data analysis.
In fluid flow studies, the most common application of LIF is two-dimensional planar laser-induced fluorescence (PLIF). Here, a laser light sheet is generated within the flow field, and the CCD camera is positioned perpendicular to the laser light sheet [Crimaldi, 2008]. Due to their compatible setup, PIV and PLIF measurements can be easily combined. In this configuration, the same field of view (FoV) is simultaneously captured by two cameras sharing the same FoVs, as illustrated in Figure 3.3. This facilitates the simultaneous measurement of velocity and concentration fields enabling the correlation of u_i and c to determine turbulent fluxes and further quantities. However, it is necessary to use optical filters to ensure that the two measurement methods do not interfere with each other.

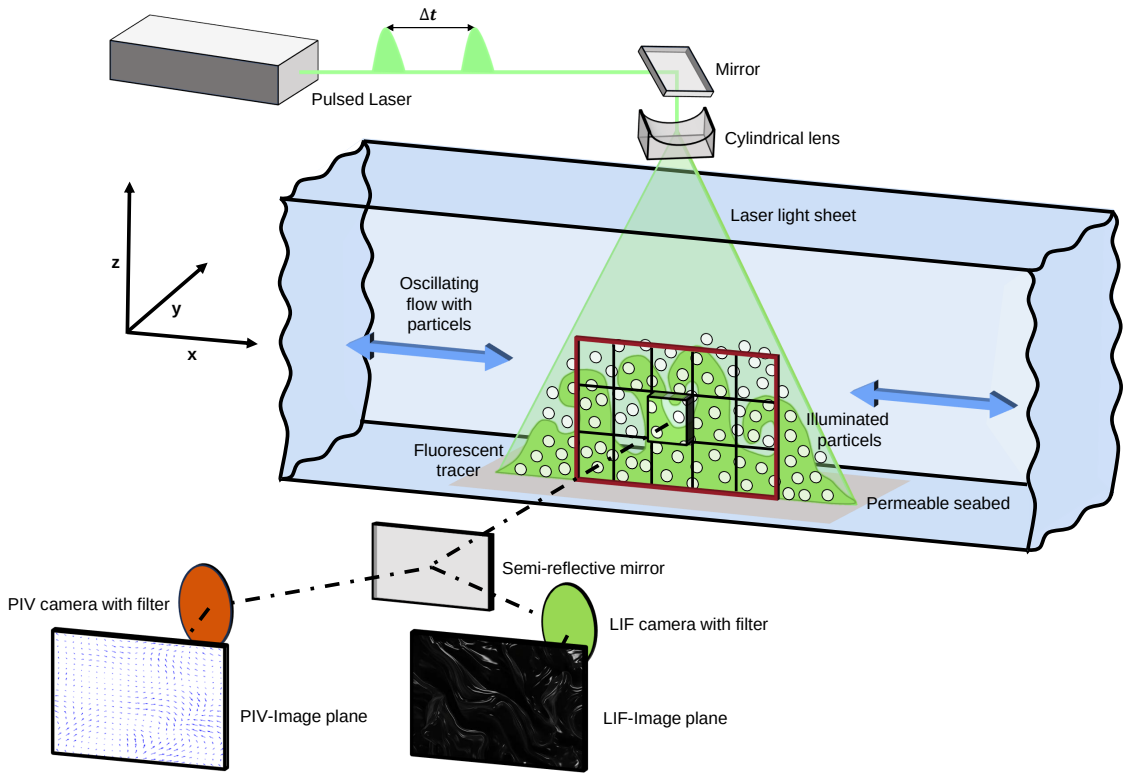

Figure 3.3: Schematic representation of the PIV-LIF measurement setup adapted from [Raffel et al., 2018] and [Dantec Dynamics A/S,] to align with the experimental setup of this study: An oscillating flow seeded with particles passes through the laser light sheet, and the scattered light from the double-exposed particles is detected by the PIV camera. Simultaneously, the distribution of fluorescent tracer dye emerging from a permeable seabed is captured within the flow by the LIF camera, enabling an integrated analysis of flow dynamics and dye transport.

Chapter 4

Materials and Methods

This chapter gives a comprehensive overview of the experimental setup, the experimental boundary conditions, and the PIV-LIF measurement procedure. Furthermore, it will elucidate the subsequent analysis of the experimentally obtained velocity and concentration field data to facilitate the evaluation of flow topography interaction on the vertical turbulent transport of a discharging tracer fluid.

4.1 Experimental Setup

The measurement results presented in this thesis were obtained in a tank located at the Chair of Fluid Mechanics at the University of Rostock, which was initially designed for experiments in unidirectional stratified flows. [Karow, 2019] modified this tank to accommodate oscillating flows. The wave tank measures 4 m in length, 0.8 m in width, and 1 m in depth. After the modification, it comprised three main components: a wave generator, a flow section, and a wave absorber, as shown in Figure 4.1. At one end of the tank, waves can be generated using a piston-type wave generator developed by [Heimbuch, 2014]. It consists of a vertical steel panel measuring 0.77 meter x 0.65 m and moving parallel to the longitudinal tank axis. This type of wave generator moves the entire water column, facilitating water movement at the seabed-water interface, and therefore making it suitable for generating shallow and intermediate water waves. The motion of the generator plate is powered by a motorized isel® toothed belt feed and controlled using the software proNC. Positioned at the tank's opposite end, a panel wave absorber, developed by [Kaufmann, 2015] and validated by [Bestier, 2016], minimizes wave reflection. The absorber consists of ten steel panels, which are oriented perpendicular to the wave direction, increasing in height towards the tank's back wall. The flow section includes a flat 1.3 m upstream section, and a 0.69 m x 0.60 m slot for a permeable artificial seabed model (SBM), representing the measurement section. The distance between the wave generator plate in its neutral position and the measurement section is 2.5 m. The bottom construction featuring this slot was developed by [Karow, 2019] to allow the installation of permeable seabed models. He termed it the 'Porous Media Application Basin'.
The wave tank was supplied with water from a 4.5 m^3 storage container. For more technical details about the flow tank, wave generator, and the basin, refer to [Karow, 2019].
In addition to the wave tank, the experimental setup study included a PIV-LIF measurement system and a tracer supply unit, as illustrated in Figure 4.2. The tracer fluid supply unit was designed to introduce a fluorescent tracer fluid into the wave tank to simulate groundwater discharge. It comprised a 5 L-tracer fluid storage tank, a submersible pump, as well as a supply tube and a small reservoir underneath the SBM. Rhodamine 6G

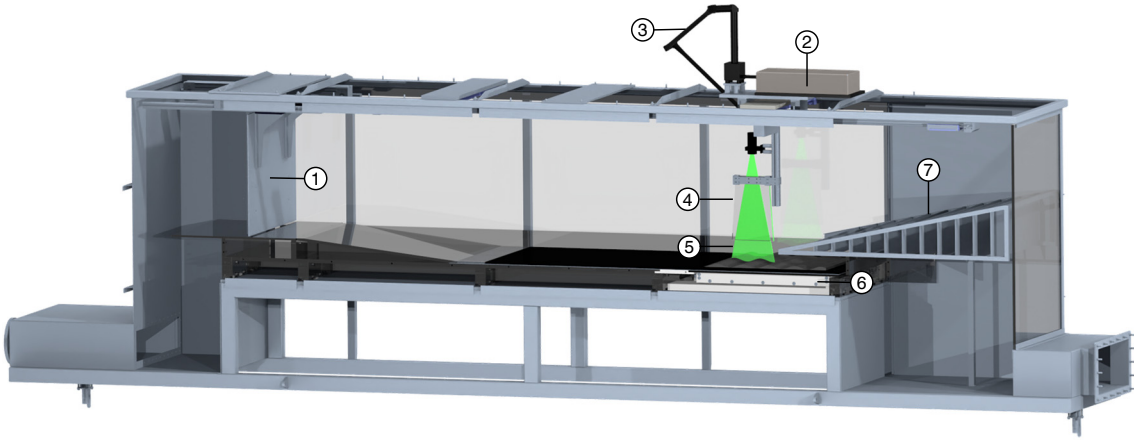

Figure 4.1: CAD model of the experimental wave tank setup: 1 - Wave generator, 2 - Laser, 3 - Light guiding arm, 4 - Light coupling, 5 - Laser light sheet, 6 - 'Porous Media Application Basin', 7 - Wave absorber; The flow section reaches from the wave generator to the wave absorber; The measurement section is defined by the laser light sheet located above the permeable seabed model.

fluorescent dye by Sigma-Aldrich® (Merck KGaA, Darmstadt, Germany) with a diffusion coefficient of 2.9 nm^2/s in water [Kievsky et al., 2008], an absorption wavelength of $525 - 530$ nm and a maximum emission wavelength of 590 nm [Yarborough, 1974] was utilized as a dye for LIF measurements. The dye powder was mixed with water to obtain a tracer fluid with the desired Rhodamine 6G concentration. This concentration varied depending on the respective measurement configuration, see Section 4.3.3. The submersible pump transported the tracer fluid into the tank, with the inflow section for the tracer fluid positioned at the bottom of the slot containing the SBM. A dispersion device, see [Karow, 2019], diffused the fluid before it entered a gap underneath the SBM, thus providing a tracer fluid reservoir to ensure steady and homogeneous perfusion of the permeable SBM. The PIV-LIF measurement system, employed for simultaneous measurements of instantaneous velocity and concentration fields, comprised two CCD cameras, a laser light source, and a control unit (computer) for measurement execution. The two Dantec FlowSense 2M cameras have a resolution of 1600 x 1200 pixels, a pixel size of 7.4 µm, and a double frame rate of 15 Hz. To ensure the reproducibility of the exact camera position, the cameras were positioned using a triaxial traverse system. The FoV of the LIF camera, which must align with the PIV camera's FoV, was adjusted using a semi-reflective mirror. The mirror's orientation can be altered via three adjusting screws.
The PIV particles, hollow 30 µm glass-spheres, and the tracer fluid were illuminated by a Litron Nd:YAG Laser with a wavelength of 532 nm. An optical light guiding arm directed the laser beam first onto a focus lens and then onto a cylindrical lens, generating the laser light sheet. This light sheet, with a thickness of approximately 2 mm, was aligned parallel to the longitudinal walls of the wave tank and directed into the water body through an acrylic Plexiglas® block (light coupling), preventing laser light reflection at the moving water surface. The light reflected by the PIV particles was filtered using a 532 nm narrow band filter, while the fluorescent light emitted by the tracer fluid passed through a 550 nm high-pass filter. Data acquisition and triggering of the cameras and laser shutter were

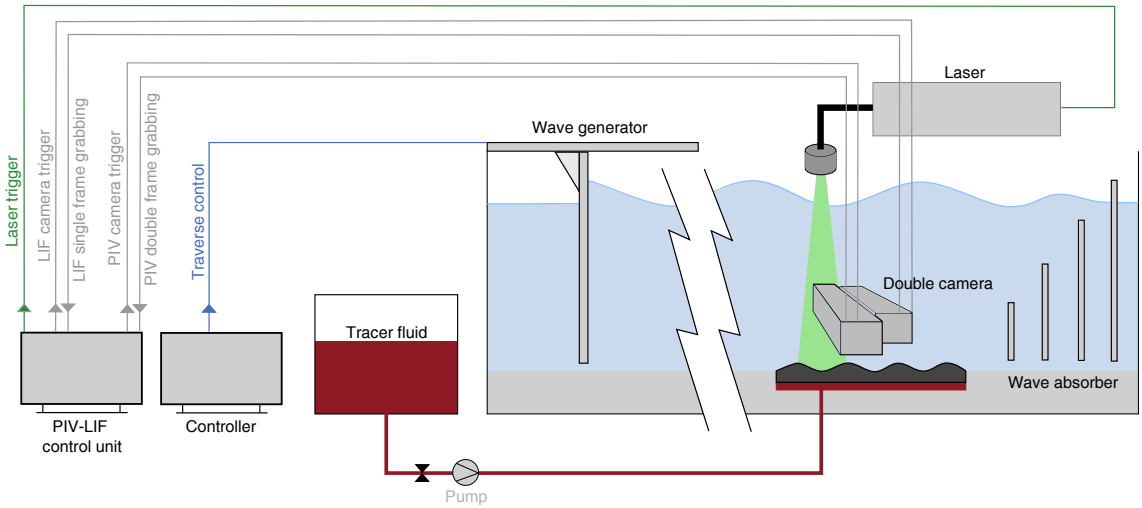

Figure 4.2: Experimental setup scheme: Wave tank (including wave absorber, flow section, and wave generator), tracer fluid supply unit (including a small reservoir inside the wave tank bottom construction, supply pipe, pump, and storage tank) and the PIV-LIF-system (including the laser, double camera, and PC control unit)

conducted using the Dantec DynamicStudio software (Dantec Dynamics A/S, Skovlunde, Denmark).

To summarise, Figure 4.3 shows a close-up scheme of the general experimental principles: The recess underneath the SBM worked as a tracer fluid reservoir and was continuously supplied from the tracer fluid storage tank. Thus, the tracer fluid could flow through the permeable SBM and enter the overlying water body at the artificial sediment-water interface. There, the oscillating flow moved the bottom boundary layer which affected the distribution of the emerging tracer fluid within the overlying water column. Moreover, Darcy and Brinkman flow were generated within the permeable material, influencing the pathways of the tracer fluid inside the SBM. During the experiment, velocity and concentration fields near the surface of the SBM were observed within a relatively small FoV, capturing at least one ripple wavelength in width. This represented a compromise between ensuring high spatial resolution of the bottom boundary layer and maintaining a sufficient overview of the topography-related flow dynamics. The metric dimensions of the FoV and the spatial resolution of the velocity and concentration measurements are further detailed in Sections 4.4 and 4.3.4, respectively.

Modification of the Wave Tank to Minimize Bottom Movement

Initial test measurements revealed that the existing bottom installations in the wave tank were susceptible to oscillation due to wave motion. Since the study aimed to analyse the bottom boundary layer within a relatively small FoV (approximately 160 mm x 90 mm), it was evident that the observed bottom movement exceeded the acceptable threshold for this purpose. Figure 4.4 illustrates the bottom movement over a single wave cycle in the initial setup, showing that the SBM surface shifted by more than one grid step

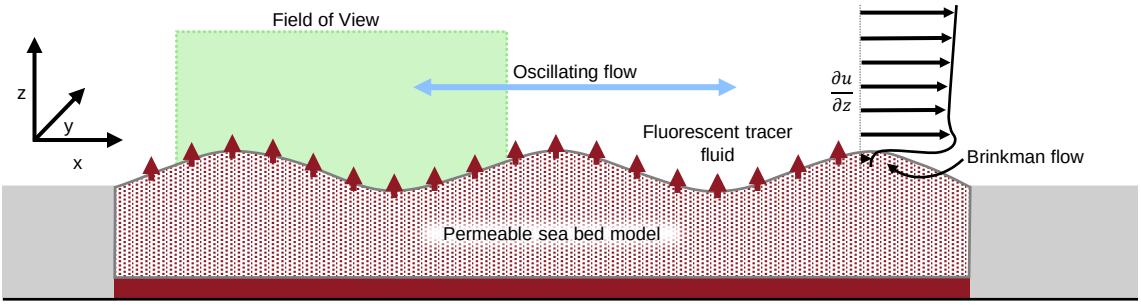

Figure 4.3: Close-up experimental scheme: Tracer fluid perfuses the permeable seabed model from underneath, reaches the artificial water-sediment interface and is mixed into the water column due to oscillating fluid motion

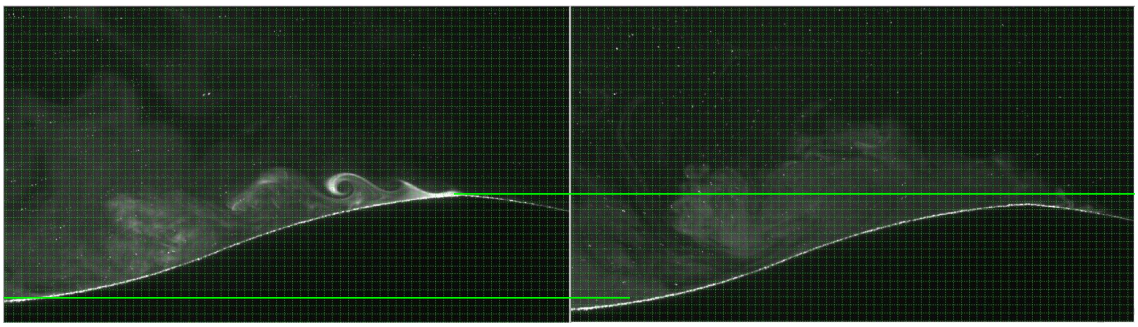

Figure 4.4: Comparison of two raw LIF snapshots at different phases of the wave cycle with a 16 x 16 pixel grid overlay: The green lines indicate height differences of more than one grid cell height of the unintentionally oscillating SBM during the wave cycle in the initial wave tank setup.

size, thereby significantly disturbing the measurements. Consequently, modifications to the existing installations were identified as necessary and implemented accordingly.
Previously, two installation components were crafted from rubber, allowing for elasticity in movement. This design was initially suitable for facilitating the bending of the tank floor to achieve a slope angle for previous measurements by [Karow, 2019]. However, since floor bending was not intended for this study, both rubber components were replaced with rigid duplicates. The first rubber component, a frame connecting the 'Porous Media Application Basin' to the rest of the bottom installation, was replaced by a duplicate made from polymethylmethacrylate (PMMA). Similarly, the second rubber component, a mat covering a significant part of the tank floor to provide a smooth surface for the flow section, was replaced by a matte black polyoxymethylen (POM) duplicate. A thin rubber mat was interposed between these two components to smooth out uneven areas of the bottom installation. These three layers were then interconnected to the 'Porous Media Application Basin' and the bottom installation via various screw connections, thereby preventing relative movement of all components, see component 1 in Figure 4.5(a).
Furthermore, the ramp positioned just behind the wave generator was modified. Previously, the slope was constructed with a loose PMMA plate resting on certain components of the bottom installation, allowing for vertical movement during wave cycles. Furthermore, this plate had sagged during previous years. To address this, the plate was replaced with a more stable and securely fixable construction. Four triangular profiles were glued to

a new PMMA plate, to prevent it from sagging. The entire assembly was tightly screwed to the bottom installation, see component 7 in Figure 4.5(b).
All of these measures were implemented to stabilize the bottom installation and firmly connect all individual components to prevent relative movements. An additional and equally important step was to secure the entire bottom installation within the tank. Since the bottom of the tank is made of glass, it was not feasible to screw the installation directly to the floor or walls. Consequently, stainless steel profiles were used to brace the bottom installation tightly against upward motion. Eight profiles were manufactured and connected to the upper tank edge using nuts and existing bolts, with washers used for vertical position adjustment to ensure a secure fit, see components 3 in Figure 4.5(a).
Finally, measures were taken to prevent horizontal movement of the bottom installation. Only one horizontal movement direction could be identified and traced back to the filling process. When the wave tank was filled at an excessively high volumetric flow rate, the whole bottom installation moved away from the inflow. To prevent displacement, two stainless steel lugs were fixed to the initial cross brace of the bottom installation. To ensure a smooth and undisturbed upstream section, any drill holes and transitions between individual components were smoothed out using moulding clay, see e.g. component 2 in 4.5(a).

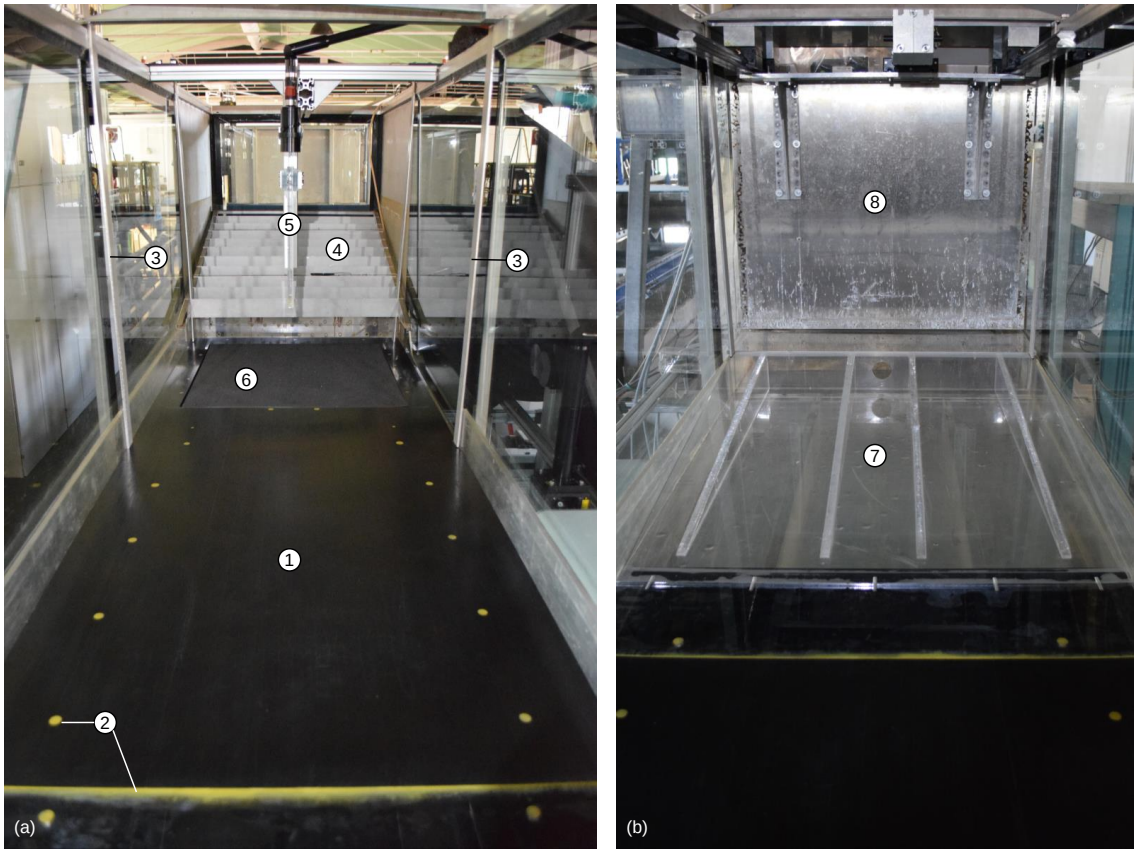

Figure 4.5: Photography of the wave tank after modification to avoid bottom movement: 1 - Rigid flow section bottom (POM), 2 - Smoothing out of transitions and drill holes, 3 - Bracing of the bottom installation against upward motion, 4 - Wave absorber, 5 - Light Coupling, 6 - seabed model (here: flat), 7 - Ramp with supportive triangular profiles, 8 - Wave generator

4.2 Boundary Conditions

The experimental boundary conditions comprise the flow conditions, the bottom topography, and the discharge of tracer fluid. The flow conditions were defined by three distinct wave scenarios. Varying bottom topography was achieved through the use of four different permeable seabed models. The tracer fluid discharge is defined by both the set volumetric flow rate and the permeability of the seabed model. The subsequent sections will offer detailed insights into these three aspects.

4.2.1 Wave Scenarios

The measurements presented in this thesis were conducted using three different wave scenarios to examine their influence on the transport processes: a calm, an intermediate, and a stormy scenario. These scenarios aim to replicate waves resembling actual intermediate water waves recorded by an acoustic wave and current profiler (AWAC) in the coastal Baltic Sea at the Baltic TRANSCOAST study site Heiligensee Hütelmoor (Coordinates: 54°13,425'N, 12°9,379'O) over a six-month period (April to October). Processed AWAC data provided surface orbital velocities, which were converted to orbital velocities one centimetre above the seabed using third-order Stokes wave theory for intermediate waves. Given that the maximum bottom orbital velocity $u_{orb,max}$ is identified as a critical factor influencing sediment transport according to [Nielsen, 1992], [Karow, 2019] chose this parameter along with the wave period T to develop wave scenarios for the wave tank experiments. Three representative orbital velocities and suitable wave periods were selected from the AWAC measurements to develop three distinct ProNC regimes, which control the piston-type wave generator's feed x_p, velocity v_p, and acceleration a_p generating respective waves. Table 4.1 specifies the characteristics of these three wave scenarios. For a comprehensive understanding of the AWAC data evaluation and the rationale behind the development of the wave scenarios, please refer to [Karow, 2019].

Table 4.1: Properties of the wave scenarios adopted from [Karow, 2019]: wave period T^*, maximum bottom orbital velocity $u^*_{orb,max}$ and water depth to wavelength ratio d/λ^*, which defines the type of all three waves as intermediate; ProNC regimes controlling the piston-type wave generator's feed x_p, velocity v_p, and acceleration a_p to produce respective wave characteristics referring to [Karow, 2019]. T corresponds to the wave period and u_{top} corresponds to the maximum horizontal far-field velocity identified during evaluation in the present study.

Wave scenario		Calm	Intermediate	Stormy
Variable	Unit			
T^*	s	1.99	2.52	3.30
T	s	1.99	2.52	3.28
$u^*_{orb,max}$	m/s	0.05	0.10	0.25
u_{top}	m/s	0.06	0.22	0.26
d/λ^*		0.09	0.05	0.07
x_p	m	0.10	0.13	0.35
v_p	m/s	0.20	0.15	0.40
a_p	m/s^2	0.50	0.50	0.60

4.2.2 Seabed Models

To realize rippled bottom topographies for the experiments, four different permeable seabed models were developed and crafted from open-cell polyurethane (PU) foam.
For pilot tests and measurements, a preliminary foam model has been constructed and manufactured using a simple sinus-shaped profile. The wavelength and amplitude of the profile lie within a range roughly measured in the field by [Schade, 2019]: Ripple height $h_R = 1.96\ \text{cm} \pm 0.24\ \text{cm}$ and ripple wavelength $\lambda_R = 14.7\ \text{cm} \pm 2.6\ \text{cm}$. The profile was sketched and extruded to a 3D model using the computer-aided design (CAD) software Creo® Parametric (PTC Inc., Boston, Massachusetts, USA). The preliminary model had a ripple height of 18.8 mm and a ripple wavelength of 147 mm. First, results for concentration and velocity measurements as well as fields of turbulent kinetic energy were presented in [Kandler et al., 2021].
For the main measurement campaign, four different seabed models were developed to investigate the influence of specific topographical characteristics on turbulent transport behaviour. The first seabed model serves as a reference and is a generic flat seabed model (FLAT). The second model, like the preliminary model, has a generic sinusoidal contour but has been adjusted in terms of ripple wavelength and height to agree with the third and fourth model: the generic sinusoidal rippled seabed model (SIN). The third model is intended to mimic a more natural ripple shape with a smaller radius at the crest than in the trough and was developed based on in situ data: the symmetric naturally rippled seabed model (NAT). The fourth model is aimed at investigating the influence of ripple asymmetry and corresponds to a modified form of the third (naturally shaped) model: the asymmetric naturally rippled seabed model (ASYM).
The last two mentioned models were developed based on in-situ data collected on October 7, 2019, from four distinct locations at the coastal study site of the Baltic TRANSCOAST project (nature reserve Heiligensee Hütelmoor) as illustrated in Figure 4.6(a). Microtopography measurements were conducted using a ULS-200 blue (750 nm wavelength) laser line scanner (2G Robotics, Waterloo, Ontario, Canada) as in [Schönke et al., 2017]. The scanner was mounted to a frame constructed from aluminium profiles, as depicted in Figure 4.6(b), and deployed to the sea floor from aboard the boat 'Klaashahn' of the Leibniz Institute for Baltic Sea Research, in German: Leibniz-Institut für Ostseeforschung Warnemünde (IOW).
In Table 4.2, the four measurement sites, denoted hereafter as Station 1 to 4, are presented alongside their respective geographic coordinates and water depths. Furthermore, it is detailed which specific marine sampling points of the Baltic TRANSCOAST project were approached for the topographic measurements.

Initially, the acquired laser scans underwent preprocessing by M. Schönke, following the procedures outlined in [Schönke et al., 2017]. The resulting 3D data is depicted in Figure 4.7, showcasing three sites characterized by clearly discernible sand ripples, alongside one stony site where ripple identification was not feasible.

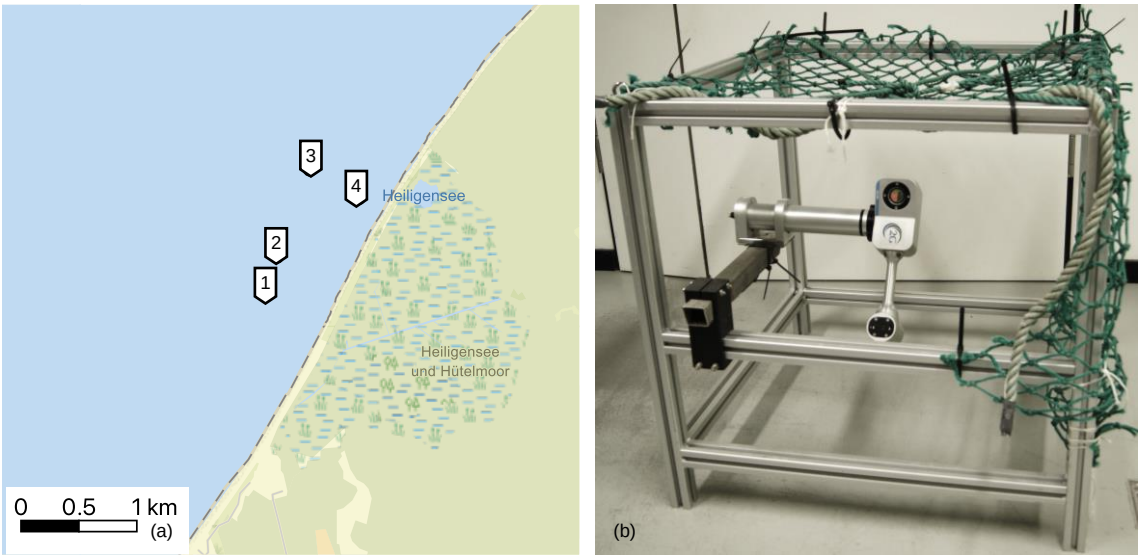

Figure 4.6: (a) Geographic location of the sampling points for recording the microtopography data at the marine site of the nature reserve Heiligensee Hütelmoor (map based on ESRI OSM Street, QGIS Version 3.34.11 Prizren, provided by A.-K. Jenner, Baltic TRANSCOAST) (b) Frame construction made of aluminium profiles with the mounted ULS-200 laser scanner

Table 4.2: Geographic coordinates and water depths of the sampling points approached for microtopography measurements, conducted on October 7, 2019, at the coastal study site of the Baltic TRANSCOAST project (nature reserve Heiligensee Hütelmoor)

Station	Sampling Point	Latitude	Longitude	Water depth
1	Near BTC 18	54°12,974'N	12°09,210'E	5.3 m
2	BTC 23	54°13,153'N	12°09,294'E	5.1 m
3	BTC 32	54°13,557'N	12°09,556'E	6.0 m
4	BTC 34	54°13,425'N	12°09,943'E	5.4 m

Subsequently, the topographical data underwent processing by the student [Meissner, 2020] (supervised by the author) using MATLAB (The MathWorks, Inc., Natick, Massachusetts, USA) to identify ripples and extract ripple profiles. To achieve this, outliers were identified, removed, and replaced through interpolation, as demonstrated in Figure 4.8. Afterwards, the elevation data underwent smoothing via a Gaussian filter. Isohypses (elevation lines) were then generated to pinpoint the crests and troughs of the ripples. At locations of minimal gradients along the isohypse contours, supporting points for curves defining ripple crests and troughs - termed hereafter as crest and trough lines - were positioned, as depicted in Figure 4.9.

To extract cross-sectional ripple profiles, equidistant orthogonal lines were generated along the crest and trough lines. This resulted in ten pairs of crest and trough lines (ST1 R1-2, ST2 R1-4, and ST3 R1-4, refer to Figure 4.9), which were utilized to generate a total of 753 cross-sectional ripple profiles. The local maxima of these profiles corresponding to the ripple crests and the local minima corresponding to the ripple troughs, provided the coordinates for both features. Only complete profiles, including either two ripple crests and one trough or one trough and two crests, were treated as valid data. [Meissner, 2020].

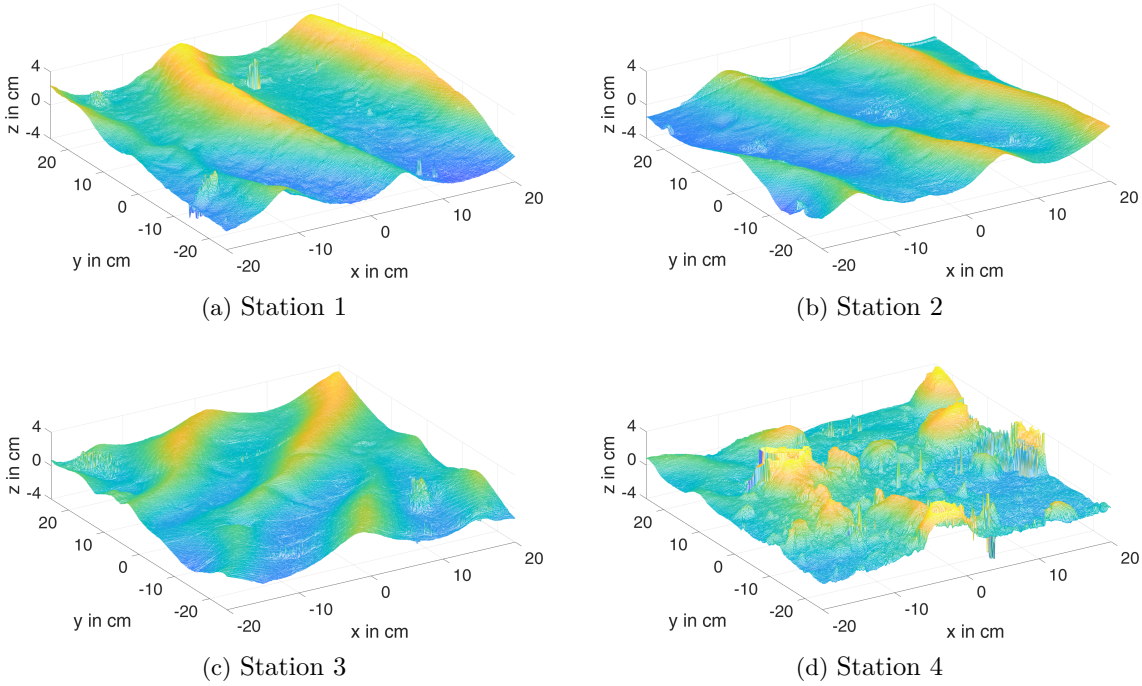

(a) Station 1

(b) Station 2

(c) Station 3

(d) Station 4

Figure 4.7: Preprocessed topographical laser scans from four coastal sites of the Baltic TRANSCOAST project (nature reserve Heiligensee Hütelmoor; (a), (b), (c) showing sand ripple marks, (d) showing a stony sea floor

Finally, the resulting cross-sectional ripple profiles delivered from [Meissner, 2020], each comprising 199 2D data points, were treated as individual measurements of ripple height and wavelength. Figure 4.10 clearly illustrates the correlation of ripple height and wavelength for each of the ten cross-sectional ripple profiles. As the purpose of the field measurement was to develop one representative naturally shaped seabed model, the identified ripple profiles were averaged, with outliers falling outside the 95% confidence interval excluded. This averaging process involved calculating the median of each coordinate point from the remaining 705 2x199 arrays defining the cross-sectional ripple profiles within the 95% confidence interval. In other words, these ripple profiles were overlaid and averaged. Hence, a singular 2x199 array was computed defining a representative cross-sectional ripple profile based on the field data, featuring a ripple height of 19.64 mm and a ripple wavelength of 159.22 mm.

To transfer this profile to Creo® Parametric for constructing a 3D model, it underwent fitting using a third-order spline fit. Since [Meissner, 2020] demonstrated, that 13 equidistant points sufficed for accurately replicating the spline, this number of coordinates was extracted from the curve and multiplied to match the geometric requirements of the seabed model. The resulting data set was exported from MATLAB as a .pts file and imported in Creo® Parametric as point coordinates. The *Sketch* tool was then used to recreate the spline, ensuring tangential continuity, and to draw the cross-section of the seabed model, which was finally extruded to a 3D model and exported as a .dxf file for manufacturing.

To create the asymmetric model, the coordinate points of the symmetric model were shifted in MATLAB. Therefore, the supporting points of the splines were compressed on the stoss side and dilated on the lee side of the cross-sectional ripple profile, resulting in a RSI of

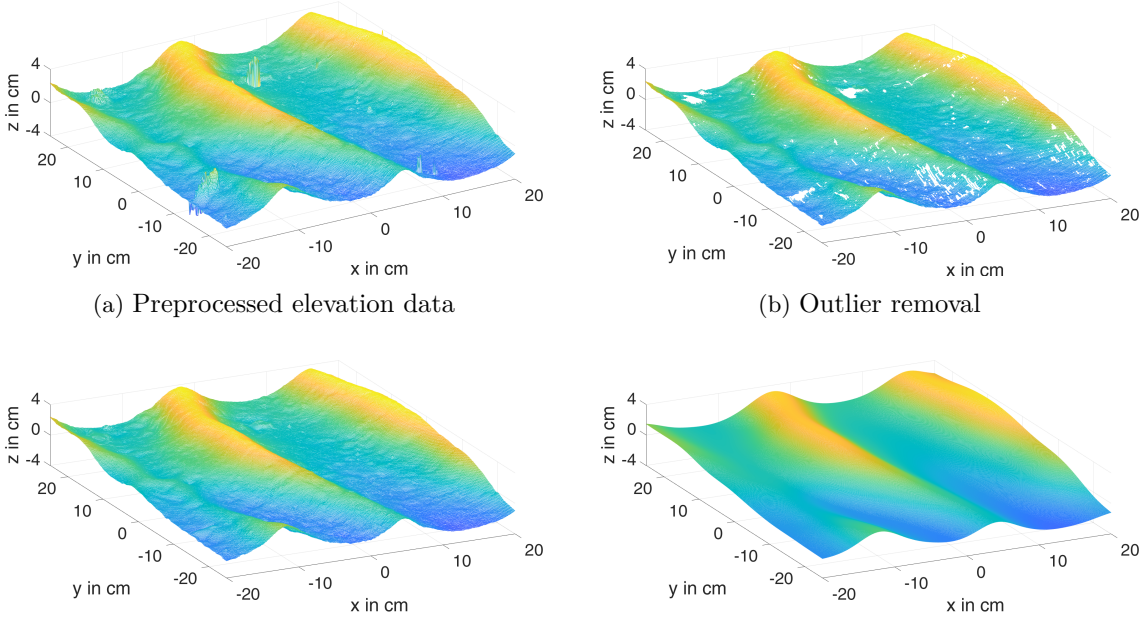

(a) Preprocessed elevation data

(b) Outlier removal

(c) Interpolated elevation data

(d) Smoothed elevation data

Figure 4.8: Processing of the topographical data at the example of Station 1: The preprocessed elevation data (a) was firstly cleansed of outliers (b) and subsequently reconstructed by interpolation (c) and smoothed with a Gaussian filter.

$RSI = \alpha/\beta = 3$. This index exceeds the range of asymmetry indices measured in the topographical scans, where a maximum RSI of approximately 2 was identified. However, this extreme value was selected to ensure that the effects of asymmetry would be clearly visible in the PIV-LIF-data.

As already mentioned, the sinusoidal rippled seabed model was then adapted to agree with the naturally shaped symmetric and asymmetric model in regards to ripple wavelength and height, as detailed in Table 4.3.

The flat (reference) seabed model corresponds to a simple cuboid measuring 690 mm in length, 600 mm in width, and 50 mm in depth, which are the same base dimensions of the other models. Figure 4.11 depicts the CAD models of all four seabed models.

Table 4.3: Geometric characteristics of the artificial seabed models with ripple steepness h_R/λ_R, ripple symmetry index $RSI = \alpha/\beta$, the relation of crest radius r_C to trough radius r_T, ripple stoss side s_{stoss}, and ripple lee slope s_{lee}

SBM	Shape	λ_R	h_R	h_R/λ_R	α/β	r_C/r_T	s_{stoss}	s_{lee}
		mm	mm				(°)	(°)
Preliminary	sinusoidal	147.00	18.80	0.13	1	1		
FLAT	-	-	-	-	-	-	-	-
SIN	sinusoidal	159.22	19.64	0.12	1	1	13.86	13.86
NAT	natural	159.22	19.64	0.12	1	<1	13.86	13.86
ASYM	natural	159.22	19.64	0.12	3	-	9.34	26.26

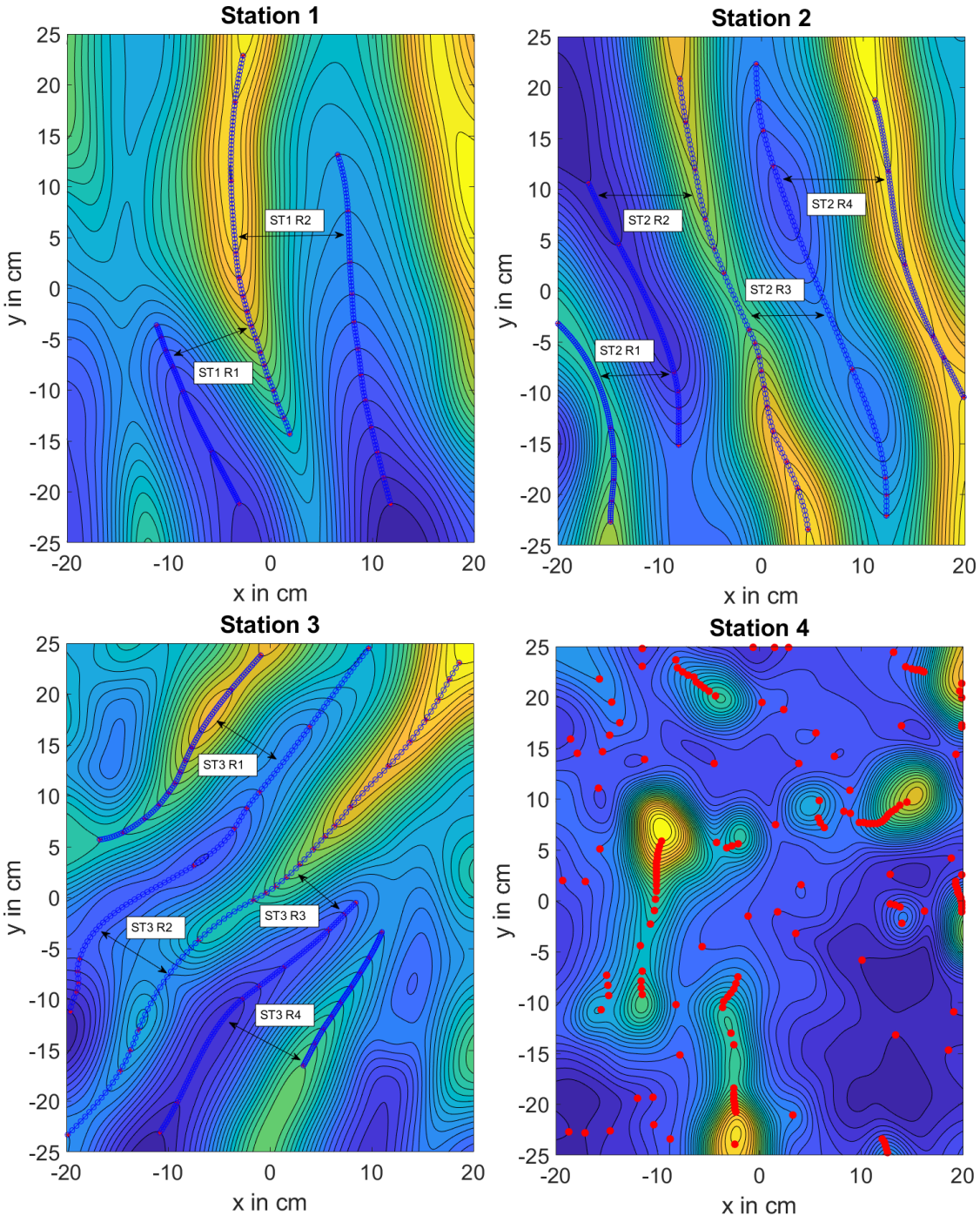

Figure 4.9: Detected crest and trough line pairs at Station 1 to 3 providing cross-sectional ripple profiles for statistical analysis and CAD model generation

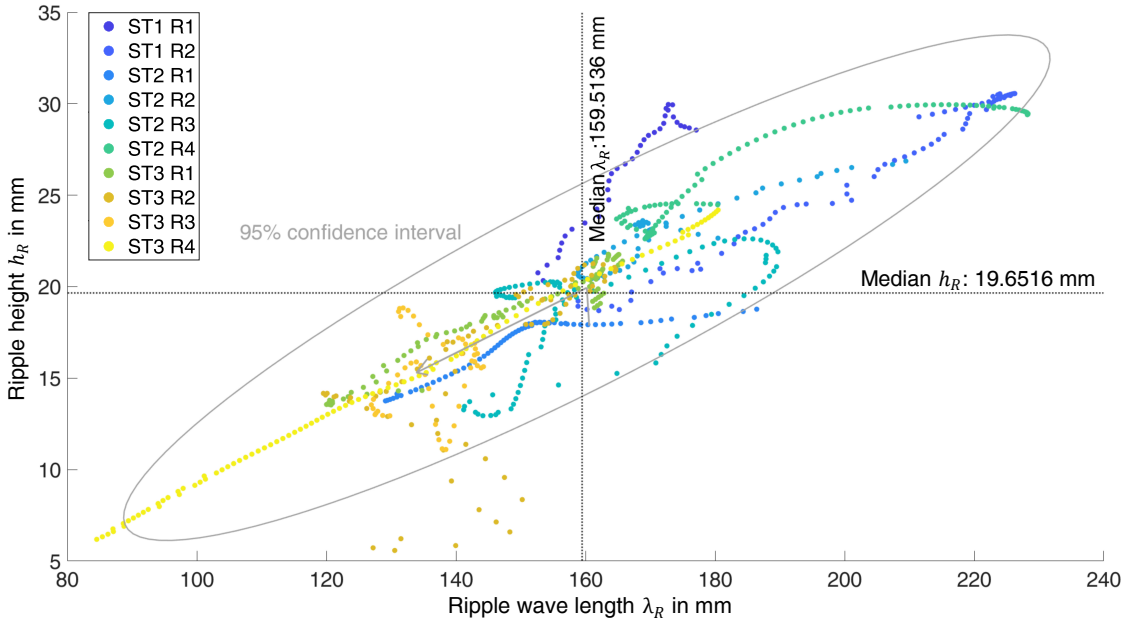

Figure 4.10: Ripple height h_R versus ripple wavelength λ_R of ten identified ripple pairs at Station (ST) 1 to 3 with up to four ripple pairs (R); Cross-sectional ripple profiles lying within the 95%-confidence interval were averaged to obtain one representative ripple shape

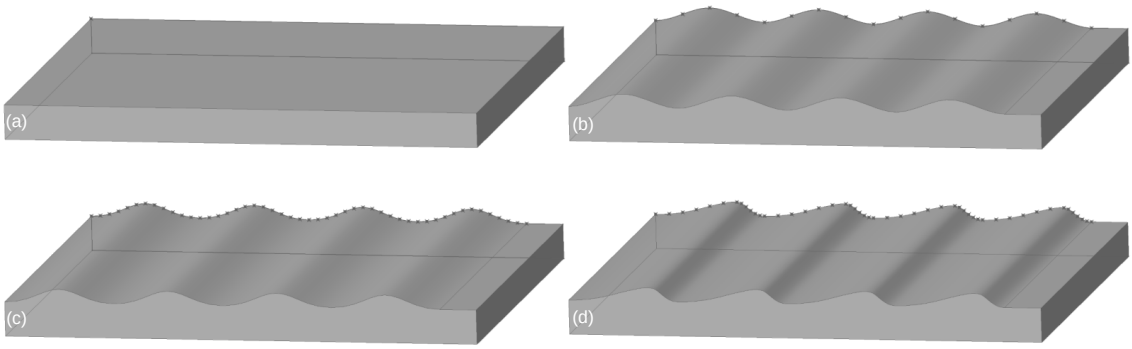

Figure 4.11: CAD models of the artificial seabed models used for the main sampling campaign; (a) FLAT: Generic flat seabed model; (b) SIN: Generic sinusoidal rippled seabed model; (c) NAT: symmetric naturally rippled seabed model; (d) ASYM: Asymmetric naturally rippled seabed model; Base dimensions: 690 mm x 600 mm x 50 mm; Ripple height $h_R = 19.64$ mm; Ripple wavelength $\lambda_R = 159.22$ mm

All artificial seabed models were manufactured based on the CAD-constructed .dxf files using a specialized CNC-cutting process, shaping open-cell PU foam into the various ripple-shaped profiles. This CNC-cutting procedure was conducted by the company Schaumstoffe Wegerich GmbH within a fabrication tolerance of ± 1 to 5 mm [Schaumstoffe Wegerich GmbH, 2021]. The chosen material, PU RG 26/35F, has an anthracite, almost black, colour to minimize laser light reflection. It features a bulk density of 26 kg/m^3 and a Shore hardness of 3.5 kPa [Schaumstoffe Wegerich GmbH, 2021].
Given that the material of the models is buoyant, their installation within the bottom construction of the wave tank required special consideration. PMMA plates, 8 mm in thickness, were perforated using a laser cutter to ensure permeability and provide a rectifier function. These plates served as mounting platforms: the foam models were affixed to the plates using UHU® spray glue. To establish a lasting adhesive bond, both surfaces were initially coated with glue, allowed to dry for approximately ten minutes, and then firmly pressed together with significant force. To prevent contamination and blockage of pores, which were crucial to maintaining permeability for tracer perfusion, the foam surface was selectively covered with glue within the appropriate areas by pressing the perforated, glue-coated plate onto the foam, effectively utilizing it as a glue stamp. Consequently, the foam and plate were only bonded within the designated regions. In addition, the perforated plate area was bordered with sealing tape to prevent lateral leakage of the tracer fluid, as visible in Figure 4.12(a). The complete foam models, which are depicted in Figure 4.12(b) to (e), could then be secured to the bottom construction of the wave tank, atop a 2 mm PMMA frame, ensuring distance from the tracer fluid inflow.
Figure 4.13 summarizes the process of model construction for the in-situ-based based models.

4.2.3 Discharge

In addition to the flow and bottom topography conditions, the quantity and quality of the tracer fluid discharge mimicking ground or pore water flow is another primary boundary condition. This boundary condition was intended to be as equal as possible for all experiments of the main sampling campaign. The volumetric flow rate from the tracer fluid storage tank was kept constant across all experiments. During the experiments, the differences in temperature, and thus density, between the tracer fluid and the water in the wave tank were kept to a minimum. The dispersion device designed by [Karow, 2019] was used to achieve even perfusion of the permeable seabed model. However, the thickness of the seabed models varies due to the wavy surfaces, resulting in a thickness of 50 mm in the ripple troughs and a thickness of 69.64 mm in the ripple crests. The same type of material was used for every seabed model, yet, slight deviations in the structure of the open-cell foam and therefore its hydraulic conductivity are likely. In contrast to [Karow, 2019], who conducted constant-head permeability measurements, the permeability of the PU foam used for the seabed models was quantified by a falling-head permeability measurement in this study.

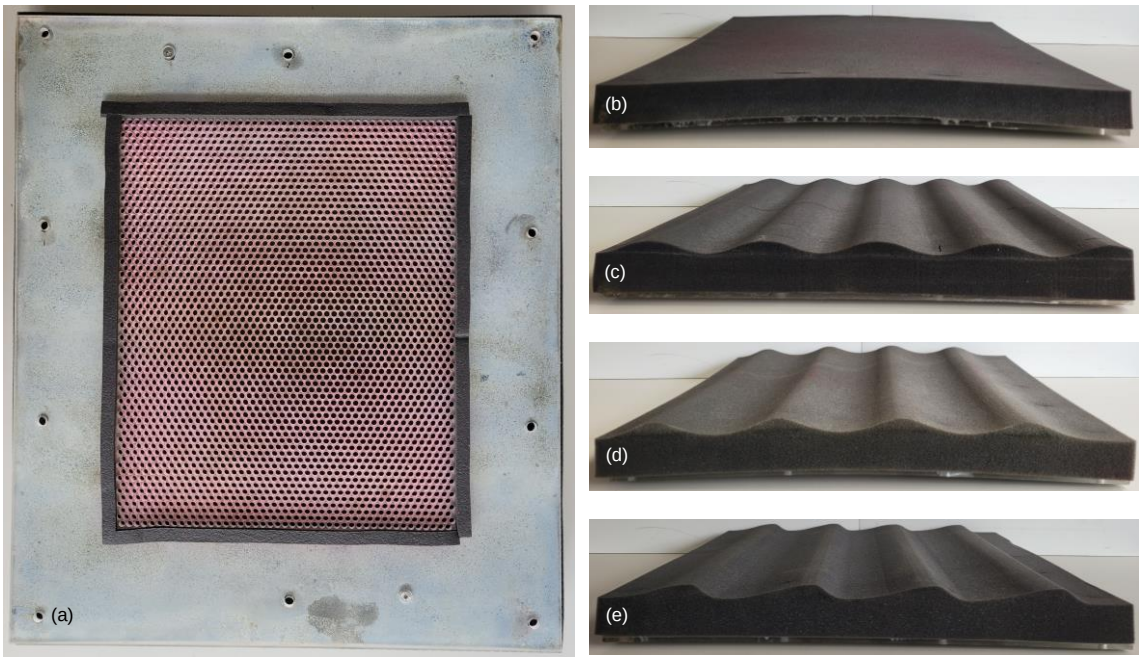

Figure 4.12: (a) Perforated and sealed PMMA plate adhered to the foam model to enable mounting in the wave tank and (b) flat (c) sinusoidal rippled (d) symmetric naturally rippled and (e) asymmetric naturally rippled foam model prepared for montage

To determine the PU foam's permeability K, cylindrical probes with a known length L were saturated with water and placed at the bottom of a 0.5 m long transparent PMMA cylinder. A bed of very permeable gravel was positioned underneath the probe to prevent it from being displaced. The PMMA cylinder was filled up with water and closed with a rubber stopper to hold the water level. Then, the stopper was opened to allow the lowering of the water level. At each $\Delta t = 5$ s time interval, the initial and final water levels h_1 and h_2 were marked on the cylinder and later on, measured. For statistical reasons, this procedure was repeated ten times, resulting in $n = 55$ measurements. From these measurements, an average hydraulic conductivity k_f was calculated based on Equation 4.1. The resulting $k_{f,mean} = 0.59$ cm/s had a standard deviation of $sd = 0.14$ cm/s. The permeability $K = 5.80 \cdot 10^{-10}$ m^2 was then calculated following Equation 4.2.

$$k_f = \frac{L \cdot \ln \frac{h_1}{h_2}}{\Delta t} \tag{4.1}$$

$$K = \frac{k_f \cdot \eta}{g \cdot \rho} \tag{4.2}$$

[Schade, 2019] measured permeability values in the upper 10 cm of the sediment at the marine Baltic TRANSCOAST Hütelmoor study site, which ranged from $K = 0.01 \cdot 10^{-10}$ m^2 to $K = 1.13 \cdot 10^{-10}$ m^2. Thus, the PU foam used to model the seabeds in this study is by a factor $\approx 5 - 500$ more permeable than the original sand in the field, but still within the range of 10^{-12} m^2 to 10^{-9} m^2 for sand given by [Bear, 1988], see Section 2.2.

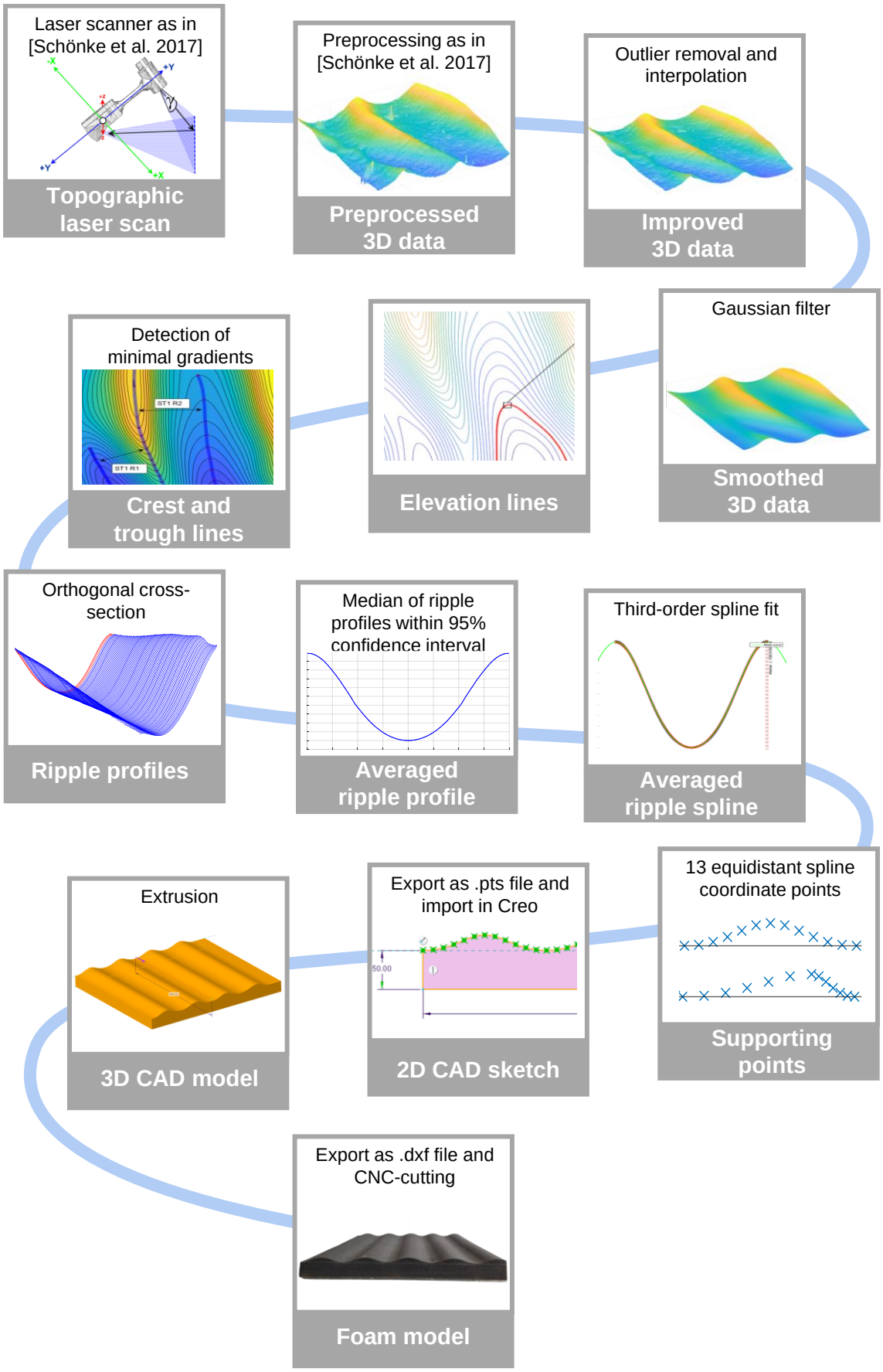

Figure 4.13: Process of seabed model development based on in-situ laser scan topography data

The volumetric flow rate of $Q = 0.96\,\mathrm{L/min} = 1.6 \cdot 10^{-5}\,\mathrm{m^3/s}$ set in the PIV-LIF-experiments equals a seepage rate of $3.9 \cdot 10^{-5}$ m/s related to a projected discharge area of 0.41 $\mathrm{m^2}$ (0.69 m x 0.60 m).
This value approaches the highest values documented in the literature according to [Rosenberry and Morin, 2004], however, a significant variability in SGD-induced seepage rates has been generally observed, which can be attributed to the numerous differences in measurement sites as well as the challenges associated with accurately measuring this parameter [Smith et al., 2009]. For the study site Hütelmoor, [Racasa et al., 2021] numerically modelled SGD and calculated maximum seepage rates of 1.05 cm/d = $1.22 \cdot 10^{-7}$ m/s for terrestrial SGD. Yet, similar volumetric flow rates in the wave tank experiments did not yield a well-measurable signal for c over the measurement duration of about 10 minutes - which proved to represent a good compromise between the convergence behaviour of the measured variables and the amount of data. Therefore, a flow rate at the upper limit of literature values was chosen for the experiments to achieve an adequate signal-to-noise ratio. In doing so, it was also considered that the tracer fluid can still be classified as a passive scalar, implying that no impact on overall flow dynamics and no interaction with other transport processes occur, as the velocities induced by the discharging tracer are negligible compared to the velocities in the water column [Combest et al., 2011].
Throughout the entire experiment, the volumetric flow accumulated to an absolute volume of circa 20 L, which corresponded to approximately 0.75% of the total water volume in the wave tank.

4.3 PIV-LIF-Measurements

The following section provides a comprehensive overview of the procedures employed for the PIV-LIF measurements. This includes the calibration processes for PIV and LIF, along with a description of the experimental protocol for individual measurements. Additionally, it details the methodology for image processing and computation of 2D time-resolved velocity and concentration fields. All these steps were carried out using the Dantec DynamicStudio 7 software.

4.3.1 PIV Calibration

The calibration process for PIV measurements aims to determine a scale factor that converts pixel units into metric units. To achieve this, a 200 mm x 200 mm dot-type target is positioned within the FoV and aligned with the laser light sheet. It consists of a white plate equipped with a defined uniform black hole pattern. An image of this target is then employed to designate a specific distance corresponding to a known metric length. Subsequently, the Dantec DynamicStudio software computes the corresponding scale factor, facilitating the scaling of measured particle displacements. For the main measurement campaign, the determined scale factor was 14.3. Multiplied with the camera pixel size of 0.0074 mm per pixel this gives a relation of 0.1058 mm/pixel.
Additionally, in this step, the position of the coordinate origin is set at the bottom left of the FoV. The camera position stayed fixed during the measurement campaign, and therefore, the coordinate origin remained consistent for all presented measurements. In the subsequent analysis, the horizontal coordinate corresponds to x, and the vertical coordinate corresponds to z.

4.3.2 LIF Calibration

The objective of the LIF calibration is to define the relation between computational pixel brightness and actual dye concentration at specific points within the FoV. To accomplish this, a calibration curve is derived by incrementally increasing the dye concentration, here Rhodamine 6G, within the wave tank and capturing images after each step. For the described experimental setup and the subsequent main measurements, a LIF calibration was conducted in six steps, covering dye concentrations ranging from $0 - 40$ µg/L. Consequently, the calibration curves comprise a maximum of six sampling points. It's noteworthy that at 50 µg/L, most of the image was overexposed. Therefore, 40 µg/L was the maximum value for calibration.
An inherent challenge arises due to the fact that the Dantec DynamicStudio software generates only linear calibration curves. However, the assumption of a linear relationship between dye concentration and pixel brightness is only valid for low concentrations of Rhodamine 6G, specifically up 0.02 mg/L [Gaskin, 1995]. Above this value, saturation effects can be observed.
Another complication stems from the varying brightness of the laser light sheet: the centre of the light sheet tends to be brighter than the periphery. This inconsistency may result

in overexposure in the centre and underexposure at the periphery, leading to potential loss of information.
To address this, multiple calibration curves were generated during the LIF calibration process: $C1$: $0 - 20$ µg/L (three data points), $C2$: $0 - 30$ µg/L (four data points), $C3$: $0 - 35$ µg/L (five data points), and $C4$: $0 - 40$ µg/L (six data points). Thus, the most suitable curve could be employed for each pixel within the FoV during LIF evaluation, thereby extending the range of measurable dye concentrations. The precise procedure will be further explained in the Sections 4.3.4 and 4.4.

4.3.3 Experimental Procedure

To ensure optimal comparability, each experiment within the main measurement campaign was conducted following a fixed experimental procedure. Initially, the storage tank underwent a thorough cleaning and was filled with tap water. During the filling stage, the wave tank was prepared for the experiment: the glass walls within the PIV and LIF camera's FoV were cleaned using a standard window cleaner and paper towels. The respective SBM was securely mounted within the wave tank's bottom construction, with careful attention paid to smoothing out the transition between the upstream section and the SBM using black, waterproof adhesive tape.
Following this, the wave tank was filled to a static water level of 0.3 m from the storage tank. Throughout the filling process, efforts were made to eliminate entrapped air from the SBM by gently pressing the foam with a perforated tamper-like tool. Subsequently, the water in the wave tank was mixed with a manually stirred suspension of 30 µm glass particles and water to facilitate PIV measurements. The dosage of glass particles was determined based on experience and fine-tuned iteratively during the preparation of the experiment.
Subsequent to this, any air bubbles were removed from the PMMA light coupling to prevent interference with the laser light sheet due to shadow casting. Once these preparatory tasks were completed, the wave generator was activated. A settling time of 20 minutes allowed the oscillatory flow to fully stabilize and the PIV particles to evenly distribute within the wave tank. During this period, preliminary measurements were conducted to warm up the laser and assess and eventually adjust the seeding particle density.
To minimize disturbance from extraneous light sources, the wave tank was covered with black cloth, and all other sources of light in the laboratory were extinguished during the measurements.
Upon completion of the settling time, the inflow of the tracer fluid was initiated. Following the recommendations of [Kandler, 2018], PIV-LIF recordings were started 10 minutes later, allowing time for the tracer to disperse within the SBM and for the formation of a concentration boundary layer. Additionally, the measurements were stopped before this layer dissipated at the end of the experiment. This approach was implemented to avoid inaccuracies in phase-averaged data caused by start-up and end effects of the discharge process.

The PIV-LIF measurements were conducted using DantecDynamic Studio with a trigger rate of 15 Hz and an inter-pulse interval of 15000 µs for the calm, 5000 µs for the intermediate, and 4000 µs for the stormy wave scenario. These intervals proved suitable for capturing the expected velocity range that resulted from the respective wave scenario. The aperture setting of the PIV camera was set to 5.6, while that of the LIF camera was set to 2.8. Each measurement session involved capturing a series of 10,100 PIV double-frame images and simultaneously 10,100 LIF single-frame images. The initial 100 images were discarded to allow the laser light sheet to reach full brightness. Consequently, for each measurement configuration, 10,000 PIV and LIF images capturing a time span of 11 minutes and 6.67 seconds were saved for processing.
To prevent pixel overexposure during the measurements and to maximize information capture, measurements were conducted with different dye concentrations of the tracer fluid. The concentrations were varied based on the dilution rate of the respective measurement configuration, which was influenced by the wave scenario and the seabed model. For configurations with a high dilution rate, a high dye concentration of the tracer fluid was used for the experiment. It is crucial to maintain an appropriate dye concentration: concentrations that are too high can lead to pixel overexposure, resulting in loss of detail in regions of high concentration values, while concentrations that are too low may not provide sufficient signal strength to accurately capture flow dynamics.
To achieve comparability, the measured concentration values were later on normalised with the respective dye concentration of the injected tracer fluid $c_{\mathrm{R6G,\ Tracer}}$, see Section 4.4. Table 4.4 lists $c_{\mathrm{R6G,\ Tracer}}$ for all experiments of the main measurement campaign.
Subsequent to each experiment, the SBM was flushed with a minimum of 15 L of pure tab water, to reduce the impact on the following experiments due to dye residues. After draining the water, the wave tank was thoroughly flushed using a common garden hose. Additionally, the light coupling as well as the windows of the tank, through which the cameras capture the images, were dried to ensure good optical access for the next measurement. The water drained from the wave tank is first filtered to remove the seeding particles using a particle filter and then treated with an activated carbon filter to remove the fluorescent dye before being discharged into the wastewater system.
Table A.1, to be found in the appendix, documents the measurement protocols for all measurement configurations.

4.3.4 Image Processing and Computing of Time-resolved Velocity and Concentration Fields in Dantec DynamicStudio

The processing of the captured images is depicted in Figure 4.14. The quality of the raw PIV images, see Figure 4.14 (a), was first improved by subtracting an overall mean image from all frames using the functions *Image Mean* and *Image Arithmetic*, see Figure 4.14 (b). Thus, the effect of lasting spots and scratches on the wave tank's glass walls, as well as the laser light reflection at the seabed surface could be reduced. Secondly, the *Image Balance* tool of the software was used to compensate for the uneven light distribution of the laser light sheet, see Figure 4.14 (c). The PIV correlation used to calculate velocity vector fields

Table 4.4: List of Rhodamine 6G dye concentration of the injected tracer fluid $c_{\text{R6G, Tracer}}$ used for the respective experiments of the main measurement campaign. This value is later used for normalisation to achieve comparability between the distinct measurement configurations.

Date	SBM	Wave Scenario	$c_{\text{R6G, Tracer}}$ in µg/L
29/06/2021	NAT	stormy	200
30/06/2021	NAT	intermediate	200
01/07/2021	NAT	calm	200
04/07/2021	ASYM	stormy	600
05/07/2021	ASYM	intermediate	600
07/07/2021	ASYM	calm	600
10/07/2021	FLAT	stormy	1200
11/07/2021	FLAT	intermediate	1200
15/07/2021	FLAT	calm	200
19/07/2021	SIN	stormy	200
20/07/2021	SIN	intermediate	200
21/07/2021	SIN	calm	200

for each frame was done using the *Adaptive PIV* tool, see Figure 4.14 (d). This method can automatically select the optimal size for each individual IA, within the bounds of specified minimum and maximum IA sizes. The initial iteration employs the largest permissible IA size, while subsequent iterations may reduce IA sizes in areas with sufficiently high particle density. The chosen grid step size was 16 x 16 pixels equivalent to 1.69 x 1.69 mm. The minimum interrogation area (IA) size was 32 x 32 pixels and the maximum was 64 x 64 pixels. Consequently, the minimum overlap was 50% and the maximum overlap was 75%. The outlier detection included a neighbourhood of 3 x 3 vectors and the defined *Peak to height ratio* for validation was 1.5. In addition, the included *Wall Windowing* tool was used to reduce wall bias at the water seabed interface. Since there are typically no particles within walls, when an IA extends into a wall, the resulting average displacements -and therefore velocities - may be biased by faster-moving particles far from the rigid boundary. The *Wall Windowing* tool mitigates this by additionally masking these distant particles, ensuring the remaining particles are symmetrically distributed around the IA centre [Dantec Dynamics A/S, 2021].

The raw LIF images, see Figure 4.14 (e), were masked to exclude the seabed using the same mask, that was selected for the *Wall Windowing* during PIV correlation, see Figure 4.14 (f). The *LIF-Processing* tool was used to correlate the pixel brightness to actual tracer fluid concentration values, see Figure 4.14 (g). This procedure was performed for each of the four LIF calibration curves. The higher the maximum value of the calibration curve, the less precise the curve is within the range of low concentration values. Thus, the LIF images were firstly processed with the shortest calibration curve ($0 - 20$ µg/L) to prevent information loss in the darker regions of the images. If, in the brighter regions of the image, this was leading to concentration values equalling the maximum concentration value of the respective calibration curve, the LIF-processing was also performed using the calibration curve with the next higher concentration maximum ($0 - 30$ µg/L). This procedure was repeated until no regions in the processed images were left, where the

concentration reached the maximum value of the respective calibration curve. Thus, a maximum of four sets of LIF images were generated for every experiment resulting in 4 x 10,000 processed LIF images. The further approach will be explained in the Section 4.4. All *LIF-processing* results were resampled using the grid defined by the velocity vector fields, see Figure 4.14 (h). This means, that the concentration values of all pixels covered by the same grid cell (corresponding to a PIV IA) were averaged. Hence, every velocity vector can be assigned to one certain concentration value for the following correlation. Both, PIV- and LIF-data were exported as .csv-files for further evaluation.

4.4 Data Processing with Python

The acquired time-resolved PIV- and LIF-datasets underwent further processing, analysis, and visualization using self-developed custom Python codes (Python Software Foundation, Wilmington, Delaware, USA) to generate phase-resolved maps and time-averaged profiles of concentration, in-plane turbulent kinetic energy, and vertical turbulent transport. This was done partly within the PyCharm integrated development environment (JetBrains, Prague, Czech Republic) and partly within the web-based interactive development environment JupyterLab (Project Jupyter, Berkeley, CA, USA).
The first step was to read and re-sort the .csv files to obtain three-dimensional arrays of the horizontal velocity u, the vertical velocity w, and the concentration c corresponding to the calculated vector fields for each of the $10,000$ time steps. In the case of the concentration, this was done for each of the up to four data sets of concentration values from the different *LIF-processing* procedures, see Section 4.3.4, resulting in 4 x 10,000 data arrays (c_1, c_2, c_3, and c_4). In this study, the vector fields and therefore the data arrays had a shape of 99 x 55 vectors, including the masked regions, but treating them as not a number (NaN) entries. The original metric dimensions of the FoV were 167.57 mm x 93.28 mm. It is noteworthy that the FoV was trimmed to a width of $\lambda_R = 159.22$ mm during the analysis to accurately represent a single ripple wavelength in the horizontally averaged results.
As a second step, the 4 x 10,000 c data arrays underwent a correction program (written by H. Stirnweiß). In DynamicStudio, when masking is applied, the masked region is set to a brightness value of 0. Subsequently, during the resampling process, this results in a downward distortion of the mean concentration within those grid cells, which include masked regions. Therefore, the program corrects the respective concentration values. The PIV grid, consisting of 99 x 55 cells, is overlaid onto the mask of dimensions 1600 x 900 pixels. Within each grid cell, the number of pixels covered by the mask is counted to determine the ratio of the total number of pixels per grid cell to the number of pixels covered by the mask. This count serves as the basis for calculating a correction factor, which is then applied to the c values through multiplication.
Both of these steps were executed in PyCharm, whereas the following steps were proceeded in JupyterLab. After reading the reshaped and corrected PIV and LIF data in a JupyterLab script, the second correction of the LIF data, addressing the correct combination of the different LIF data arrays (c_1, c_2, c_3, and c_4), was carried out. This process is illustrated in Figure 4.15.

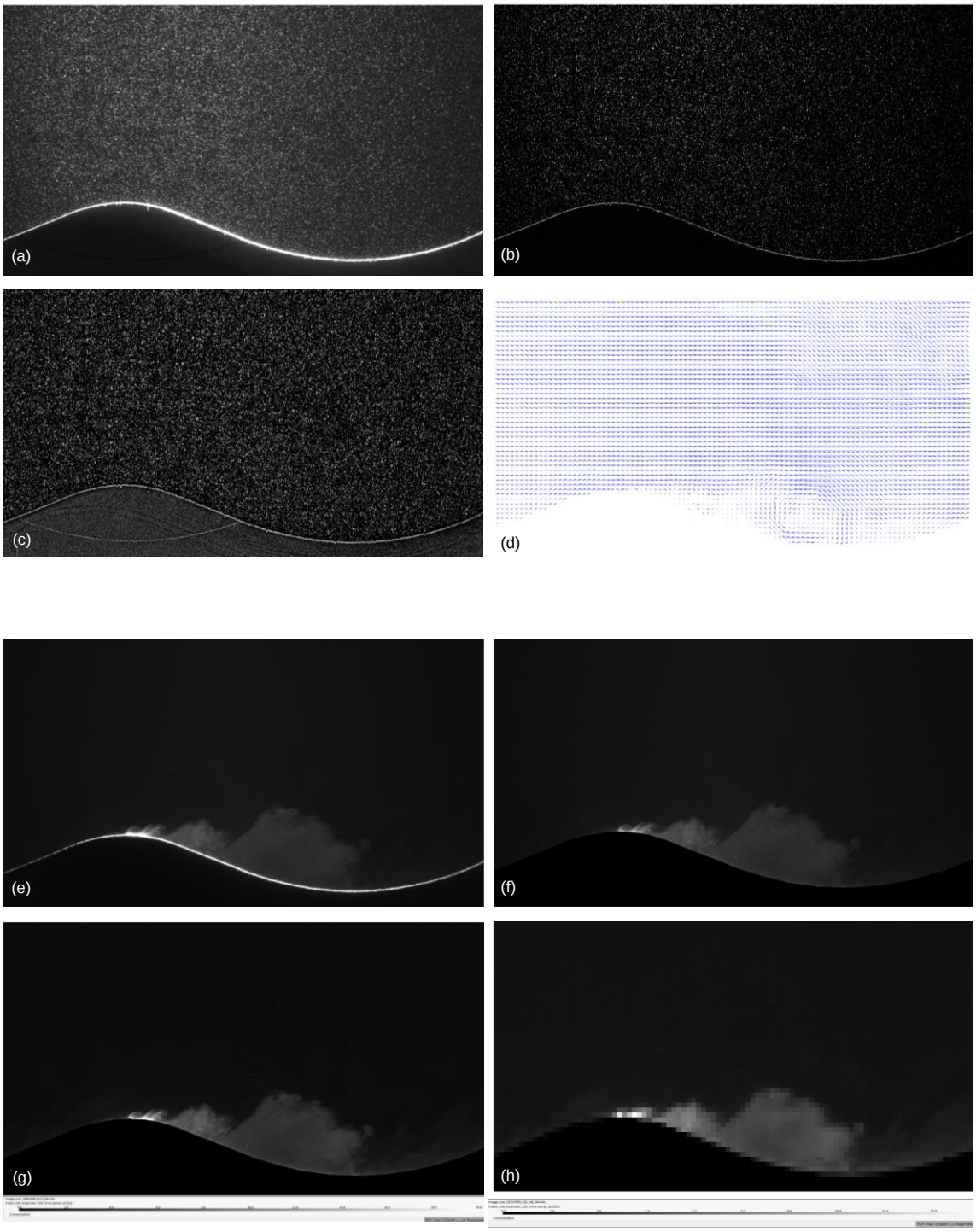

Figure 4.14: Image processing and calculation of time-resolved velocity and concentration fields in Dantec DynamicStudio (a) Raw PIV image (double frame) (b) Subtraction of *Image Mean* (c) Balanced PIV image (d) PIV vector field (outcome of *Adaptive PIV* algorithm) (e) Raw LIF image (single frame) (f) Masked LIF image (g) LIF image after *LIF-Processing* (h) Resampled LIF image

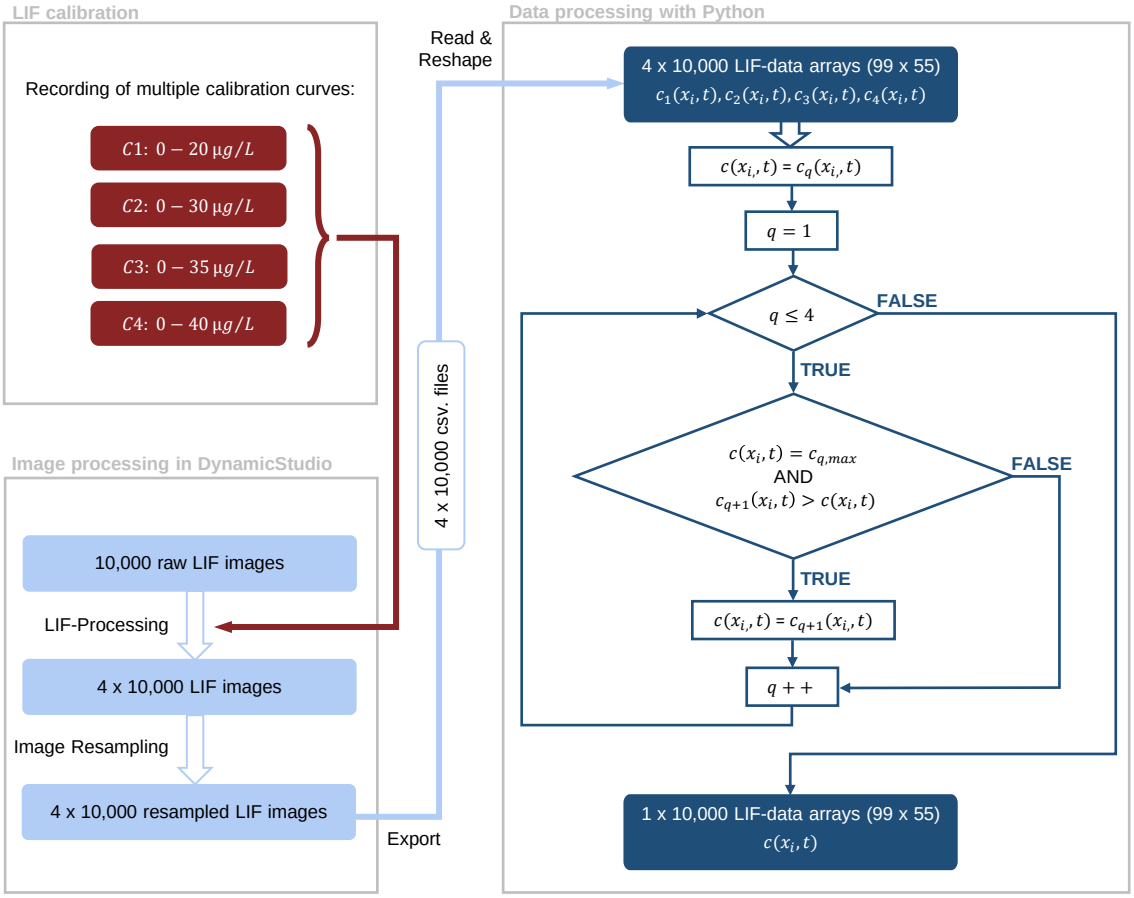

Figure 4.15: Processing of LIF data combining multiple calibration curves to prevent information loss: During the LIF calibration, four calibration curves with increasing maximum concentration were recorded. These curves were used for *LIF-Processing* in DynamicStudio resulting in 4 x 10,000 LIF data sets, which were subsequently resampled and exported. In a custom Python script, the respective data arrays were combined following the depicted flowchart. The outcome is a set of 10,000 combined 99 x 55 c data arrays.

The process begins by assigning the data arrays $c(x_i, t)$ to the first LIF data arrays $c_1(x_i, t)$. Subsequently, for every time step and each of the 99 x 55 elements of the arrays, two conditions are checked: whether $c(xi, t)$ is equal to the maximum concentration value of the respective calibration curve $c_{q,max}$ (here: 20 µg/L), and whether $c_{q+1}(x_i, t)$ is greater than $c(x_i, t)$. If both conditions are satisfied, the respective element of the arrays $c(x_i, t)$ is updated to $c_2(x_i, t)$. This iterative process repeats, ensuring that at each step, the LIF data arrays $c(x_i, t)$ are updated to reflect the maximum values identified from the subsequent data arrays.

Thus, the effect of overexposure was prevented without losing information in the darker regions of the images. This procedure results in 1 x 10,000 c data arrays.

To achieve comparability between the different measurement configurations, despite the varying Rhodamine 6G concentration of the respectively injected tracer fluid $c_{\mathrm{R6G,\ Tracer}}$, the resulting values within the c data arrays were normalised with $c_{\mathrm{R6G,\ Tracer}}$ used for the corresponding experimental configuration, see Table 4.4. This means, that at each point of the FoV and for every time step, the Rhodamine 6G concentration measured in

the water column $c_{\mathrm{R6G}}(x_i, t)$ was normalised with $c_{\mathrm{R6G,\ Tracer}}$ following Equation 4.3 to obtain the concentration of tracer fluid dissolved in the water column $c(x_i, t)$, with units of $[c(x_i, t)] = \mathrm{L/m^3}$, which will hereafter be referred to as tracer fluid concentration.

$$c(x_i, t)\left(\mathrm{L/m^3}\right) = 1000\left(\mathrm{L/m^3}\right) \cdot \frac{c_{\mathrm{R6G}}(x_i, t)\,(\ \mu\mathrm{g/L})}{c_{\mathrm{R6G,\ Tracer}}\,(\ \mu\mathrm{g/L})} \tag{4.3}$$

After these steps of data preparation, the data was phase-averaged to compute fluctuation values. These were necessary to subsequently calculate the quantities, which were selected to investigate the measurement results regarding the influence of the flow-topography interaction on the turbulent transport behaviour.

4.4.1 Phase Binning and Calculation of Phase Averages

As the purpose of this study is to quantify turbulent transport by calculating vertical turbulent fluxes according to Equation 3.13, it is necessary to compute the fluctuation values of the vertical velocity $w'(x_i, t)$ and the concentration $c'(x_i, t)$. To quantify turbulence by turbulent kinetic energy as given in Equation 3.11, it is additionally required, to determine the fluctuation values of the horizontal velocity $u'(x_i, t)$. Due to the oscillating nature of the examined flow, these fluctuation values can not simply be calculated by subtracting the time-averaged value of the respective variable from the instantaneous values, but a phase average is needed as a reference, as constituted by Equation 3.20.

To facilitate phase averaging of the obtained data, the previously prepared u-, w-, and c- arrays corresponding to distinct time steps had to be sorted into phase bins, each representing a range of phase angles. This range is termed the bin width and is defined by its total angle span as well as its median phase angle. The whole wave cycle of 360° divided by the bin width gives the number of phase bins N_{pb} (e.g. $\varphi = 0 \pm 5°$ corresponds to a bin width of 10° and $N_{pb} = 36$). The binning and averaging procedure is schematically illustrated in 4.16. The number of phase bins N_{pb} over the whole wave cycle was chosen based on a statistical evaluation following [Ostermann et al., 2015]. This choice must strike a balance between reducing signal noise and preserving the inherent flow characteristics. If the number of phase bins is too low, the assumption of a constant mean value across the entire phase bin is no longer valid, resulting in artificially amplified fluctuations in the computed values. Conversely, while increasing the number of phase bins tends to reduce the overestimation of fluctuation values, it also decreases the number of entries per bin. This reduction lowers the accuracy of the phase-averaged values and increases their sensitivity to outliers.

To determine the optimal number of phase bins, the root mean square deviation (RMSD) of the horizontal velocity was derived following Equation 4.4. The phase-averaged horizontal velocity field obtained for a particular number of phase bins $\langle u_{N_{pb},k} \rangle$ is subtracted from the phase-averaged result of the next smaller phase bin number $\langle u_{N_{pb}-1,k} \rangle$, meaning that for each phase angle, the standard deviation of the entire flow field difference is calculated. The spatial and temporal averaging of the standard deviation produces a value that, while not directly representative of the flow field, serves as an indicator for assessing the quality

of the results. This value is anticipated to reach its minimum when the maximum amount of flow effects is preserved while minimizing noise. Further increases in the resolution of the phase-averaged data are constrained by data quality, as the flow features being resolved may eventually approach the magnitude of the noise.

$$RMSD = \sqrt{\frac{\sum_{k=1}^{N_{pb}} (\langle u_{N_{pb},k} \rangle - \langle u_{N_{pb}-1,k} \rangle)^2}{N_{pb}}} \tag{4.4}$$

Following this approach, it was determined that $N_{pb} = 100$ represents a good compromise for the three wave scenarios employed, resulting in a bin width of 3.6°.
The distinctive phase bin, in which the data arrays corresponding to a certain time step were sorted, was selected based on the phase of the far field velocity. As representative of this phase, the horizontal velocity component at the upper edge of the FoV $u_{top}(t)$ was identified. To prevent mistakes due to the impact of boundary effects of the adaptive PIV correlation, the horizontally averaged value of u within the second to last row ($z_{max} := z(z_{index} = 53)$) was used as an indicator for the wave phase angle and calculated following Equation 4.5.

$$u_{top}(t) = \langle u \rangle_x (z = z_{max}, t) = \frac{1}{X_{FoV}} \sum_{k=1}^{X_{FoV}} u(x_k, z_{max}, t) \tag{4.5}$$

The angular brackets combined with the index x indicate a horizontally averaged value of the horizontal velocity $\langle u \rangle_x$. The variable X_{FoV} corresponds to the number of data entries in the horizontal direction of the data array (representing the FoV), thus, in this case, $X_{FoV} = 99$.
Once u_{top} was determined for every time step, the exact time of zero crossings t_{zc} of this variable was identified by linear interpolation. Whenever the sign of u_{top} changed from negative to positive, this was assigned as the beginning of a new wave cycle, as indicated in Figure 4.16, marked by the dashed blue line. If, however, the sign changed from positive to negative, the second half of the wave cycle started indicating the change of the flow direction. For every time step, the individual period $T(t)$ of the present wave cycle was determined by the time difference between the zero crossing time of the present wave cycle and the zero crossing time of the following wave cycle. Thus, for every time step, the phase angle $\varphi_{ts}(t)$ can be computed based on the difference between the exact time of that time step t and the exact time of the last zero crossing $t_{zc}(t)$ of $u_{top}(t)$ and the respective period $T(t)$ of the present wave cycle, as depicted in Equation 4.6.

$$\varphi_{ts}(t) = 2\pi \frac{t - t_{zc}(t)}{T(t)} \tag{4.6}$$

Based on the respective phase angle $\varphi_{ts}(t)$, the data arrays of u, w, and c for each time step were sorted into $N_{pb} = 100$ phase bins. The phase bin number of every time step $n_{pb}(t)$ is defined by Equation 4.7, with // standing for integer division. Please note, that N_{pb} refers to a quantity, whereas n_{pb} refers to a numbering.

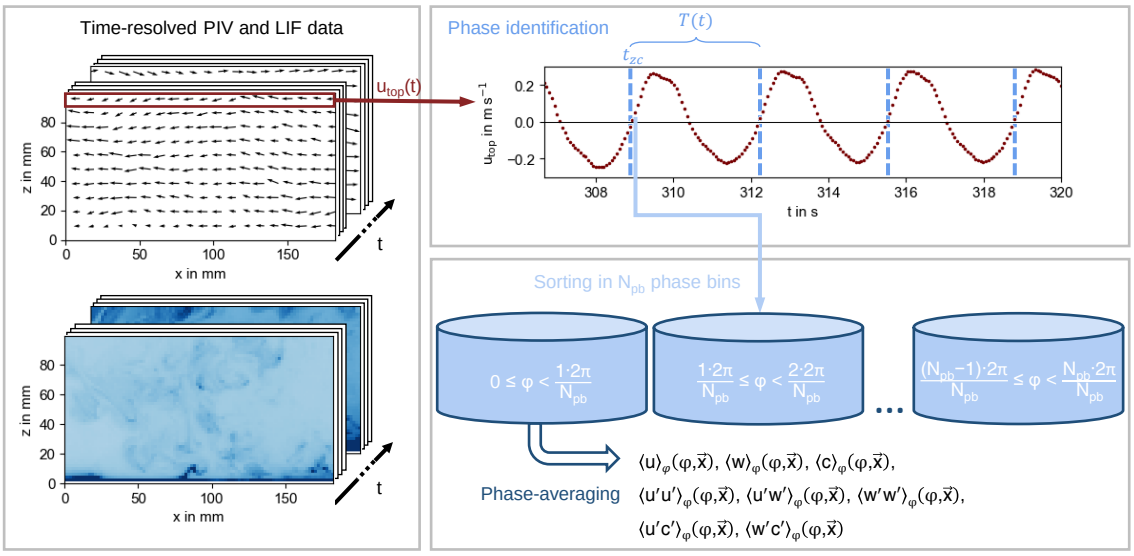

Figure 4.16: Scheme of phase binning and averaging method (illustration adapted from [Stirnweiß et al., 2024a]): Dependent on the respective phase angle $\varphi(t)$ of $u_{top}(t)$, time-resolved velocity (u, w) and concentration (c) data arrays are sorted into N_{pb} phase bins. This allows for the calculation of phase-averaged values of u, w and c and, thus, fluctuation values giving phase-resolved results for Reynolds stresses or turbulent fluxes. Note that the 99 x 55 data arrays spatially correspond to a FoV of 167.57 mm x 93.28 mm.

$$n_{pb}(t) = \varphi_{ts}(t) \;//\; \frac{2\pi}{N_{pb}} \tag{4.7}$$

For each phase bin n_{pb}, the phase averages of u, w, and c were computed by averaging all data arrays of each variable, which were sorted into that bin, as represented by Equation 4.8 with E_{pb} corresponding to the number of entries within the respective phase bin.

$$\langle\gamma\rangle_{\varphi}(x_i, \varphi := 2\pi\frac{n_{pb}}{N_{pb}}) = \frac{1}{E_{pb}(n_{pb})}\sum_{k=1}^{E_{pb}}\gamma(x_i, t_k) \tag{4.8}$$
$$\text{with } n_{pb} \in \{0, ..., N_{pb}-1\} \text{ and } \gamma \in \{u, w, c\}$$

The described phase binning and averaging method facilitates the subsequent computation of fluctuation values.

4.4.2 Calculation of Phase-resolved and Time-averaged Quantities

According to the Reynolds decomposition for oscillating flow fields given in Equation 3.19, the fluctuation values of u, w and c were calculated by subtracting the phase-averaged values from Equation 4.8 from the instantaneous values following Equation 4.9.

$$\gamma'(x_i, t) = \gamma(x_i, t) - \langle\gamma\rangle_{\varphi}(x_i, \varphi(t)) \text{ with } \gamma \in \{u, w, c\} \tag{4.9}$$

By multiplication of the fluctuation values $u'(x_i, t)$ or $w'(x_i, t)$ and $c'(x_i, t)$ the turbulent fluxes $u'c'(x_i, t)$ or $w'c'(x_i, t)$ could be derived for every time step.

The in-plane turbulent kinetic energy $TKE_{xz}(x_i, t)$ for every time step was calculated following Equation 4.10 and will be abbreviated as TKE from this point onwards.

$$TKE_{xz}(x_i, t) = \frac{1}{2}(u'(x_i, t)^2 + w'(x_i, t)^2) \tag{4.10}$$

The time-specific values were then phase-averaged following Equation 4.8 to obtain the phase-resolved results $\langle u \rangle_\varphi(x_i, \varphi)$, $\langle w \rangle_\varphi(x_i, \varphi)$, $\langle c \rangle_\varphi(x_i, \varphi)$, $\langle TKE_{xz} \rangle_\varphi(x_i, \varphi)$, and $\langle w'c' \rangle_\varphi(x_i, \varphi)$, which are presented in Chapter 5. These phase- and spatially resolved outcomes provide intuitively understandable insights into the phase-dependent processes of the flow and mixing behaviour.

To allow for quantitative comparability of the outcomes corresponding to the different measurement configurations, time-averaged profiles of the concentration, TKE, and the vertical turbulent flux depending on the bottom distance z^* were determined. The bottom distance z^* corresponds to the difference between the z-coordinate and the bottom height z_0 of the artificial seabed.

Therefore, the phase-resolved results were first, horizontally averaged according to Equation 4.11 and second, averaged among all phase bins following Equation 4.12 giving $\langle \overline{c} \rangle_x(z^*)$, $\langle \overline{TKE_{xz}} \rangle_x(z^*)$, and $\langle \overline{w'c'} \rangle_x(z^*)$. To ensure that the horizontal averaging corresponds to the averaging over one ripple wavelength, the data arrays were previously trimmed in the x-direction to $\lambda_R = 159.22$ mm. The resulting profiles are presented in Chapter 5 as well.

$$\begin{gathered} \langle \gamma \rangle_{\varphi,x}(z^*, \varphi := 2\pi \frac{n_{pb}}{N_{pb}}) = \frac{1}{X_{FoV}} \sum_{k=1}^{X_{FoV}} \langle \gamma \rangle_\varphi(x_k, z - z_0, \varphi) \\ \text{with } n_{pb} \in \{0, ..., N_{pb} - 1\} \text{ and } \gamma \in \{c, TKE_{xz}, w'c'\} \end{gathered} \tag{4.11}$$

$$\langle \overline{\gamma} \rangle_x(z^*) = \frac{1}{N_{pb}} \sum_{k=1}^{N_{pb}} \langle \gamma \rangle_{\varphi,x}(z^*, \varphi_k) \text{ with } \gamma \in \{c, TKE_{xz}, w'c'\} \tag{4.12}$$

The turbulent mixing length l_c was derived based on Equation 3.18 by firstly calculating phase-resolved values according to Equation 4.13, which were subsequently averaged following Equation 4.14. Note that the concentration gradient in the z-direction is negative, resulting in an overall positive sign within the square root term. The respective results are presented in Chapter 5.

$$l_{c,\varphi}(z^*, \varphi) = \sqrt{-\frac{\langle w'c' \rangle_{\varphi,x}(z^*, \varphi)}{\left| \frac{\partial \langle u \rangle_{\varphi,x}(z^*, \varphi)}{\partial z} \right| \frac{\partial \langle c \rangle_{\varphi,x}(z^*, \varphi)}{\partial z}}} \tag{4.13}$$

$$l_c(z^*) = \frac{1}{N_{pb}} \sum_{k=1}^{N_{pb}} l_{c,\varphi}(z^*, \varphi_k) \tag{4.14}$$

4.4.3 Correction of the Concentration Normalization Factor of Measurement 'FLAT, calm'

After post-processing and evaluating the measurement campaign discussed in this work, it was noted that one single concentration measurement significantly deviated from comparable measurements, see Figure 4.17, despite the absence of any obvious fluid mechanical explanation. Further investigation revealed that the chosen normalization factor $c_{\mathrm{R6G,\ Tracer}}$, which refers to the Rhodamine 6G concentration used for the respective experiment, was the likely source of error.

During the campaign, measurements for all four seabed models were conducted in the following order with respect to the wave scenario: first stormy, then intermediate, and last calm. The reason behind this sequencing, was the idea, that initiating measurements with the stormy scenario, which induces the strongest wave pumping, would ensure thorough perfusion of the permeable seabed with the tracer fluid. This approach was intended to facilitate uniform discharge across all measurements.

However, with the flat seabed model, the discharge and transport of the tracer fluid exhibited significant variability depending on the wave scenario: Under the calm scenario, the tracer was barely mixed in the water column, resulting in the accumulation of a highly concentrated layer of tracer in the lowest water layer. Conversely, under the intermediate or stormy scenarios, the discharging tracer was rapidly washed away and diluted, resulting in very low instantaneous concentration values within the FoV.

To prevent overexposure on the one hand and information loss on the other, as already described in Section 4.3.3, a tracer with relatively high Rhodamine 6G concentration of $c_{\mathrm{R6G,\ Tracer}} = 1200\ \mu\mathrm{g/L}$ was injected during the intermediate and stormy wave scenario. For the calm wave scenario, a tracer with a much lower dye concentration of $c_{\mathrm{R6G,\ Tracer}} = 200\ \mu\mathrm{g/L}$ was applied. This substantial difference in concentrations is suspected of having caused the observed discrepancy. Specifically, it appears that, due to the order of measurements, the actual dye concentration during the measurement with the flat bed and the calm wave scenario was higher than intended. It is hypothesized that portions of the tracer dye were retained in the permeable bed during the measurements with the higher concentration. Although efforts were made to counteract this effect by flushing the seabed model after each measurement, this remains the most probable explanation and will be further discussed in Chapter 6.

Given the time constraints, it was not feasible to conduct an improved measurement at the point during the evaluation when this inconsistency became noticeable. Therefore, a correction factor was derived to adjust the existing measurement results. The averaged concentration value in the water layer at the top boundary of the FoV was again chosen as an indicator, as the influence of the seabed topography is minimal at this location and assuming an infinitely long experiment duration with exclusively vertical dispersion, only the value of the pump-driven inflow should be significant in this water layer. Therefore, the horizontally averaged c-value was calculated following 4.15.

Table 4.5: Average concentration value at the top boundary of the FoV $\overline{c_{top}}$, value at the beginning of the measurement $c_{top}(t = 0)$ and the average value of the absolute deviation of $c_{top}(t)$ from its linear fit for all measurements under the calm wave scenario. The ratio of the averaged concentration $\overline{c_{top}}$ of the inconsistent measurement ('FLAT, calm') and the average of the averaged concentrations obtained from the three other measurements under the calm wave scenario results into a factor of 3.5.

	Date	$\overline{c_{top}}$	$c_{top}(t = 0)$	Deviation
SIN, calm	21/07/2021	0,0013	0,0012	0,0003
NAT, calm	01/07/2021	0,0017	0,0013	0,0002
ASYM, calm	07/07/2021	0,0017	0,0012	0,0003
Average		0,0015	0,0012	0,0002
FLAT, calm	15/07/2021	0,0055	0,0043	0,0007
Relation		3,6222	3,5267	3,0034

$$c_{top}(t) = \langle c \rangle_x (z = z_{max}, t) = \frac{1}{X_{FoV}} \sum_{q=1}^{X_{FoV}} c(x_q, z_{max}, t) \tag{4.15}$$

Figure 4.18 shows the discrepancy between the measurements taken with the flat bed and the calm wave scenario, and the measurements conducted with the same wave scenario or seabed model. This is evident in both, the respective average concentration value at the top boundary of the FoV $\overline{c_{top}}$ and the value at the beginning of the measurement $c_{top}(t = 0)$, which was derived from a linear fit of $c_{top}(t)$. The increased size of the respective bubble in the plot indicates significant differences in concentration fluctuations compared to comparable measurements since the bubble size illustrates the average of the absolute deviation of $c_{top}(t)$ from its linear fit.

Therefore, $c_{\text{R6G, Tracer}}$ of the FLAT,calm-measurement was adjusted using a correction factor (cf) of 3.5, which corresponds to the ratio of the time-averaged concentration at the top edge of the FoV $\overline{c_{top}}$ of the particular measurement and the average of the $\overline{c_{top}}$-values obtained from the measurements with the rippled beds under the calm wave scenario, see Table 4.5. This adjustment yields a corrected averaged concentration profile, represented by the red line in Figure 4.17 and the red circle in Figure 4.18. Subsequently, in Chapter 5, only the corrected results will be presented and compared with the remaining measurements.

Notably, $\overline{c_{top}}$ and $c_{top}(t)$ are also high for the measurements with the naturally rippled seabed and the intermediate and stormy wave scenario. However, the average of the absolute deviation of $c_{top}(t)$ from its linear fit, indicated by the bubble size, is less conspicuous. In addition, the high concentration values can be explained by physical reasons, as detailed in 6. Therefore, there was no reason to correct these two measurements.

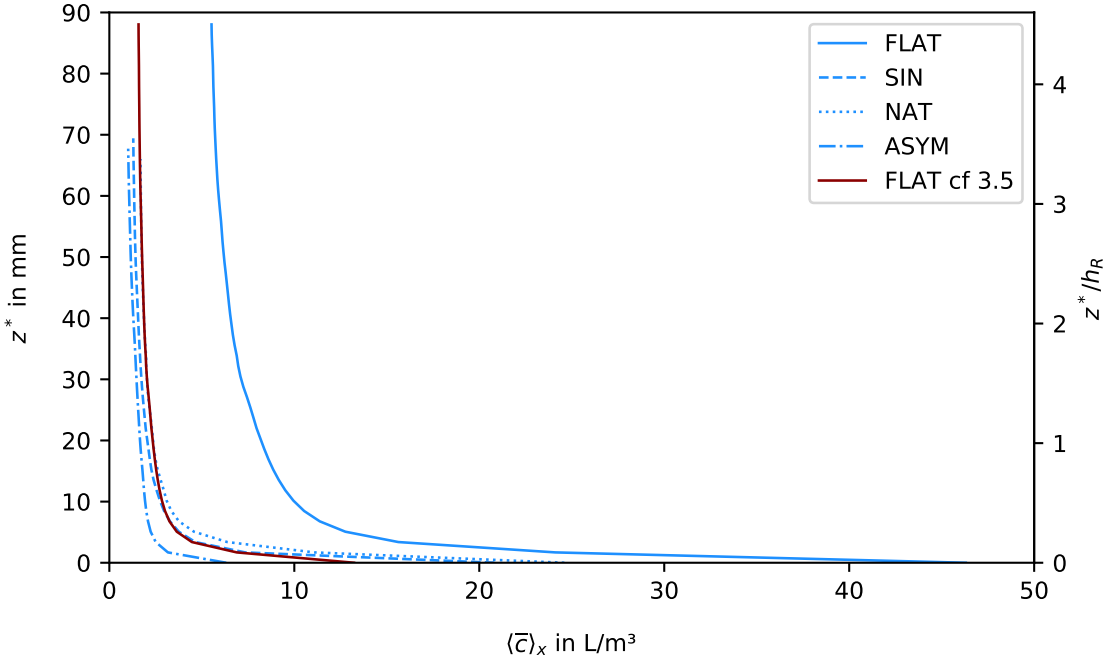

Figure 4.17: Time-averaged profiles of the concentration depending on the bottom distance under the calm wave scenario. The red curve refers to the corrected c-values for measurement 'FLAT, calm', which are scaled by the correction factor 3.5.

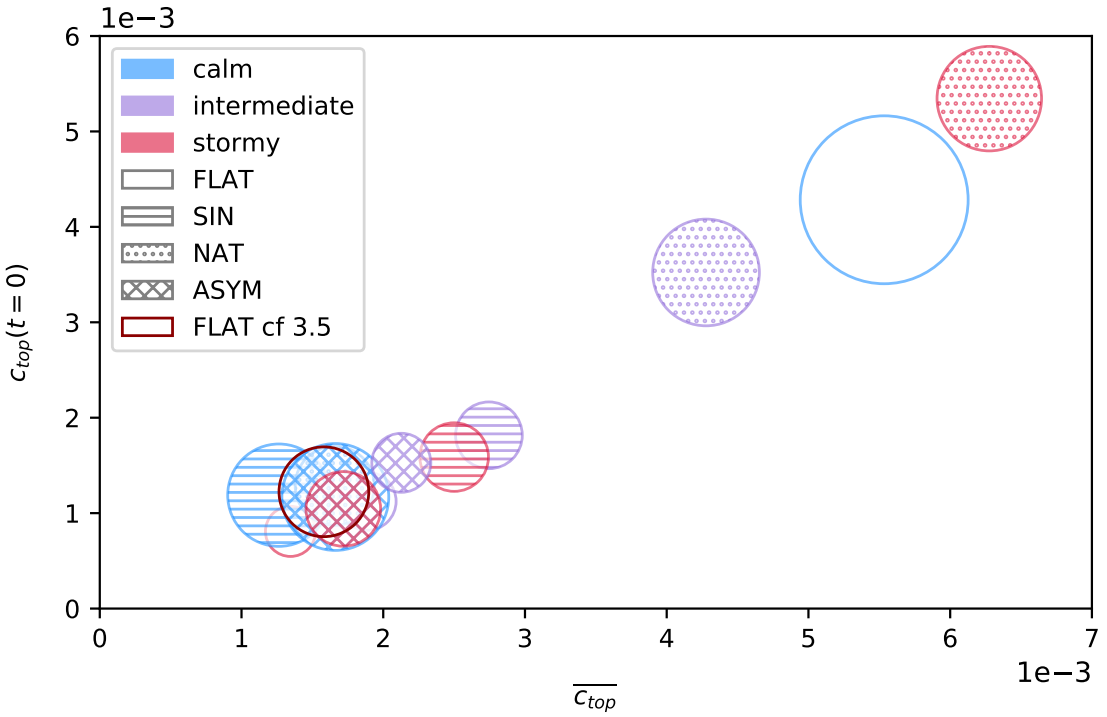

Figure 4.18: Concentration measurement 'FLAT, calm' deviates from similar measurements (with either a flat seabed, indicated by the unfilled circles, or under the calm wave scenario, indicated by blue coloured markers) in terms of time-average $\overline{c_{top}}$ (x-axis), its fitted starting point $c_{top}(t=0)$ (y-axis) and the average of the absolute deviation of $c_{top}(t)$ from its linear fit (bubble size), which can be understood as an indicator for the concentration fluctuations. The corrected concentration data, scaled by the correction factor 3.5, is represented by the red circle and matches the values of the other measurements with the calm wave scenario or flat seabed.

Chapter 5

Results

5.1 Oscillating Far-Field Velocity

As detailed in Section 4.4, the reference metric utilized for phase bin identification was the oscillating far-field velocity, obtained by horizontally averaging the vertical velocity in the top level of the FoV, denoted as u_{top}. Figure 5.1 depicts the resulting phase-averaged far-field velocity $\langle u_{top} \rangle_{\varphi}(\varphi)$ throughout the entire wave cycle above all four seabed models and under all three wave scenarios. It should be noted that the variable is plotted over the wave phase φ rather than time t, and therefore, the plot does not reflect the differences in wave period T, which were specified in Section 4.2.1.
Notably, the seabed topography slightly alters $\langle u_{top} \rangle_{\varphi}$. The profiles above the flat bed appear slightly shifted, predominantly resulting in lower velocities. Additionally, the zero-crossing points, indicative of the inflexion point of the wave direction, are somewhat shifted towards lower phase angles.
Moreover, the figure illustrates that two of the three wave scenarios employed in this study were not symmetric. The zero-crossing occurs well before $\varphi = \pi$ under the intermediate and the stormy scenario, indicating that the second half of the wave cycle is prolonged.
Furthermore, in the case of the stormy wave scenario, a plateau forms in the first half of the wave cycle, indicating a longer duration of high-velocity values compared to the intermediate scenario, where $\langle u_{top} \rangle_{\varphi}$ decreases more rapidly after reaching its maximum. The calm wave scenario exhibits significantly smaller velocity amplitudes and a distinct plateau around the maximum value, especially during the first half-cycle.
It was observed that the intermediate wave scenario either produced outcomes closely resembling those of the stormy wave scenario or exhibited characteristics similar to a precursor of processes more pronounced under the stormy wave scenario. Therefore, the following section primarily presents the phase-resolved results of the stormy wave scenario rather than those of the intermediate scenario.

5.2 Comparison of Turbulent Transport Above the Flat and the Sinusoidal Rippled Seabed Model

The subsequent section presents the outcomes of velocity and concentration measurements conducted above the flat and the sinusoidal rippled seabed model facilitating a comparative analysis. Additionally, computations of the in-plane turbulent kinetic energy TKE_{xz} (TKE) will depict the occurrence of turbulence within the observed domain. Moreover, vertical turbulent fluxes will serve to quantify the turbulent transport of discharging tracer

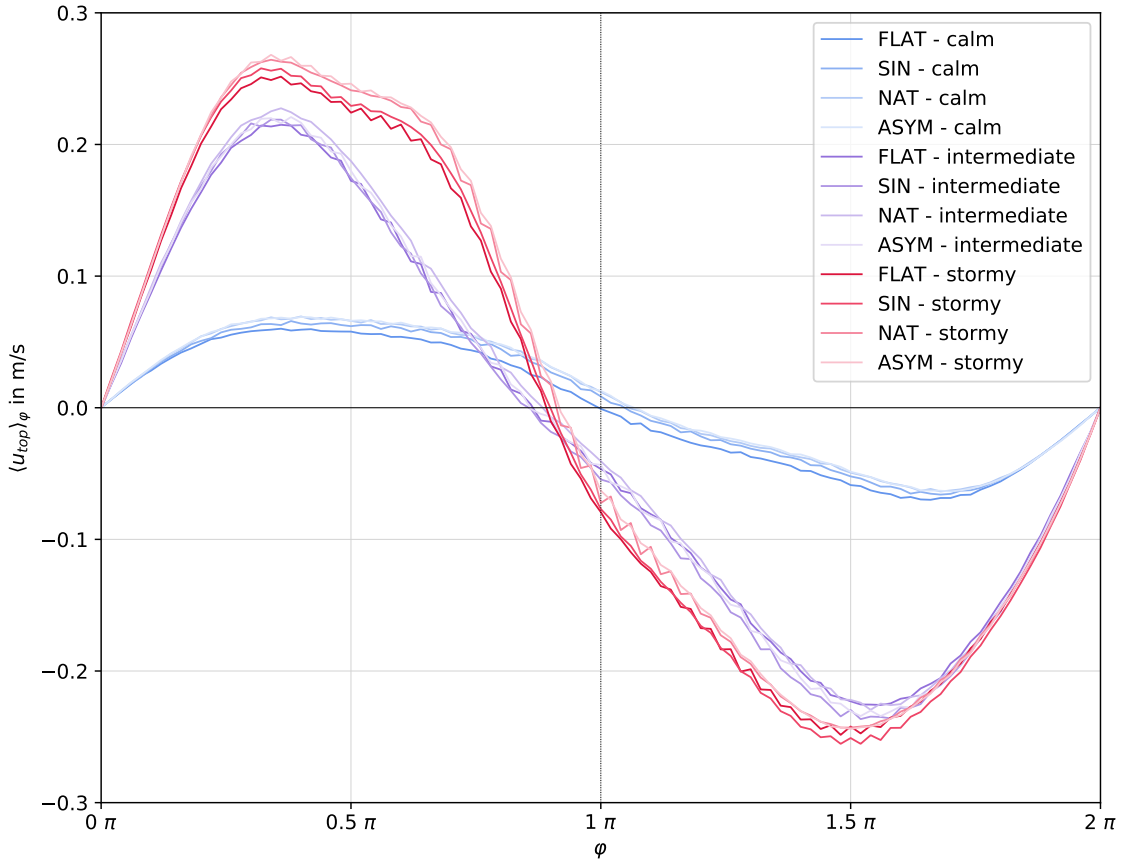

Figure 5.1: Phase average of the horizontally averaged velocity in the top level of the FoV $\langle u_{top} \rangle_\varphi(\varphi)$ for all twelve experimental configurations. The wave scenarios are indicated by blue-coloured lines for the calm, purple-coloured lines for the intermediate, and red-coloured lines for the stormy one. Here, the different seabed models, flat (FLAT), sinusoidal rippled (SIN), symmetric naturally rippled (NAT) and asymmetric naturally rippled (ASYM) are indicated by varying shades of these colours. Note that the varying period T of the wave scenarios is not visualised in the plot due to the representation over φ.

fluid. Selected phase-resolved results will be contrasted with time- and horizontally averaged profiles.

Tracer Fluid Distribution

Figure 5.2, 5.3 and 5.4 show maps illustrating phase-resolved velocity and concentration fields for four characteristic phases observed above both the flat and the sinusoidal rippled bed under the calm, the intermediate, and the stormy wave scenario. Note that, in the vector field plots, only every fifth vector is shown for clarity, and the vector lengths are scaled independently for each phase. In the middle column of the Figures the horizontally averaged vertical velocity $\langle u_{top} \rangle_\varphi$ is presented as an indicator of the phase's position within the wave cycle. Phase (a) represents the instance of maximum horizontal velocity. Phase (b) captures the moment when the horizontal velocity is about to change direction. In phase (c), the horizontal velocity once again peaks, but in the negative direction. Finally, phase (d) depicts the reversal of the wave's horizontal velocity direction.
Under the calm wave scenario, as depicted in Figure 5.2, the flow remains attached to the seabed surface throughout the entire period above both seabeds. The tracer fluid concentration is observed to be highest within a thin layer directly at the bottom surface and exhibits minimal variation across different phases. However, under the intermediate wave scenario, as illustrated in Figure 5.3, the tracer fluid concentration in the near bed boundary layer is overall lower than under the calm scenario. Above the flat seabed only little variation of the tracer fluid distribution can be observed over the wave cycle. Conversely, above the sinusoidal rippled seabed phase-dependency is even more pronounced: a cloud of tracer fluid appears to be carried away by the flow and flips to the respective lee side of the ripple crest as the wave direction changes. Thus, a variation of the concentration field across different phases is notable. In phases (b) and (d) a small swirl is visible in the respective lee side wake of the ripple crest. The flow does not follow the seabed surface throughout the whole wave period. This phenomenon is even more pronounced under stormy wave conditions, as illustrated in Figure 5.4. As the wave changes its flow direction, a recirculation zone develops in the depression behind the ripple crest. A tracer fluid cloud is expelled at the ripple crest and follows the flow direction. During phases (a) and (c), at the points of maximum horizontal velocity, this cloud exhibits a flattened shape. In phases (b) and (d), when the eddies form, the cloud extends in height and nearly occupies the space between the ripple crest and trough.
When examining the profiles of the time- and horizontally averaged concentration $\langle \overline{c} \rangle_x$ depicted in Figure 5.5, it becomes apparent that, under the calm wave scenario, the tracer fluid distribution above the flat and rippled seabeds is similar outside the boundary layer. Though, in proximity to the seabed, the horizontally averaged concentration above the rippled bed exceeds that above the flat bed. Under the intermediate and stormy wave scenarios, the near-bed tracer fluid concentration remains nearly identical, while the presence of rippled seabed results in elevated concentration values in the upper water layers. Overall, the calm wave scenario induces significantly higher time- and horizontally averaged concentration values directly at the seabed interface compared to the other two scenarios.

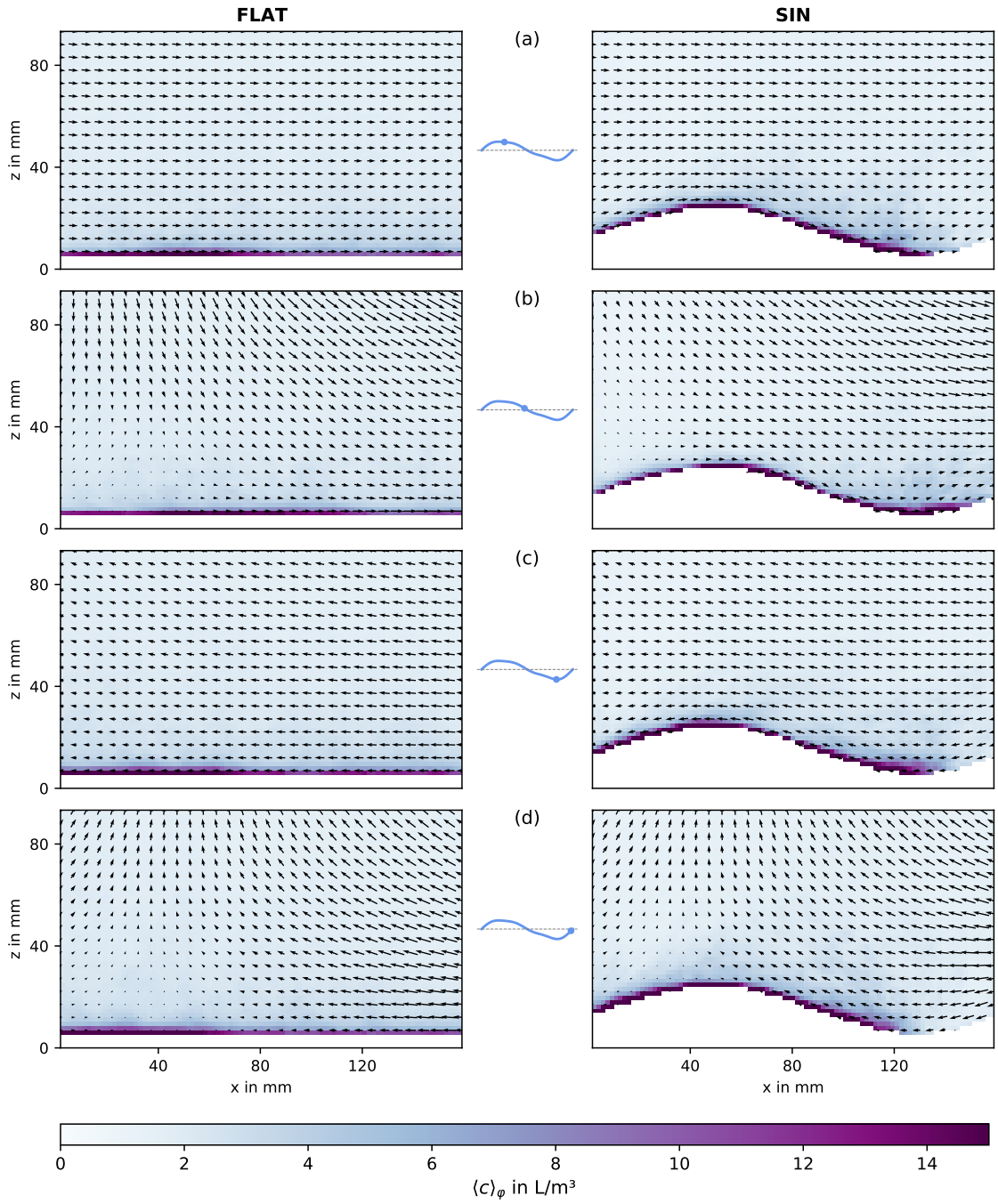

Figure 5.2: Tracer fluid distribution $\langle c \rangle_\varphi$ and velocity fields $\langle \mathbf{u} \rangle_\varphi$ for specific phases of the wave cycle under the calm wave scenario above both the flat seabed (left) and the sinusoidal rippled seabed (right). The middle column plot indicates the corresponding phase's position within the wave cycle. The absolute concentration was normalised with the dye concentration $c_{\mathrm{R6G,\ Tracer}}$ of the injected tracer fluid.

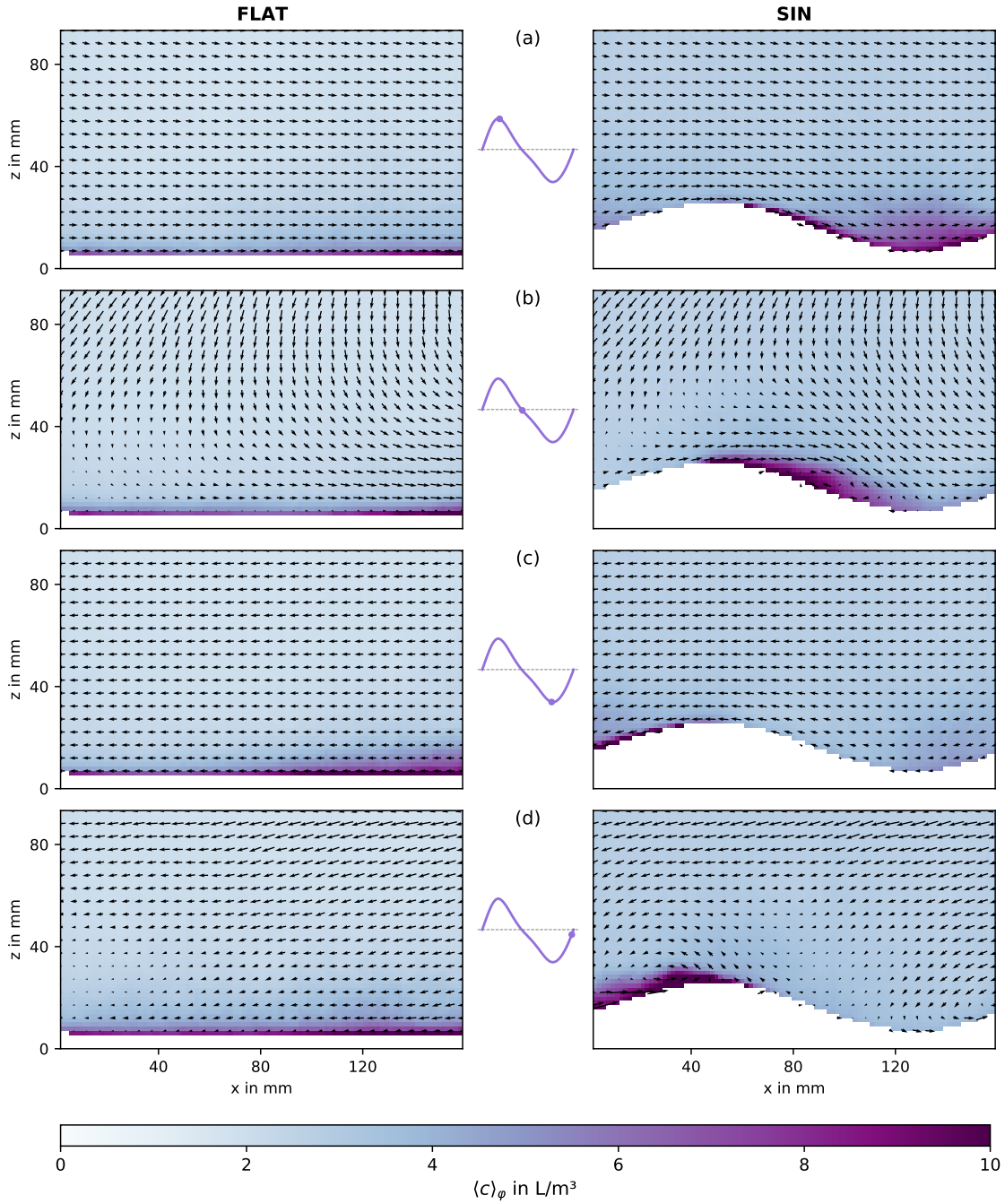

Figure 5.3: Tracer distribution $\langle c \rangle_\varphi$ and velocity fields $\langle \mathbf{u} \rangle_\varphi$ for specific phases of the wave cycle under the intermediate wave scenario above both the flat sea bed (left) and the sinusoidal rippled sea bed (right). The middle column plot indicates the corresponding phase's position within the wave cycle. The absolute concentration was normalised with the dye concentration $c_{\mathrm{R6G,\ Tracer}}$ of the injected tracer fluid.

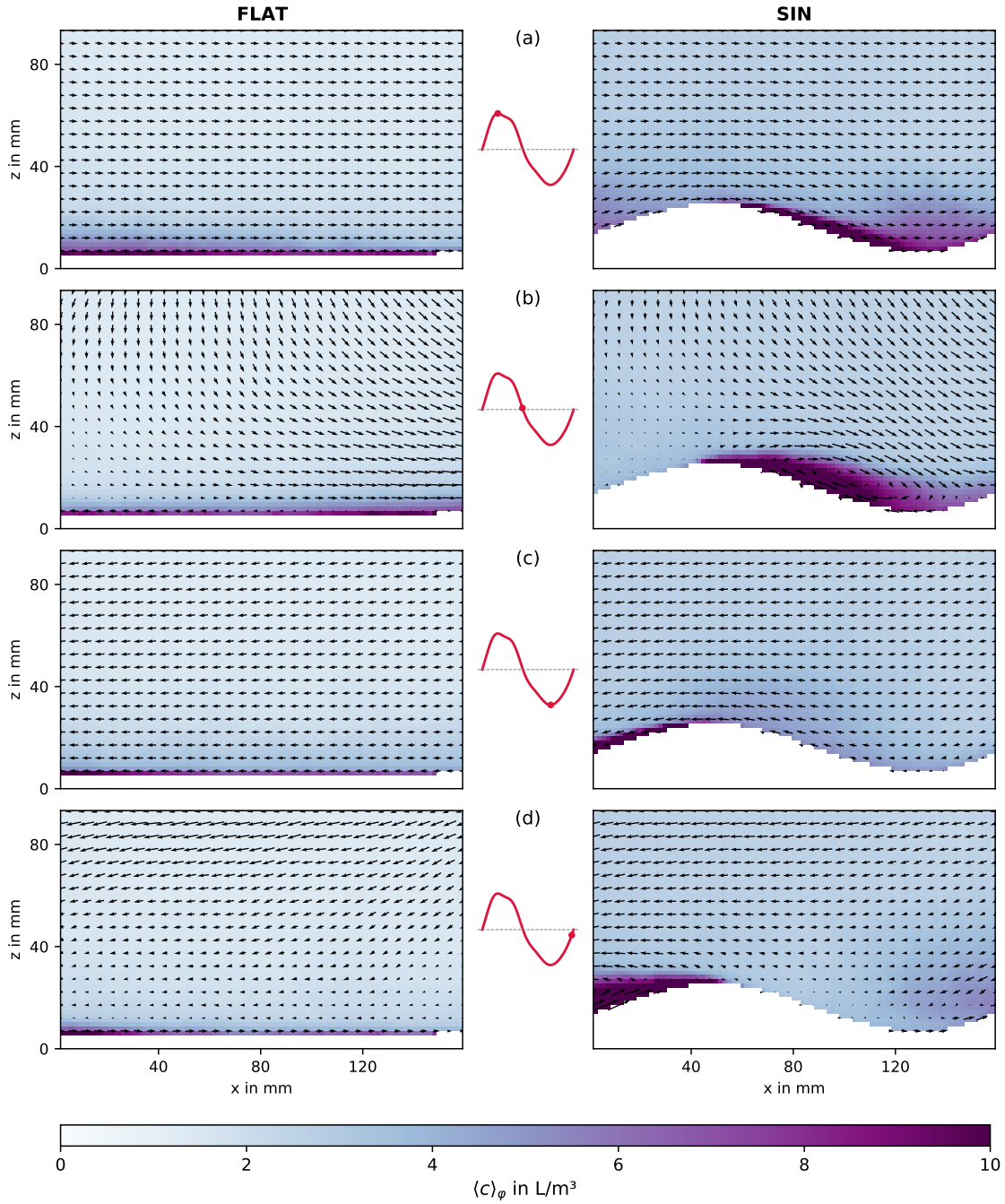

Figure 5.4: tracer fluid distribution $\langle c \rangle_\varphi$ and velocity fields $\langle \mathbf{u} \rangle_\varphi$ for specific phases of the wave cycle under the stormy wave scenario above both the flat seabed (left) and the sinusoidal rippled seabed (right). The middle column plot indicates the corresponding phase's position within the wave cycle. The absolute concentration was normalised with the dye concentration $c_{\mathrm{R6G,\ Tracer}}$ of the injected tracer fluid.

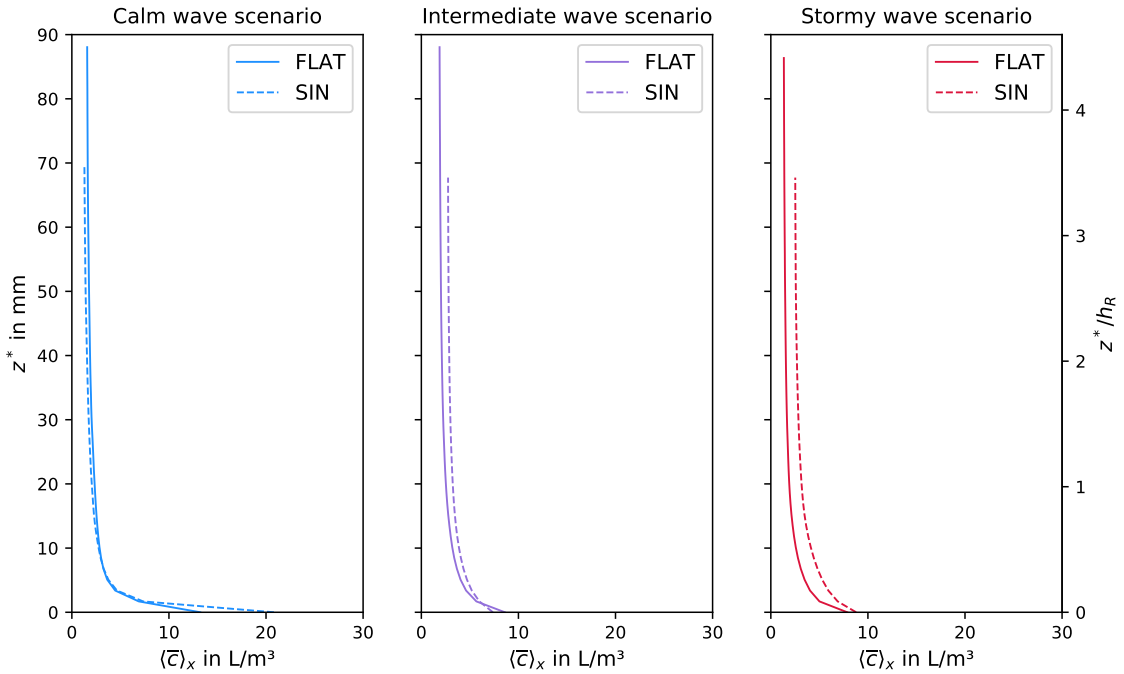

Figure 5.5: Time- and horizontally averaged tracer fluid concentration $\langle\overline{c}\rangle_x$ dependent on the bottom distance z^* above the flat and the sinusoidal rippled seabed under the calm (left), the intermediate (middle) and the stormy (right) wave scenario. On the right y-axis, the bottom distance was normalised with the ripple height h_R.

Turbulent Kinetic Energy

Figure 5.6 presents the corresponding profiles of the time- and horizontally averaged in-plane turbulent kinetic energy $\langle\overline{TKE_{xz}}\rangle_x$. Under the calm wave scenario, the TKE profiles above both the flat and the sinusoidal rippled seabeds show considerable similarity. However, under the intermediate scenario, a distinct contrast between the two seabed models becomes evident. Within a range of one ripple amplitude ($z^*/h_R = 0-1$), the TKE above the rippled bed is notably enhanced compared to that above the flat seabed. This discrepancy is even more pronounced under the stormy wave scenario. The underlying cause of this variation becomes apparent upon examining the phase-resolved TKE maps depicted in Figure 5.7. The presence of ripples induces two primary effects: firstly, it enhances the TKE directly at the bottom, especially along the downstream slope during phases with maximum horizontal velocity; secondly, the formation of recirculation zones during phases around the change in wave direction corresponds to regions of heightened TKE spanning from the ripple crest to the trough. These periodically occurring phenomena notably increase TKE within the first 20 mm of bottom distance.

Vertical Turbulent Fluxes

The vertical transport of discharging fluid is quantified by the turbulent fluxes derived from the fluctuations of the vertical velocity and the concentration of tracer fluid. Figure 5.8 illustrates the profiles of the time- and horizontally averaged vertical turbulent flux of the tracer fluid $\langle\overline{w'c'}\rangle_x$ above both beds under the three wave scenarios. Under the calm

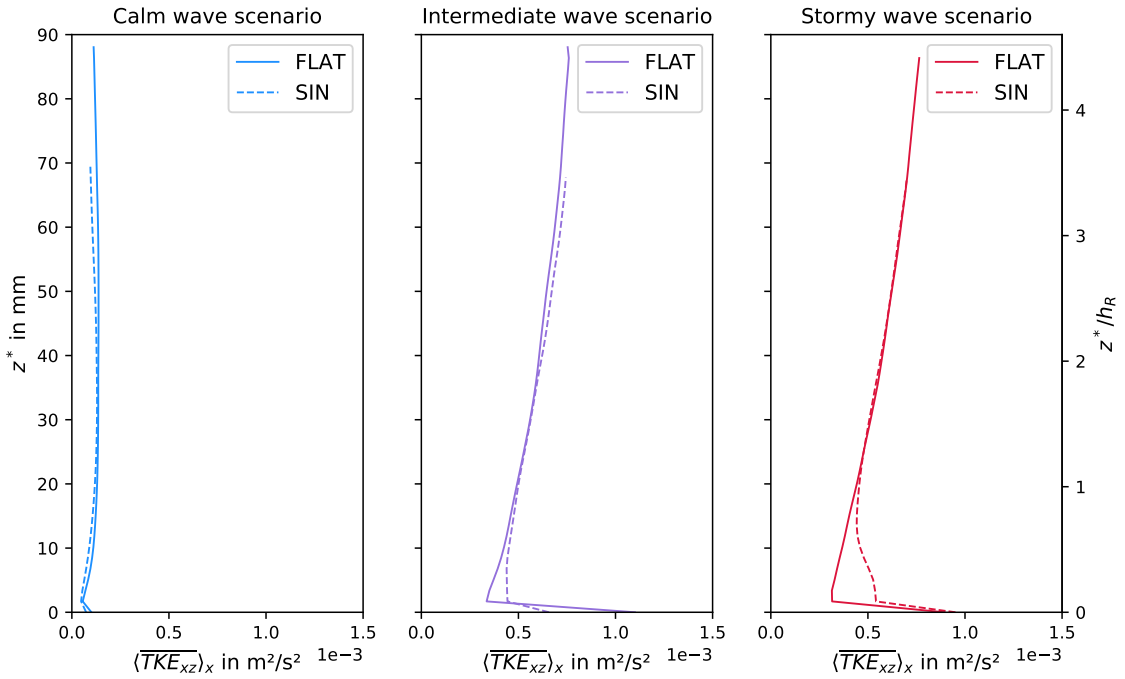

Figure 5.6: Time- and horizontally averaged in-plane turbulent kinetic energy $\langle\overline{TKE_{xz}}\rangle_x$ dependent on the bottom distance z^* above the flat and the sinusoidal rippled seabed under the calm (left), the intermediate (middle) and the stormy (right) wave scenario. On the right y-axis, the bottom distance was normalised with the ripple height h_R.

wave scenario, the vertical turbulent flux is nearly the same within the upper region of the FoV. Only within the first 10 mm of bottom distance, the turbulent flux above the rippled bed significantly exceeds the flux above the flat bed. This increase is caused by concentration fluctuation within the seabed depression due to the presence of the ripple shape. Under the intermediate and the stormy scenario, the flux above the rippled seabed is elevated compared to the one above the flat seabed nearly in the whole water layer captured in the FoV. The flux profiles above the flat bed, however, are more convex and peak at about half a ripple amplitude. In contrast, the profiles above the rippled bed peak in nearer distance to the seabed.

Figure 5.9 depicts the phase-resolved spatial distribution of the vertical turbulent flux in the case of the stormy wave scenario. Above both beds, the vertical fluxes show a distinct decrease with growing bottom distance. But whereas the vertical fluxes are relatively even in the horizontal direction above the flat seabed, significant spatial variations along the rippled seabed contour are visible. The vertical flux is substantially enhanced at the downstream slope of the ripple. In phases (a) and (c) the enhancement is limited to a thin layer directly at the seabed interface. Though, in phases (b) and (d) a larger region of increased vertical flux corresponding to the circulation of the flow field at the lee side of the ripple is clearly visible.

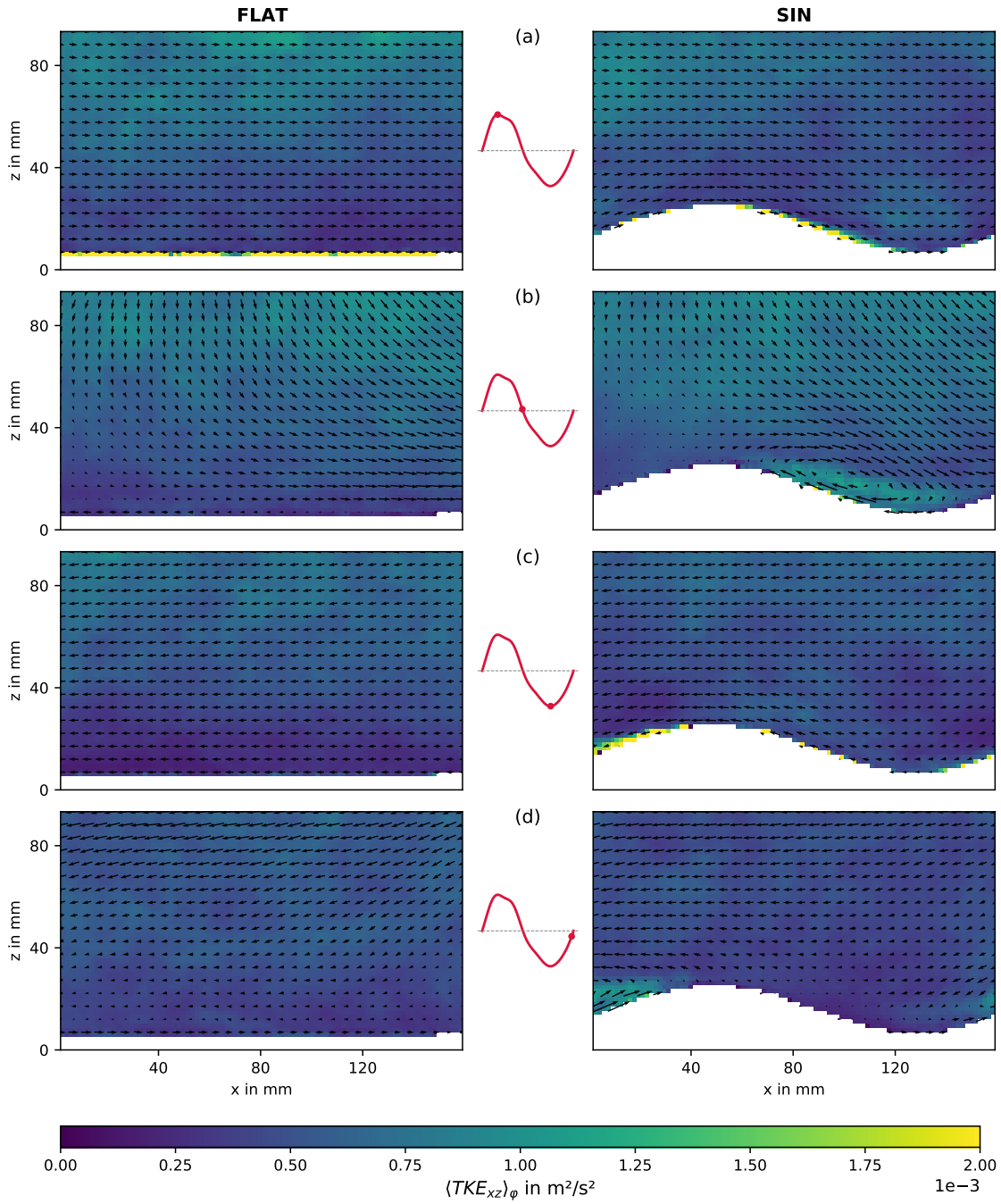

Figure 5.7: Phase averaged in-plane turbulent kinetic energy $\langle TKE_{xz} \rangle_\varphi$ and velocity fields $\langle \mathbf{u} \rangle_\varphi$ for specific phases of the wave cycle under the stormy wave scenario above both the flat seabed (left) and the sinusoidal rippled seabed (right). The middle column plot indicates the corresponding phase's position within the wave cycle.

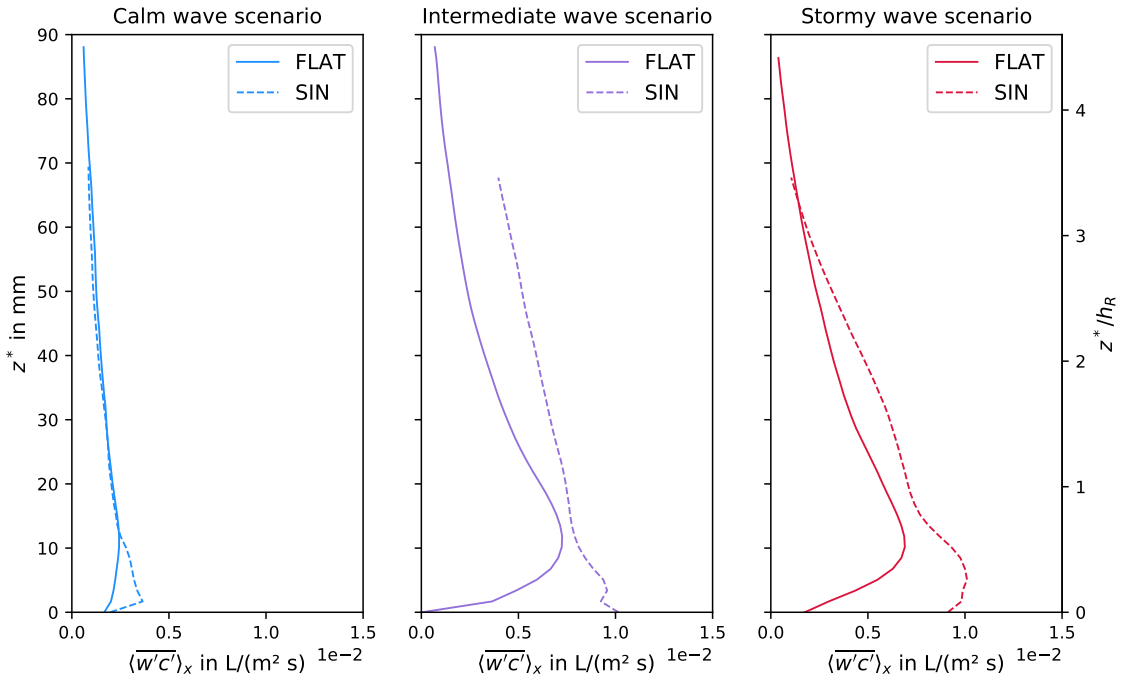

Figure 5.8: Time- and horizontally averaged vertical turbulent flux of the tracer fluid $\langle \overline{w'c'} \rangle_x$ dependent on the bottom distance z^* above the flat and the sinusoidal rippled seabed under the calm (left), the intermediate (middle) and the stormy (right) wave scenario. On the right y-axis, the bottom distance was normalised with the ripple height h_R.

Summary

The preceding analyses reveal fundamental differences in flow conditions and the distribution of a discharging tracer fluid within the water column above the flat and rippled bed. In addition, the wave scenario corresponding to a characteristic horizontal velocity and wave period was observed to have a crucial impact. Above both beds, concentration values peak directly at the bottom and decrease towards higher water layers. Under the calm wave scenario, tracer fluid accumulation within the boundary layer is higher compared to both other scenarios, where the vertical turbulent flux was observed to be significantly enhanced and therefore tracer fluid is dispersed away from its source more rapidly. Above the flat seabed, the discharge of tracer fluid at the seabed interface remains spatially uniform across all wave scenarios, yet tracer fluid concentration, turbulent fluxes, and shear, inducing turbulence at the seabed, vary periodically with the wave's phase angle. The phase-dependent variation of the concentration might be attributed to wave pumping. However, at the same time as high concentration values occur in phase (a), high TKE values were observed, rather indicating turbulent transport. In phase (c), on the other hand, elevated TKE values near the bottom are much less pronounced and barely visible. A possible explanation for this could be that the orbital velocity decreases more rapidly in phase (c) than in phase (a), see Figure 5.1.

However, above the rippled seabed, flow-topography interaction notably alters the processes of tracer fluid transport. Flow acceleration at the top of the upstream slope during high vertical velocities under the intermediate and stormy wave scenarios corresponds to a

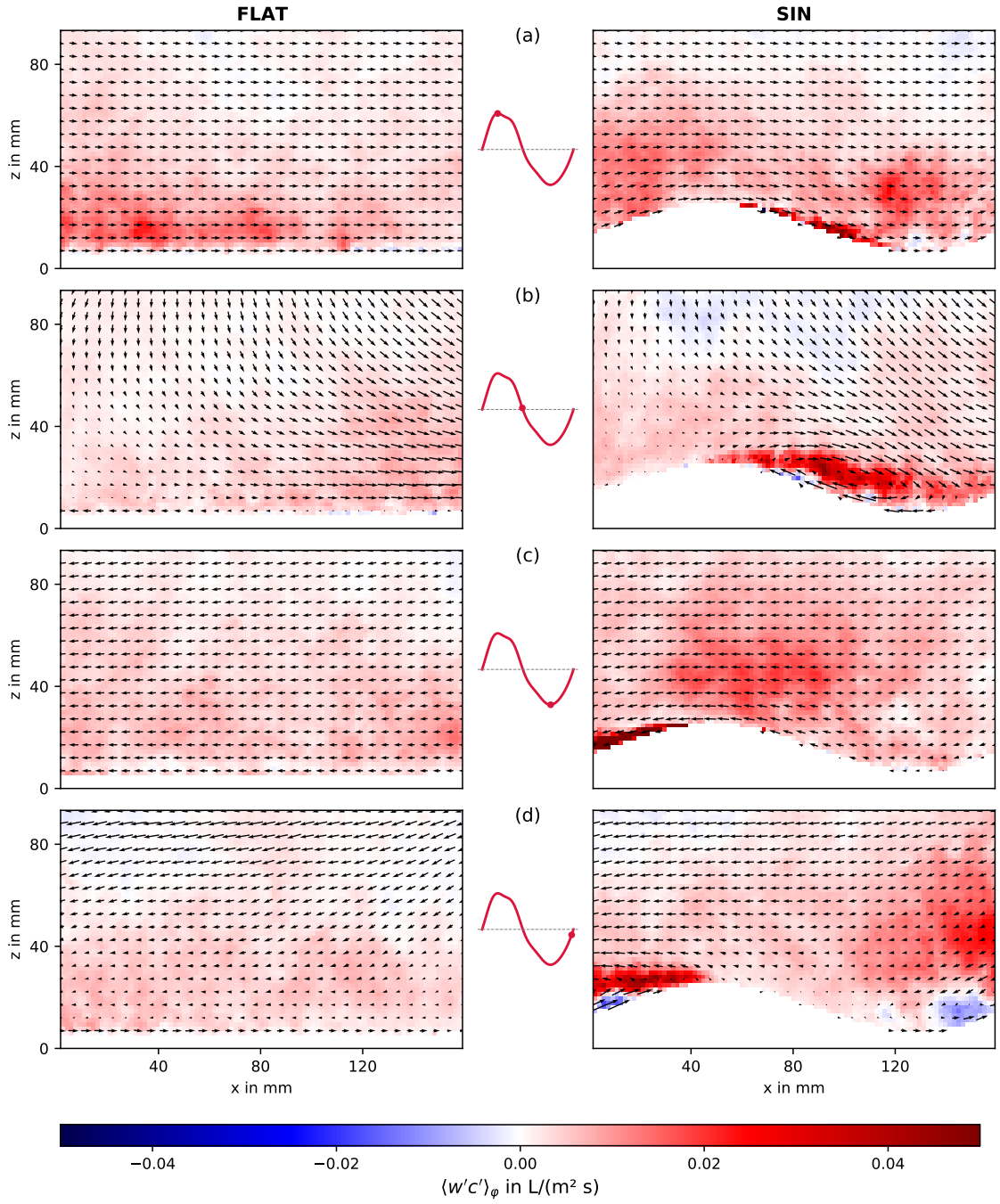

Figure 5.9: Phase averaged vertical turbulent flux $\langle w'c' \rangle_\varphi$ and velocity fields $\langle \mathbf{u} \rangle_\varphi$ for specific phases of the wave cycle under the stormy wave scenario above both the flat seabed (left) and the sinusoidal rippled seabed (right). The middle column plot indicates the corresponding phase's position within the wave cycle.

focused discharge at the ripple crest. Moreover, in the phases of wave inflection, flow field circulation emerges at the lee side of the ripple, apparently further pumping tracer fluid from the permeable seabed and leading to elevated local concentration values. Additionally, flow separation at the downstream slope significantly amplifies velocity fluctuations and thus local vertical turbulent fluxes. This in turn facilitates higher concentrations of tracer fluid in upper water layers.

5.3 Comparison of Turbulent Transport Above the Sinusoidal and the Naturally Rippled Seabed Model

The following passage will address the results of simultaneous velocity and concentration measurements obtained above the sinusoidal and the symmetric naturally rippled seabed model. Furthermore, turbulence will be visualized by calculations of in-plane turbulent kinetic energy TKE_{xz}. Additionally, vertical turbulent fluxes will quantify the turbulent transport of the discharging tracer fluid. For all of these quantities, time- and horizontally-averaged profiles will be supplemented by selected phase-resolved findings.

Tracer Fluid Distribution

In Figure 5.10 the phase-resolved velocity and concentration fields above the sinusoidal and the naturally rippled seabed are depicted across four characteristic phases of the stormy wave cycle. Note that, in the vector field plots, only every fifth vector is shown for clarity, and the vector lengths are scaled independently for each phase. Above both seabeds, flow separation occurs at the wave's inflection point, forming a recirculation zone in the downstream depression behind the ripple crest. However, the recirculation zone above the naturally rippled seabed spans a significantly larger area compared to the other bed, extending up to two ripple amplitudes above the ripple trough. Moreover, the smaller radius and therefore steeper slope of the ripple lead to a more pronounced acceleration of the flow, as evidenced in phase (d). Above both beds, a significant dependence of the tracer fluid's spatial distribution on the phase of the wave cycles can be observed. Higher concentration values occur directly at the downstream slope and are more widely distributed in phases (b) and (d) compared to phases (a) and (c). Notably, the naturally rippled bed results in a more concentrated and larger tracer fluid cloud being expelled at the ripple crest. This cloud correlates with the span of the recirculation zone in the flow field, appearing at the inflection point of $\langle u_{top} \rangle_\varphi$. In contrast, under the calm wave scenario, depicted in Figure A.1, to be found in the appendix, the flow follows the ripple contour and the tracer fluid discharge is predominantly even above the whole ripple wavelength across the whole wave cycle.

Figure 5.11 illustrates profiles of the time- and horizontally averaged tracer fluid concentration $\langle \overline{c} \rangle_x$ above the sinusoidal and the naturally rippled bed under all three wave scenarios. Under the calm wave scenario, both beds exhibit similar maximum concentration values directly at the seabed interface, showing a steep gradient within the first 10 mm of bottom distance. In higher water layers, the concentration values above the naturally rippled seabed are slightly lower than above the sinusoidal rippled bed. Under both remaining wave scenarios, a significant divergence above the naturally rippled bed compared to the sinusoidal rippled bed is observed within the height of two ripple amplitudes. This difference is most pronounced at the bottom and diminishes with increasing bottom distance, indicating a gentler gradient. For the sinusoidal rippled bed, a maximal concentration occurs under the calm wave scenario. Conversely, above the naturally rippled bed, maximum concentration under the intermediate and the stormy scenario slightly exceeds that

under the calm scenario, steadily increasing. Furthermore, peak concentration values are more than double those observed above the sinusoidal rippled seabed.

Turbulent Kinetic Energy

Profiles of the time- and horizontally averaged in-plane turbulent kinetic energy $\langle\overline{TKE_{xz}}\rangle_x$ are presented in Figure 5.12. Under the calm wave scenario, TKE values above the sinusoidal rippled seabed exhibit a slight enhancement compared to those above the naturally rippled bed. However, this relationship shifts under the intermediate scenario, with TKE above the naturally rippled bed surpassing that above the sinusoidal rippled bed in the lower water column, notably increasing with decreasing bottom distance. This trend becomes more pronounced under the stormy wave scenario: while TKE levels are relatively similar for both beds in the upper water column, the values above the naturally rippled bed notably exceed those above the sinusoidal rippled bed within the bottom distance of two ripple amplitudes. Above the sinusoidal rippled seabed, the TKE profile exhibits a sudden spike at the seabed interface, whereas, above the naturally rippled bed, the profile shows a bulge, peaking at about half a ripple amplitude above the ground, particularly evident under the stormy wave scenario.
The phase-resolved TKE maps depicted in Figure 5.13 reveal, that TKE levels at the downstream slope of the naturally shaped ripple are considerably higher than those behind the sinusoidal ripple. A trail of significantly enhanced TKE initially follows the ripple contour for half a ripple wavelength and then extends up to two ripple amplitudes above the trough in phases (a) and (c). In phase (b), a region of high TKE is located within the depression behind the ripple crest and in the centre of the recirculation zone of the flow field. The centre of the recirculation zone behind the sinusoidal rippled bed is located much closer to the bottom surface than the centre of the recirculation zone behind the naturally rippled bed. Examining selected vertical velocity profiles illustrated along the ripple contour in Figure 5.14, it is evident that the flow separates earlier at the downstream slope of the naturally rippled seabed. This results in a significantly wider and thicker recirculation zone, correlating with markedly enhanced TKE values.

Vertical Turbulent Fluxes

Figure 5.15 depicts profiles of the time- and horizontally averaged vertical turbulent flux of the tracer fluid $\langle\overline{w'c'}\rangle_x$ above the sinusoidal and the naturally rippled seabed under all three wave scenarios. Under the calm wave conditions, the turbulent flux above the sinusoidal rippled bed slightly exceeds that above the other bed, with differences being small. However, under both other scenarios, turbulent flux above the naturally rippled bed is increased compared to that above the sinusoidal rippled bed. This deviation is especially notable within the first two ripple amplitudes or 40 mm above the bottom, where the flux profiles above the naturally rippled bed are distinctly bulged. Under the intermediate wave scenario the flux peaks at approximately 5 mm bottom distance, corresponding to 0.25 ripple amplitudes, while under the stormy wave scenario, the peak shifts to 20 mm, corresponding to 1 ripple amplitude. Upon examination of the phase-resolved maps of the

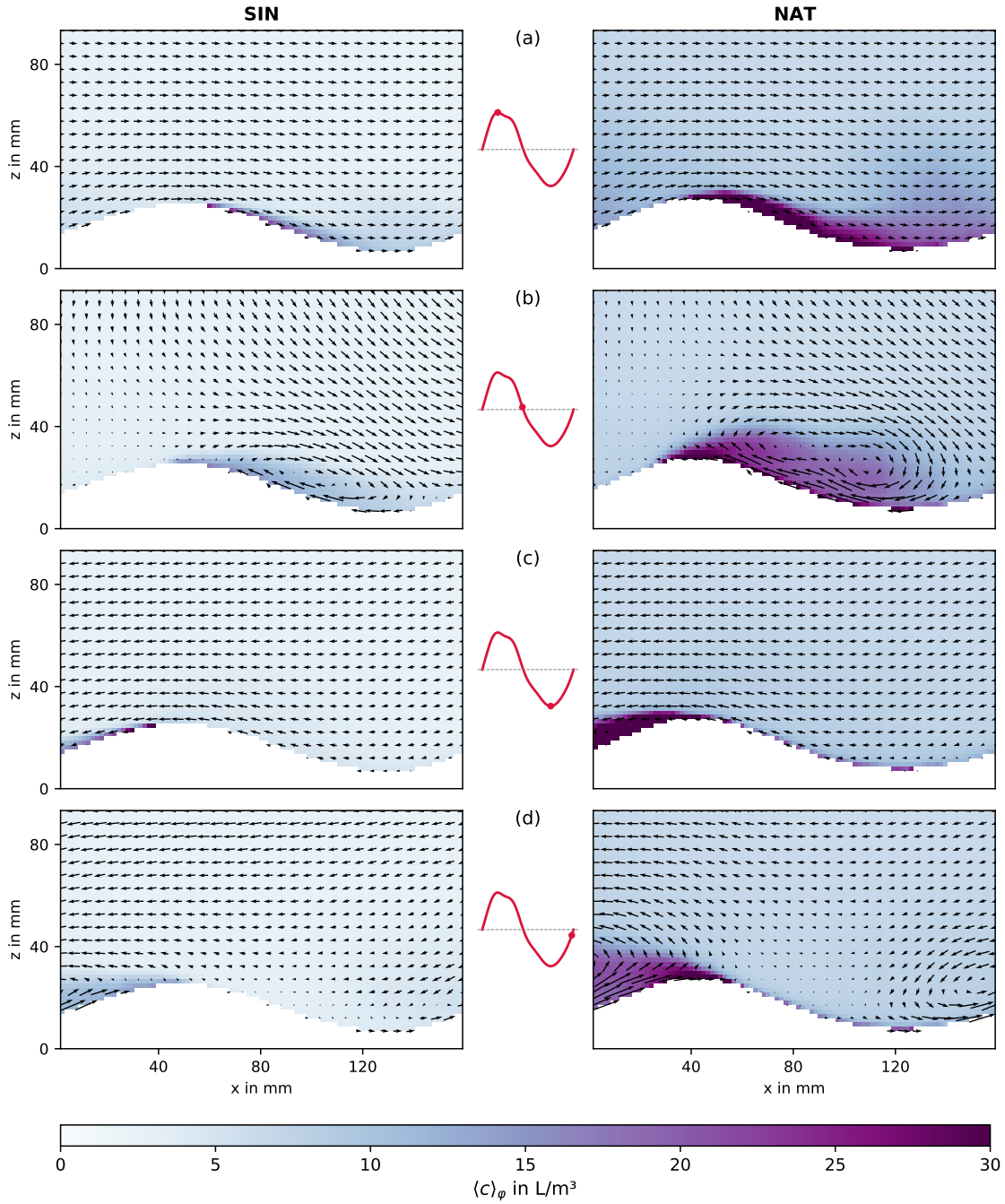

Figure 5.10: Tracer fluid distribution $\langle c \rangle_\varphi$ and velocity fields $\langle \mathbf{u} \rangle_\varphi$ for specific phases of the wave cycle under the stormy wave scenario above both the sinusoidal rippled seabed (left) and the naturally rippled seabed (right). The middle column plot indicates the corresponding phase's position within the wave cycle. The absolute concentration was normalised with the dye concentration $c_{\mathrm{R6G,\ Tracer}}$ of the injected tracer fluid.

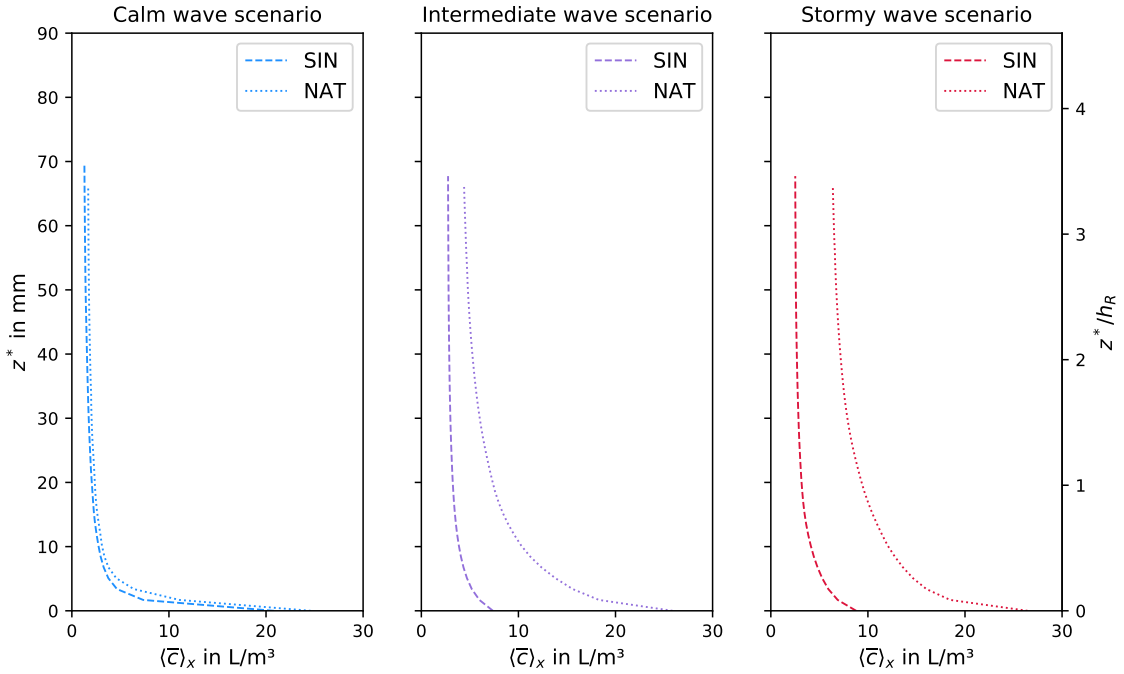

Figure 5.11: Time- and horizontally averaged tracer fluid concentration $\langle\overline{c}\rangle_x$ dependent on the bottom distance z^* above the sinusoidal and the naturally rippled seabed under the calm (left), the intermediate (middle) and the stormy (right) wave scenario. On the right y-axis, the bottom distance was normalised with the ripple height h_R.

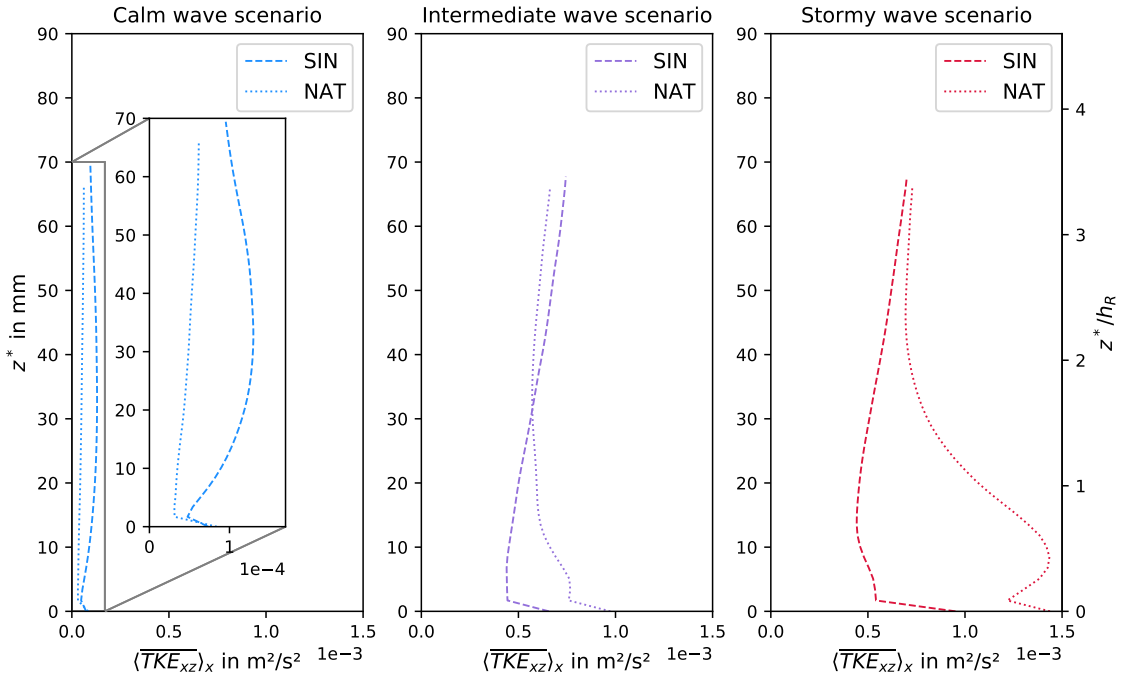

Figure 5.12: Time- and horizontally averaged in-plane turbulent kinetic energy $\langle\overline{TKE_{xz}}\rangle_x$ dependent on the bottom distance z^* above the sinusoidal and the naturally rippled seabed under the calm (left), the intermediate (middle) and the stormy (right) wave scenario. On the right y-axis, the bottom distance was normalised with the ripple height h_R.

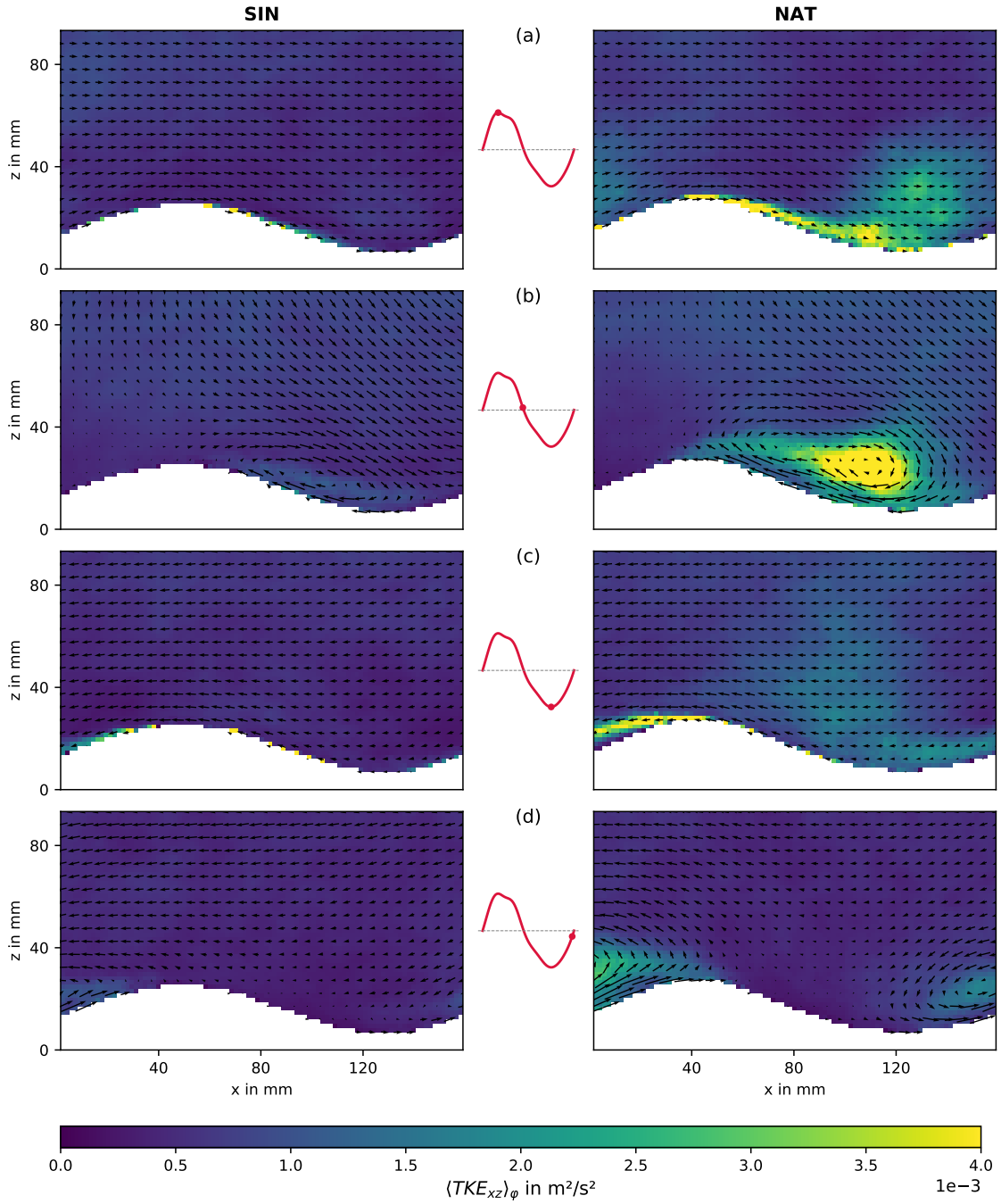

Figure 5.13: Phase averaged in-plane turbulent kinetic energy $\langle TKE_{xz} \rangle_\varphi$ and velocity fields $\langle \mathbf{u} \rangle_\varphi$ for specific phases of the wave cycle under the stormy wave scenario above the sinusoidal (left) and the naturally rippled seabed (right). The middle column plot indicates the corresponding phase's position within the wave cycle.

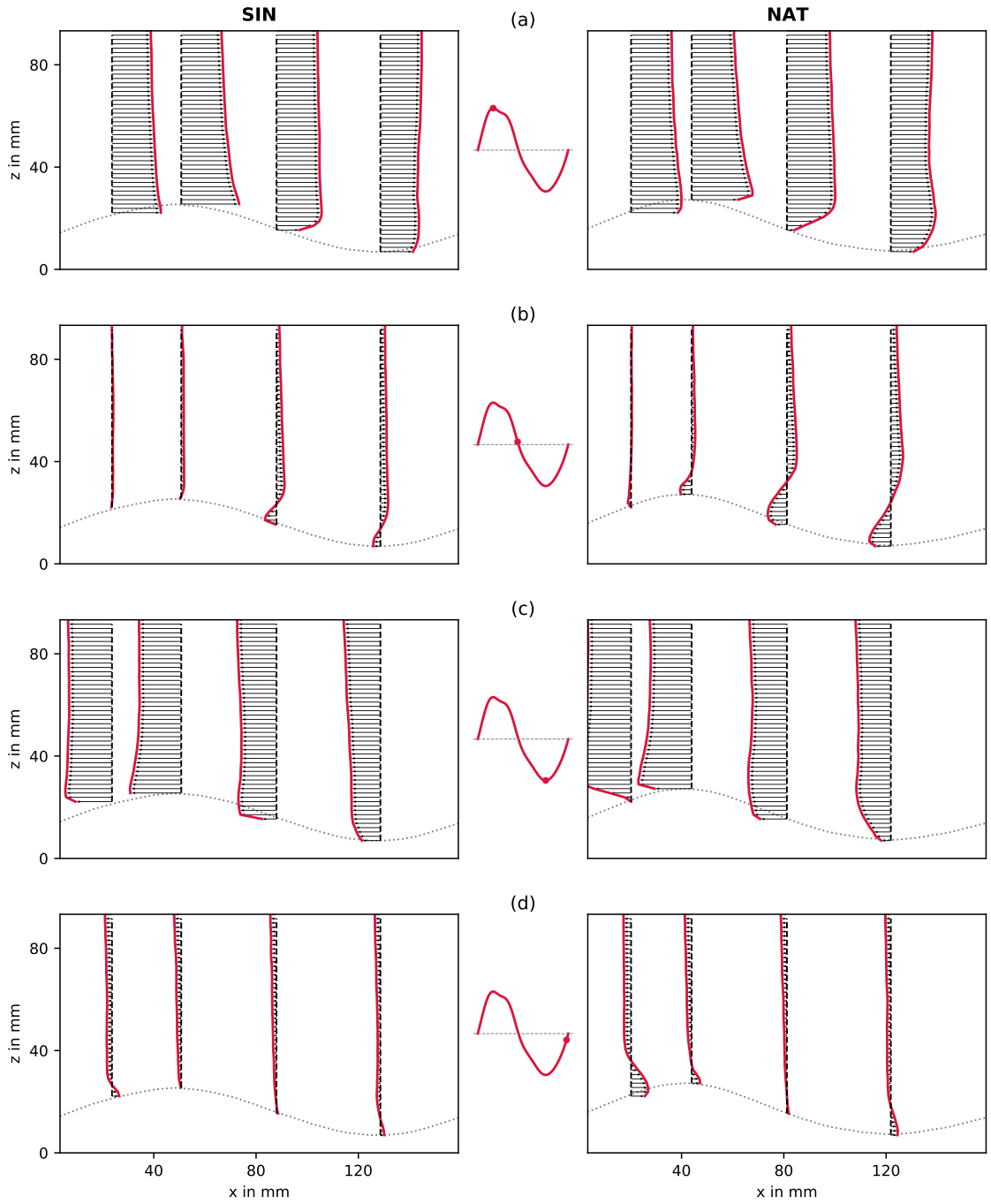

Figure 5.14: Phase averaged horizontal velocity profiles for specific phases of the wave cycle under the stormy wave scenario above the sinusoidal rippled (left) and the naturally rippled (right) seabed. The middle column plot indicates the corresponding phase's position within the wave cycle

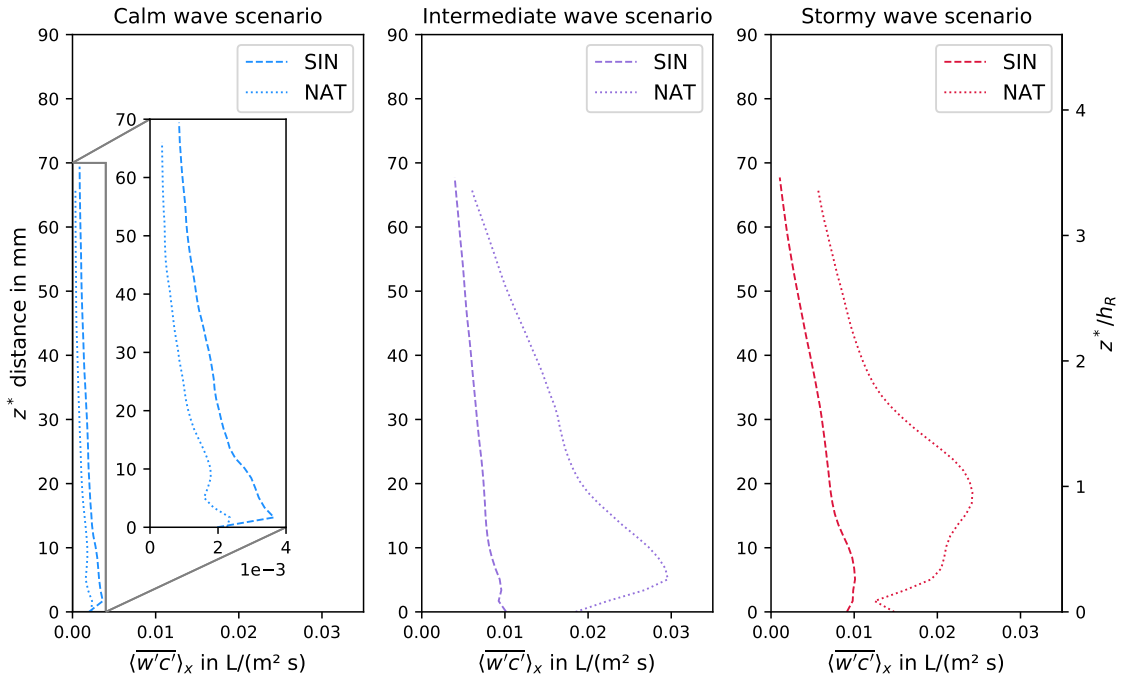

Figure 5.15: Time- and horizontally averaged vertical turbulent flux of the tracer fluid $\langle\overline{w'c'}\rangle_x$ dependent on the bottom distance z^* above the sinusoidal and the naturally rippled seabed under the calm (left), the intermediate (middle) and the stormy (right) wave scenario. On the right y-axis, the bottom distance was normalised with the ripple height h_R.

vertical turbulent flux under the intermediate scenario above both beds, as illustrated in Figure A.2 and Figure A.3, to be found in the appendix, discernible differences emerge in the pattern of high fluxes above the naturally rippled bed compared to those above the sinusoidal rippled bed. Above the latter, regions of high turbulent flux are attached to the seabed surface and regions of negative flux are barely visible, whereas, above the naturally rippled bed, regions of high turbulent flux separate from the seabed surface and regions of negative turbulent flux appear underneath.

Figure 5.16 illustrates the respective maps under the stormy wave scenario, where regions of positive vertical flux are considerably larger and higher in magnitude than under the intermediate wave scenario. Above the naturally rippled bed, the magnitudes of the vertical turbulent flux are even higher and the areas of enhanced flux are larger than above the sinusoidal rippled bed. Spatially, there is a distinct enhancement of turbulent flux at the interface of the downstream slope above both beds, forming a larger cloud that spans up to two ripple amplitudes above the trough in the second half of the ripple depression. Additionally, at the left edge of the FoV, the influence of the next ripple outside the left boundary is observable. In phase (b) an oval-shaped recirculation zone within the flow field corresponds to a region of concentrated positive fluxes. However, this region is flatter above the sinusoidal rippled bed. Phases (c) and (d) exhibit similar, but inverted, patterns. Furthermore, layers of negative flux, which locally indicate downward vertical transport, develop beneath these regions and correlate with flow acceleration along the upstream slope. This phenomenon is particularly distinguishable in phases (b) and (d).

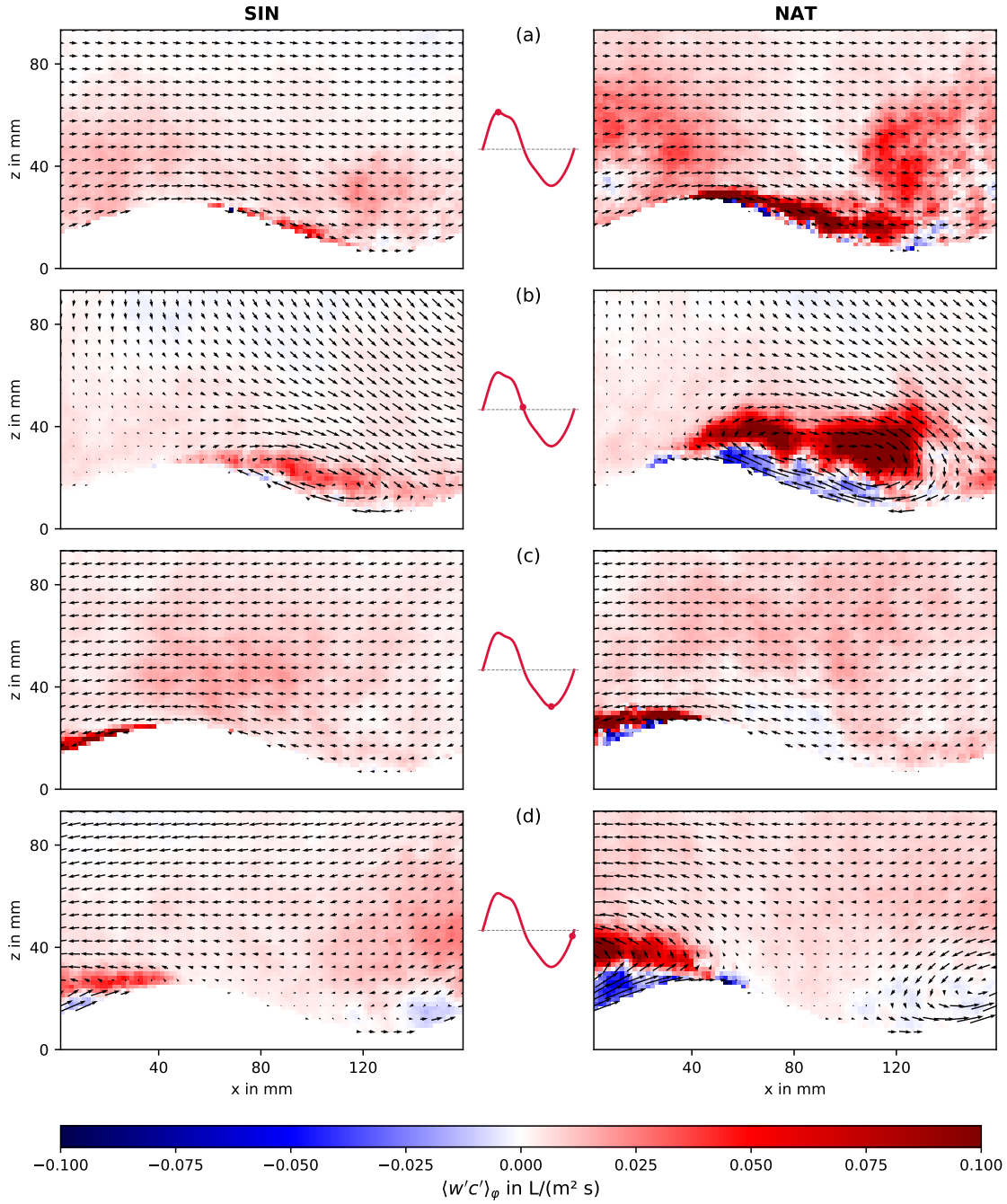

Figure 5.16: Phase averaged vertical turbulent flux $\langle w'c' \rangle_\varphi$ and velocity fields $\langle \mathbf{u} \rangle_\varphi$ for specific phases of the wave cycle under the stormy wave scenario above the sinusoidal (left) and the naturally rippled seabed (right). The middle column plot indicates the corresponding phase's position within the wave cycle.

Summary

The previous exposition demonstrates, that a variation of the ripple shape can profoundly alter discharge and transport processes by influencing the flow conditions. Under the intermediate and stormy wave scenarios, the steeper slope and smaller radius of the naturally rippled bed compared to the sinusoidal rippled bed result in earlier flow separation at the downstream ripple slope. This expands the flow field recirculation zone in width, height, strength, and duration and therefore induces an additional pressure gradient. Consequently, both the pumping of tracer fluid from the permeable seabed and vertical turbulent flux within the water column are profoundly amplified, with peak turbulent flux values reaching up to three times those above the sinusoidal rippled bed. Overall, this results in markedly elevated values of tracer fluid concentration throughout the whole water column above the naturally rippled bed under the intermediate and the stormy wave scenario.

5.4 Comparison of Turbulent Transport Above the Symmetric and the Asymmetric Naturally Rippled Seabed Model

This section contrasts the profiles of the time- and horizontally averaged tracer fluid concentration, TKE_{xz}, and vertical turbulent flux acquired above both the symmetric and asymmetric naturally rippled seabed models. These findings will be additionally supported by chosen phase-resolved results, highlighting the observed effects.

Tracer Fluid Distribution

Figure 5.17 presents profiles of the time- and horizontally averaged tracer fluid concentration $\langle \overline{c} \rangle_x$ over both the symmetric and the asymmetric naturally rippled seabed. Under calm wave conditions, concentration values above the asymmetric bed slightly exceed those above the symmetric bed, except within the first 5 mm of bottom distance. Notably, in close proximity to the seabed interface, the peak concentration above the asymmetric bed only reaches a quarter of that above the symmetric rippled bed. However, under the intermediate and stormy wave scenarios, the maximum concentration is even lower, representing only a fraction of the maximum value above the symmetric rippled bed. Examining phase-resolved spatial tracer fluid distribution under the stormy wave scenario, as depicted in Figure 5.18, reveals that much higher tracer fluid concentrations were measured above the symmetric rippled bed, than above the asymmetric rippled bed. Note, that the colour bar in Figure 5.18 is scaled by a factor of five. Above the latter, enhanced values at the gentle upstream slope of the asymmetric seabed profile can be observed during the phase of maximum vertical velocity, phase (a). As the wave's direction reverses in phase (b), a cloud of slightly heightened tracer fluid concentration can be observed in the lee side wake of the ripple, corresponding to the recirculation zone in the velocity field separating at the steep slope of the ripple. In phase (c), when the reference velocity $\langle u_{top} \rangle_\varphi$ reaches its maximum negative value, and accordingly the flow field has changed its direction completely, a small and highly concentrated cloud of tracer fluid is expelled at the ripple crest and follows the gentle ripple slope. A diffused tracer fluid cloud, that might either be expelled at the next ripple crest outside the right edge of the FoV or be a remnant from the previous wave phases is visible in the upstream part of the FoV. Finally, in phase (d), only a small and flat-shaped recirculation zone in the velocity field is observable, corresponding to a region of enhanced tracer fluid concentration.

Turbulent Kinetic Energy

The profiles of the time- and horizontally averaged in-plane turbulent kinetic energy $\langle \overline{TKE_{xz}} \rangle_x$ above both the symmetric and the asymmetric naturally rippled seabed, as presented in Figure 5.19, exhibit strong similarity across all wave scenarios. The highest peak value and the most distinct bulge are observed under the stormy wave scenario at approximately 0.5 ripple amplitudes above the bottom. Figure 5.20 illustrates the

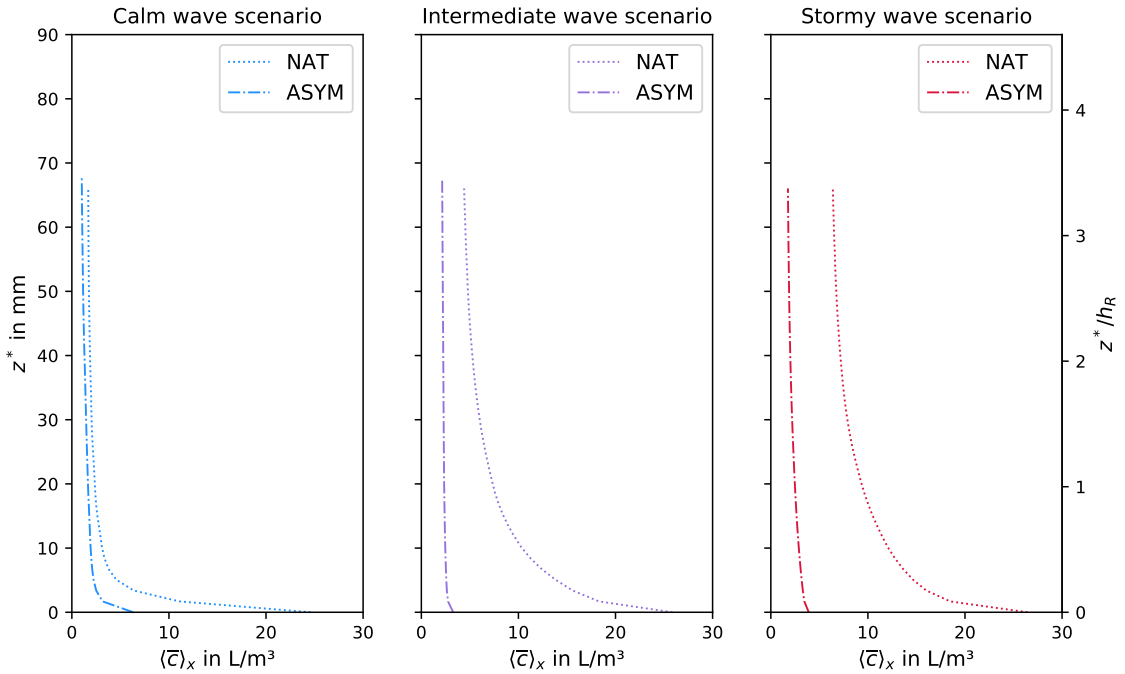

Figure 5.17: Time- and horizontally averaged tracer fluid concentration $\langle\overline{c}\rangle_x$ dependent on the bottom distance z^* above the symmetric and the asymmetric naturally rippled seabed under the calm (left), the intermediate (middle) and the stormy (right) wave scenario. On the right y-axis, the bottom distance was normalised with the ripple height h_R.

phase-resolved TKE above both beds under the stormy wave scenario, where profound differences can be noted. In phase (a), a region of enhanced TKE above the asymmetric rippled bed is concentrated directly at the steep downstream slope. Above the symmetric seabed, the corresponding region of heightened TKE is attached to the downstream slope until it reaches the ripple trough, where it extends up to approximately two ripple amplitudes in height, albeit decreasing in magnitude. In phase (b), flow separation occurs at the downstream slope forming recirculation zones in the flow field corresponding to high magnitudes in TKE. Above the asymmetric bed, the recirculation zone forming at the steep slope of the ripple exhibits a rounder shape and extends across a larger region than above the symmetric bed. While phases (c) and (d) display similar but mirrored patterns of enhanced TKE as phases (a) and (b) in the case of the symmetric seabed, significant differences are found in the case of the asymmetric seabed. In phase (c), the region of enhanced TKE at the downstream slope is small and attached to the surface of the gentle ripple slope. In phase (d), a small recirculation zone can be discerned at the gentle ripple slope, albeit with low magnitudes in velocity and TKE.

These observations can be supplemented with selected vertical velocity profiles illustrated along the ripple contour in Figure 5.22. In phase (a), flow acceleration near the seabed compared to the far-field velocity occurs at the ripple crest. Flow separation at position (II) is observed on the steep slope of the asymmetric rippled bed, whereas the flow remains attached to the symmetric rippled bed at the corresponding position (I). In phase (b), a recirculation zone spanning the downstream slope is noted above both beds, exhibiting similar magnitudes of reverse flow at positions (III) and (IV). In phase (c), flow separation

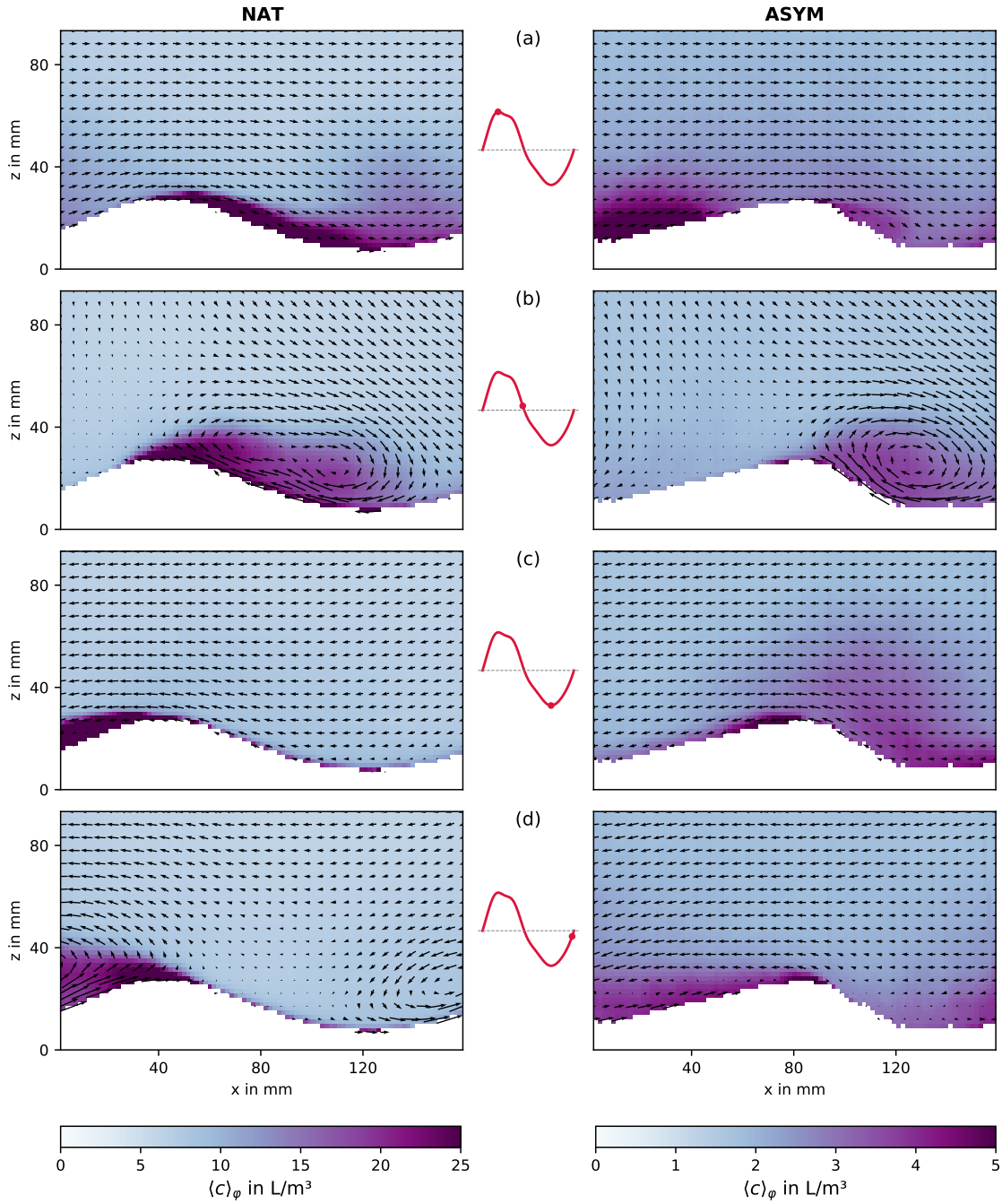

Figure 5.18: Tracer fluid distribution $\langle c \rangle_\varphi$ and velocity fields $\langle \mathbf{u} \rangle_\varphi$ for specific phases of the wave cycle under the stormy wave scenario above the symmetric (left) and the asymmetric (right) naturally rippled seabed. The middle column plot indicates the corresponding phase's position within the wave cycle. The absolute concentration was normalised with the dye concentration $c_{\mathrm{R6G,\ Tracer}}$ of the injected tracer fluid. Note, that the left colour bar is scaled by a factor of five.

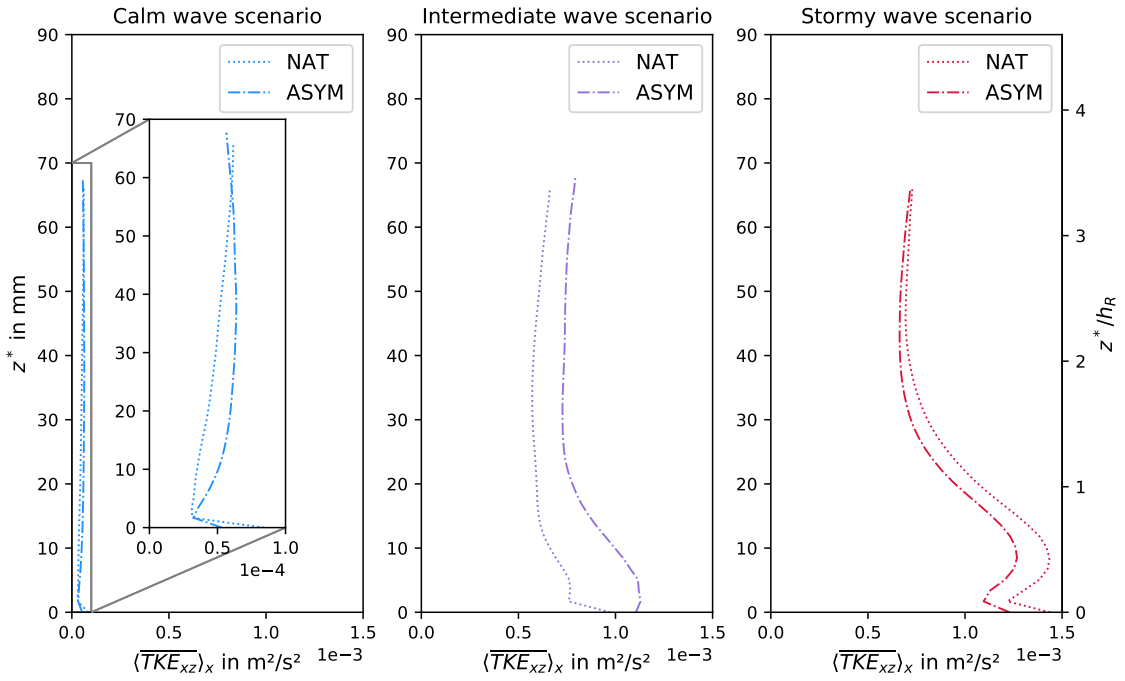

Figure 5.19: Time- and horizontally averaged in-plane turbulent kinetic energy $\langle\overline{TKE_{xz}}\rangle_x$ dependent on the bottom distance z^* above the symmetric and the asymmetric naturally rippled seabed under the calm (left), the intermediate (middle) and the stormy (right) wave scenario. On the right y-axis, the bottom distance was normalised with the ripple height h_R.

initiates on the downstream slope of the symmetric rippled bed at position (V), while the flow remains well attached to the gentle slope of the asymmetric rippled bed at the corresponding position (VI). In phase (d), the recirculation zone at the downstream slope of the symmetric rippled bed at position (VII) mirrors the pattern observed in phase (b) at position (III). However, above the asymmetric rippled bed, the recirculation zone on the downstream slope is significantly smaller than in phase (b), as evident from the point of zero velocity in the velocity profile being closer to the seabed surface and the lower magnitudes of reverse flow at position (VIII).

Vertical Turbulent Fluxes

Figure 5.22 displays the profiles of time- and horizontally averaged vertical turbulent flux of the tracer fluid $\langle\overline{w'c'}\rangle_x$ above both, the symmetric and the asymmetric naturally rippled bed under all three wave scenarios. Under the calm wave scenario, the fluxes above both beds are similar across the whole height of the FoV. Under the intermediate and the stormy scenario, however, the turbulent fluxes above the asymmetric bed are significantly lower than above the symmetric bed. The phase-resolved vertical turbulent fluxes occurring under the stormy wave scenario, illustrated in Figure 5.23, reveal a significant dependency on the phase of the wave cycle concerning the occurrence of high magnitudes in turbulent flux above both seabeds. While phases (a) and (c), as well as phases (b) and (d), exhibit similar but mirrored patterns for the symmetric bed, the asymmetric bed induces asymmetric effects. Under the calm scenario, see Figure A.4, to be found in the appendix, the

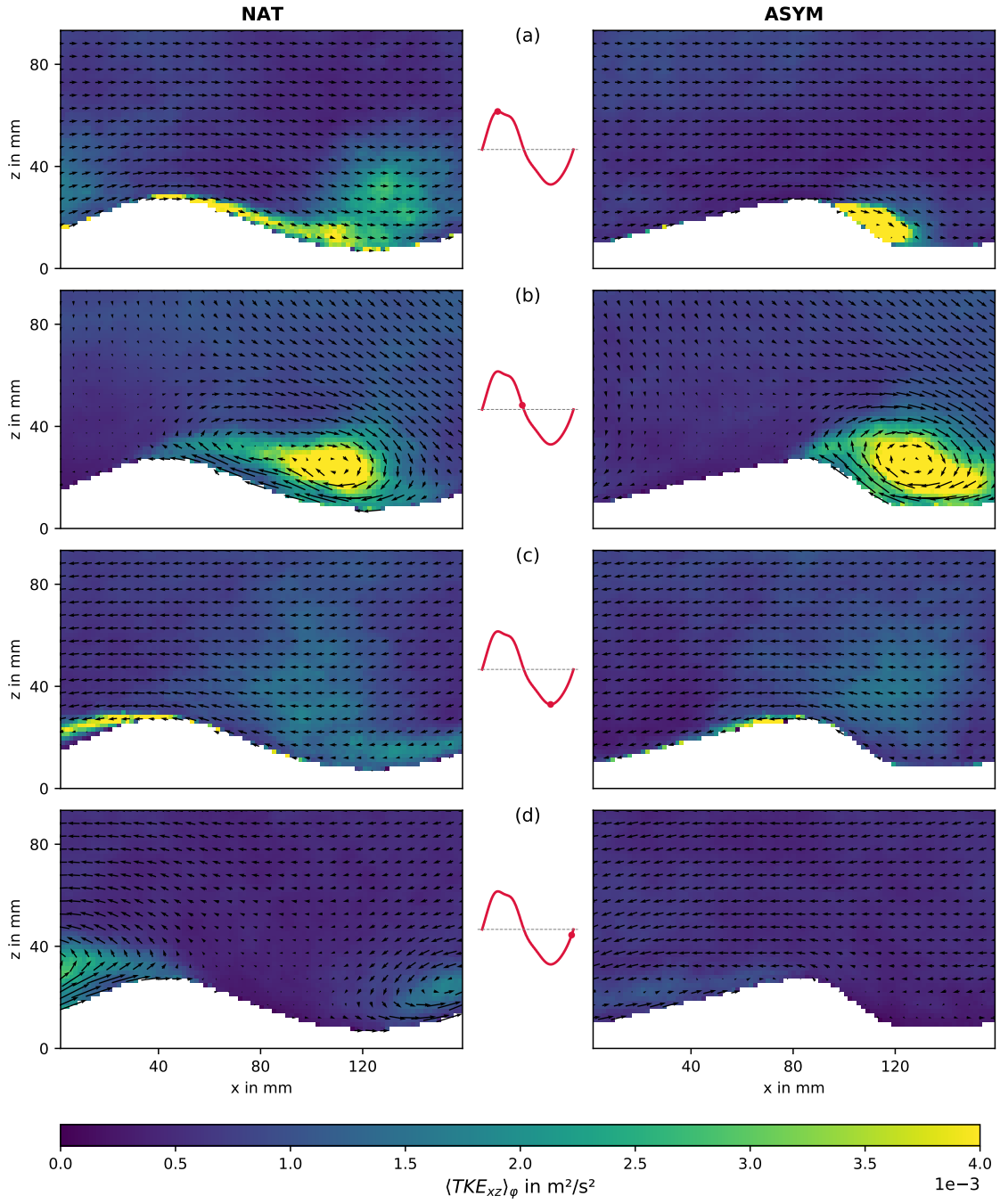

Figure 5.20: Phase averaged in-plane turbulent kinetic energy $\langle TKE_{xz} \rangle_\varphi$ and velocity fields $\langle \mathbf{u} \rangle_\varphi$ for specific phases of the wave cycle under the stormy wave scenario above the symmetric (left) and the asymmetric (right) naturally rippled seabed. The middle column plot indicates the corresponding phase's position within the wave cycle.

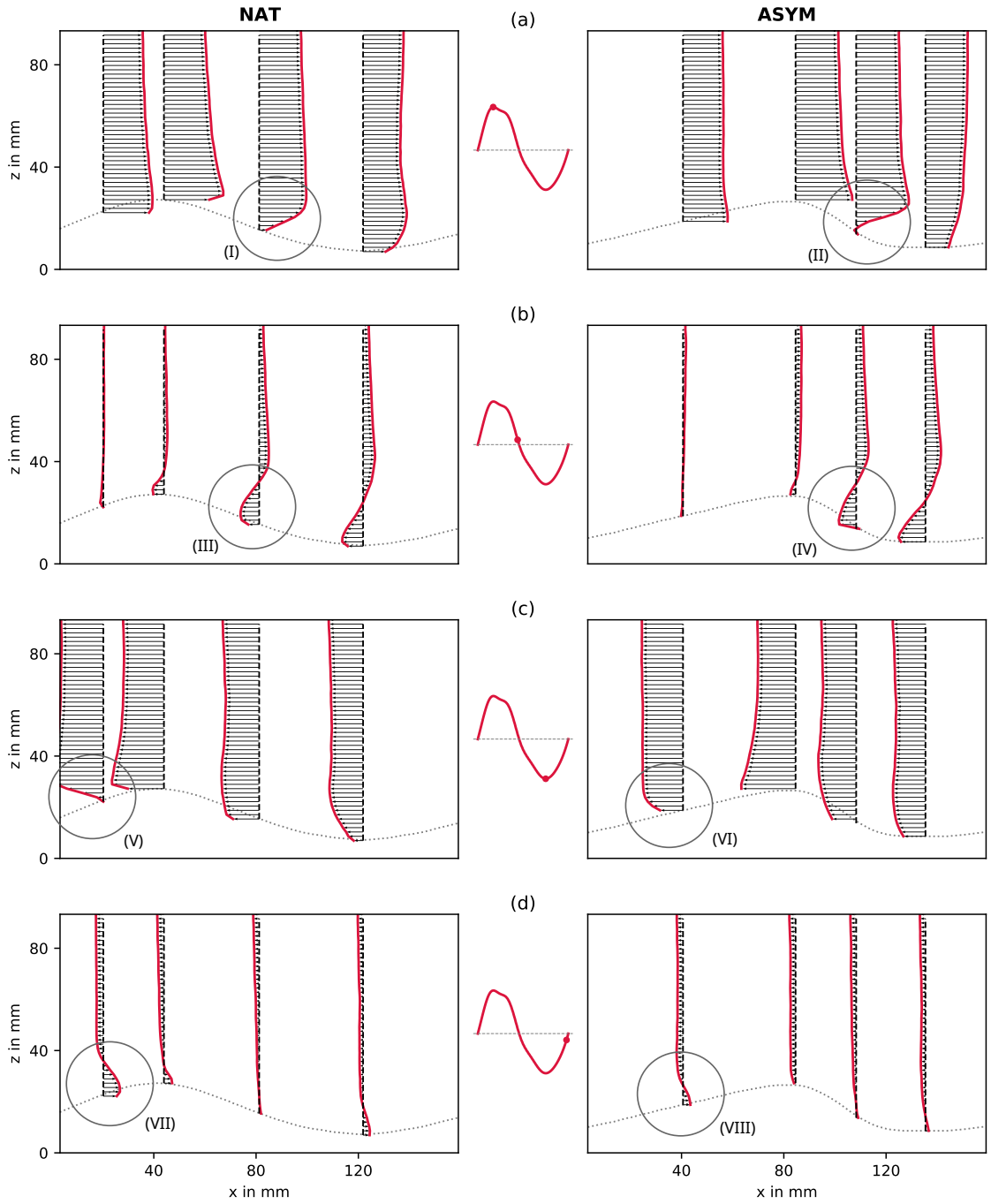

Figure 5.21: Phase averaged horizontal velocity profiles for specific phases of the wave cycle under the stormy wave scenario above the symmetric (left) and the asymmetric (right) naturally rippled seabed. The middle column plot indicates the corresponding phase's position within the wave cycle

highest fluxes occur at the gentle ripple slope. The magnitude is generally small (note, that the colour bar in Figure A.4 is scaled by a factor of five) and the flow is attached to the bottom surface throughout the whole wave cycle. Under the stormy wave scenario, a region of enhanced vertical flux develops at the steep ripple slope during phase (a), where the flow initiates separation from the bottom surface. This region is less concentrated than in phase (c), where only a very small but strong vertical flux occurs just behind the ripple crest at the gentle slope of the ripple, while the flow remains attached during this phase of the wave cycle. The differences are even more pronounced during wave inflection phases: In phase (b) a large recirculation zone forms in the wake of the steep lee side of the ripple, corresponding to an area of high magnitudes in turbulence-induced flux, approximately five times higher than in the absence of separation in the calm scenario. The peak of $\langle w'c' \rangle_\varphi$ is reached where the overflow of the ripple crest encounters the ascending recirculation zone. Remnants of this region of significantly heightened turbulent flux are still visible in phase (c). However, in phase (d), only a very flat-shaped, recirculation zone with low magnitudes in velocity forms at the gentle ripple slope, corresponding to slightly enhanced values of vertical turbulent flux.
In the horizontal averaging over the entire wave period, see Figure 5.22, lower values result for this reason: While the mutual high flux values on the lee side of the ripples over the symmetric bed accumulate twice per wave period, the average over the asymmetric bed is only increased by the strong turbulent flux occurring once per wave period behind the steep ripple side. Additionally, generally larger magnitudes of vertical turbulent flux were determined over the symmetrically rippled bed, as the shape and extent of the recirculation zone seem to promote tracer fluid discharge and transport significantly more than in the case of the asymmetric bed.

Summary

The previously presented findings illustrate that the asymmetry of the investigated seabed model fundamentally affects the process of tracer fluid discharge and vertical turbulent flux. So far, regarding the symmetric seabed models (FLAT, SIN, NAT), phases (a) and (c) as well as phases (b) and (d) showed very similar but mirrored patterns concerning flow field, tracer fluid distribution, turbulence, and turbulent flux. However, the asymmetric bed certainly causes asymmetric effects under the intermediate and the stormy scenario. At the gentle slope, less flow acceleration (upstream) and later flow separation (downstream) were observed, which in turn decreases pressure gradients forcing tracer fluid out of the permeable seabed. At the steep slope, strong pressure gradients due to flow acceleration (upstream) and flow field recirculation (downstream) occur, inducing tracer fluid discharge. However, these effects seem to compensate for each other with regard to turbulent transport: When high concentration values are available, low flow field fluctuations will constrain a pronounced turbulent vertical flux. On the other hand, when early flow separation at the steep ripple slope enables strong flow field fluctuations, a pronounced turbulent flux is prevented by low concentration fluctuations due to moderate local tracer fluid output. Phase-specifically, TKE is high in phases of flow separation at the steep

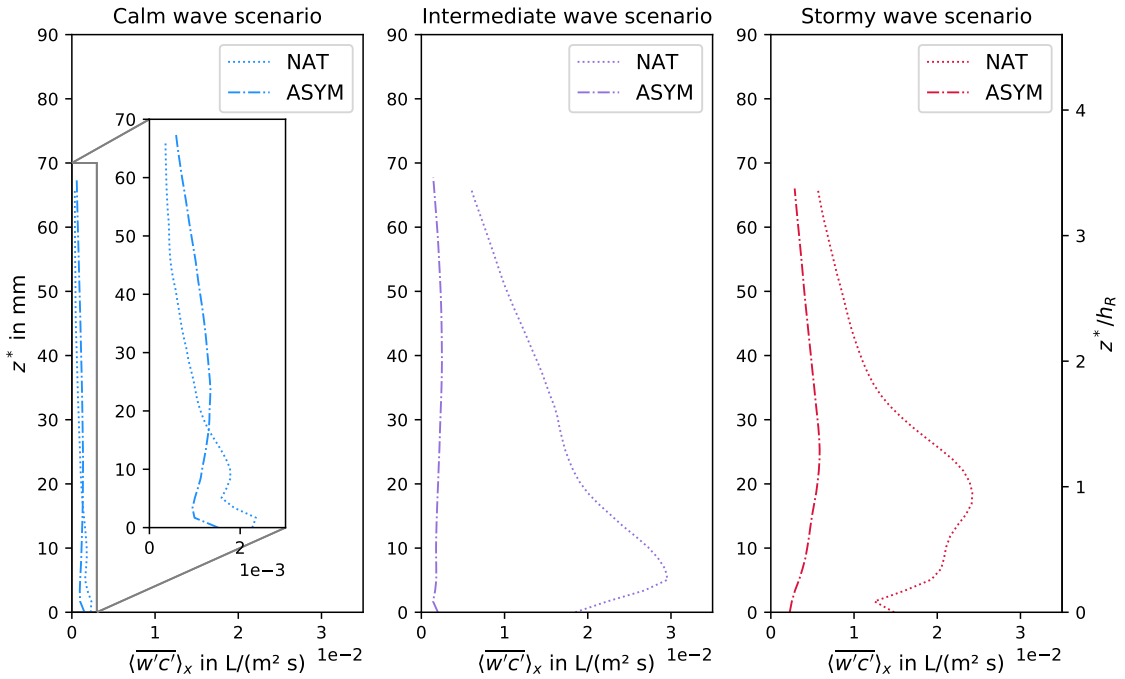

Figure 5.22: Time- and horizontally averaged vertical turbulent flux of the tracer fluid $\langle\overline{w'c'}\rangle_x$ dependent on the bottom distance z^* above the symmetric and the asymmetric naturally rippled seabed under the calm (left), the intermediate (middle) and the stormy (right) wave scenario. On the right y-axis, the bottom distance was normalised with the ripple height h_R.

ripple slope and low in phases, where the gentle part of the ripple acts as the downstream slope. In the profiles of the time- and horizontally averaged TKE, these effects even each other out resulting in curves being very similar to those of the symmetric seabed. Therefore, the capacity of turbulence is equal to the symmetric bed with simultaneously lower local concentration values leading to overall lower magnitudes in vertical turbulent flux. Thus, the transport process is less effective across the surface of the asymmetric bed resulting in lower concentration values throughout the whole water column compared to the symmetric naturally rippled bed.

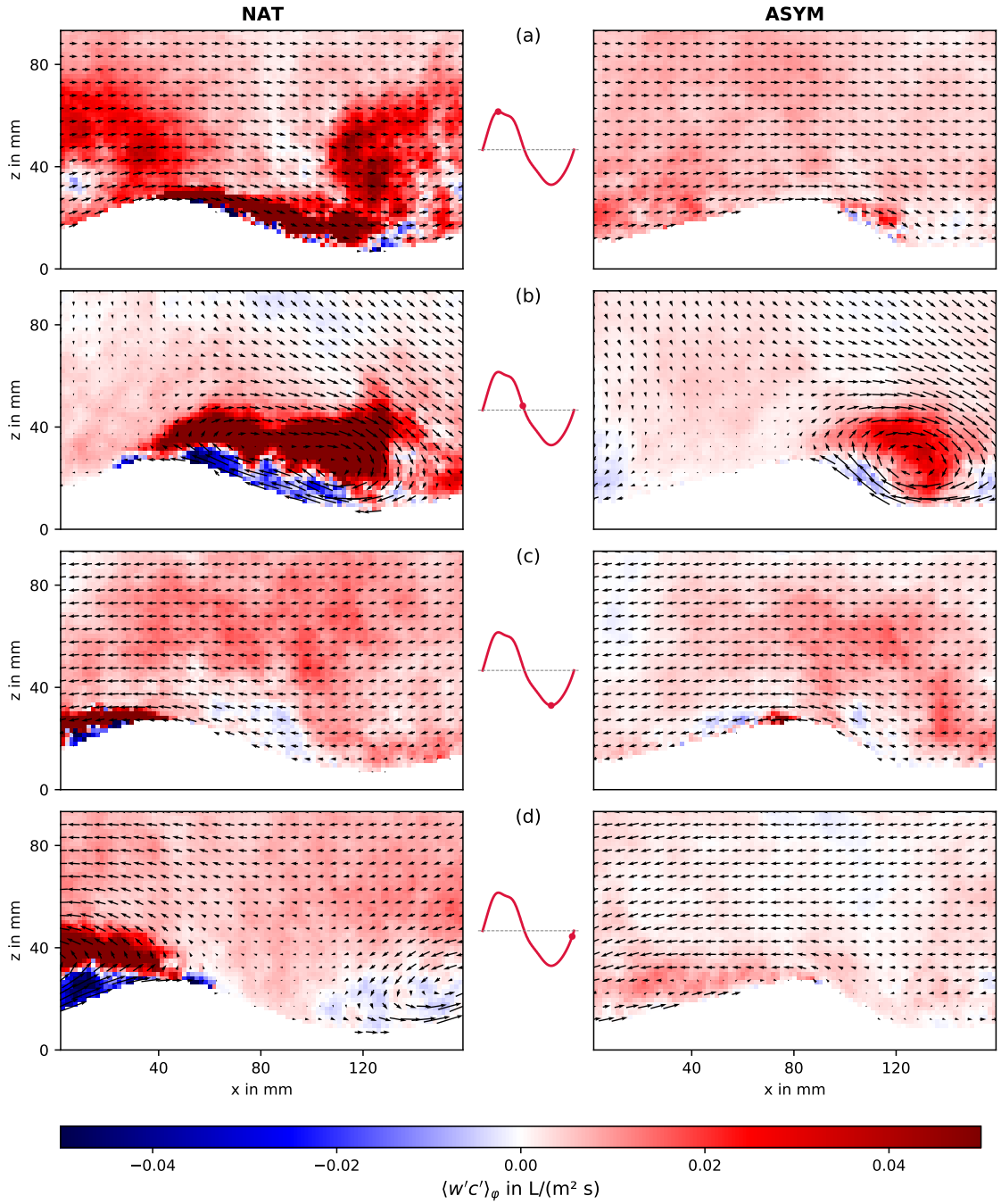

Figure 5.23: Phase averaged vertical turbulent flux $\langle w'c' \rangle_\varphi$ and velocity fields $\langle \mathbf{u} \rangle_\varphi$ for specific phases of the wave cycle under the stormy wave scenario above the symmetric (left) and the asymmetric (right) naturally rippled seabed. The middle column plot indicates the corresponding phase's position within the wave cycle.

5.5 Turbulent Mixing Length

Figure 5.24 presents the turbulent mixing length l_c as a function of the bottom distance z^* calculated using Equations 4.13 and 4.14 above all four seabed models under each of the three wave scenarios. The calculation of l_c depends on three distinct quantities derived from the measurements: the vertical turbulent flux $\langle w'c' \rangle_{\varphi,x}$, the vertical gradient of the concentration $\langle c \rangle_{\varphi,x}$ and the absolute value of the vertical gradient of the horizontal velocity $\langle u \rangle_{\varphi,x}$. Due to this dependency, the results exhibit a certain degree of noise. Outliers become more frequent with increasing distance from the seabed, as the concentration and velocity gradients diminish significantly, as visible in Figures e.g. 5.17 and Figure 5.21.
Above the flat seabed, the curve progression of the mixing length is similar for all wave scenarios. The vertical profile of the mixing length increases steadily up to about 20 mm from the seabed, although not linearly. Above this point, the mixing length value fluctuates around a value of 35 mm to 40 mm after a slight overshoot.
Above the other seabeds, the vertical profile of the mixing length shows a qualitatively similar pattern. Initially, a steady increase in near-bed water layers is visible, followed by an apparent settling around a fixed value, hereafter referred to as far-field mixing length, accompanied by an increase in outliers for the reasons described above. However, the wave scenario has a stronger influence on the mixing length than above the flat seabed, particularly above the sinusoidal rippled and the asymmetric naturally rippled seabed.
Above all rippled seabeds, the mixing length near the seabed - within the first approximately 20 mm or one ripple height h_R of bottom distance -, shows the lowest values under the stormy wave scenario. Additionally, it is predominantly reduced compared to the values occurring above the flat seabed.
Above the symmetric naturally rippled seabed a continuous increase of the mixing length with growing bottom distance is notable up to two ripple heights $\Delta z/h_R = 2$. Under the calm wave scenario, the mixing length continues to rise. In contrast, under the intermediate and stormy wave scenarios, the far-field mixing length stabilizes at around 45 mm to 50 mm.
Above the sinusoidal rippled and asymmetric naturally rippled seabeds, the mixing lengths under the intermediate and stormy wave scenarios significantly exceed those observed under the calm scenario at distances greater than approximately 20 mm or one ripple height h_R from the seabed. Above the sinusoidal rippled seabed, the far-field mixing length stabilizes at around 35 mm under the calm wave scenario and 50 mm under the intermediate and stormy wave scenario. Above the asymmetric naturally rippled seabed, the far-field mixing length stabilizes at around 30 mm under the calm wave scenario and around 80 mm under the intermediate and stormy wave scenario.
Overall, the highest mixing lengths, ranging from 120 mm to 125 mm, were observed above the asymmetric seabed under the intermediate and the stormy wave scenario.

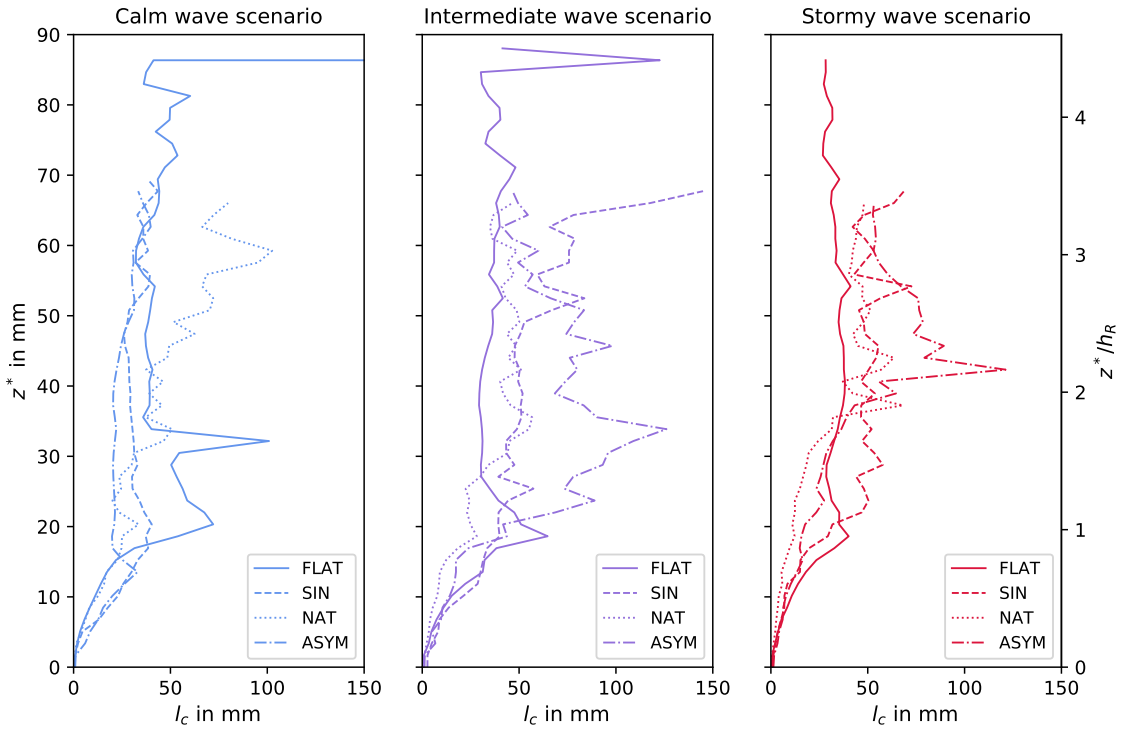

Figure 5.24: Turbulent mixing length l_c as a function of the bottom distance z^* above all four seabed models under the calm (left), the intermediate (middle) and the stormy (right) wave scenario. On the right y-axis, the bottom distance was normalised with the ripple height h_R.

Chapter 6

Discussion

The present work focuses on how seabed topography impacts the vertical transport of fluid emerging from the seabed, with the fluid injected at the bottom of the artificial seabed at a constant volumetric flow rate. The central hypothesis is that the interaction between seabed topography and oscillating flow generates varying degrees of turbulence and that this is the governing factor influencing fluid transport and thereby the resulting local concentration values.

The study investigates three key aspects: the impact of a rippled seabed compared to a flat seabed; the influence of the ripple shape, specifically comparing sinusoidal ripples with naturally shaped ripples that have sharper crests and broader troughs; and the effect of ripple asymmetry versus symmetry on the flow and transport behaviour.

In addition to the influence of the seabed topography, the effect of varying wave conditions was also investigated as a second variable.

To address these research questions, a series of wave tank experiments were conducted to quantify the turbulent transport of a fluorescent tracer fluid emerging from four different permeable seabed models: a flat (FLAT), a sinusoidal rippled (SIN), a symmetric (NAT) and an asymmetric naturally rippled (ASYM) under differing oscillating flow conditions. The seabed models were partially generic (FLAT and SIN) and partially developed based on in-situ microtopography scans (NAT and ASYM), as detailed in Section 4.2.2.

The oscillating flow conditions were derived from driving three different wave scenarios developed by [Karow, 2019] as briefly described in Section 4.2.1. These scenarios differ in terms of period duration T and maximum horizontal orbital velocity $u_{orb,max}$.

The experiments involved simultaneous two-dimensional PIV and LIF measurements within a FoV of 159.22 mm x 93.28 mm just above the seabed-water-interface, as extensively described in Section 4.3. The derived velocity and concentration fields were phase-averaged to compute fluctuation values of the horizontal velocity u, the vertical velocity w, and the concentration c. This allowed for the determination of phase-resolved tracer fluid distribution $\langle c \rangle_\varphi$, in-plane turbulent kinetic energy $\langle TKE_{xz} \rangle_\varphi$ and vertical turbulent flux $\langle w'c' \rangle_\varphi$. Furthermore, the results were averaged over the entire wave cycle and horizontally averaged to obtain time- and horizontally-averaged concentration $\langle \overline{c} \rangle_x$, in-plane turbulent kinetic energy $\langle \overline{TKE_{xz}} \rangle_x$ and vertical turbulent flux $\langle \overline{w'c'} \rangle_x$ profiles depending on the bottom distance z^*. Additionally, profiles of the turbulent mixing length l_c as a function of z^* were derived. The calculation of all these quantities was detailed in Chapter 4.4.

The results of the aforementioned calculations were thoroughly described in Chapter 5, where the observations made above the different seabed models were compared in pairs (FLAT vs. SIN, SIN vs. NAT, and NAT vs. ASYM).

Key Findings and Interpretation

One key observation was that the boundary conditions — seabed topography and wave scenario — not only affect the transport of the emerging tracer fluid within the water column but also fundamentally influence the discharge process from the permeable seabed, specifically affecting the location, extent, and tracer fluid concentration of the outflow. Under the calm wave scenario, the tracer fluid predominantly emerges uniformly from all seabeds. In contrast, under the intermediate and the stormy wave scenario, characterised by higher maximum flow velocities and longer periods, the tracer discharge from the rippled seabeds exhibits significant spatial and temporal variability: highly concentrated tracer fluid emerges at the ripple crest and the downstream slope corresponding to the respective wave phase.

The observation of focused fluid discharge at the ripple crests aligns with findings by [Huettel et al., 1996] or [Precht and Huettel, 2004], who documented fluid inflow at the ripple troughs and fluid outflow from deeper sediment layers at ripple crests under unidirectional and oscillating flow conditions. According to [Huettel et al., 1996], this focused discharge is explained by the Bernoulli principle: flow obstruction by sediment surface structures increases the local pressure on the upstream slopes, while the pressure drops as the flow accelerates over the elevated features. Similarly, [van der Werf et al., 2007] and [Hare et al., 2014], among others, demonstrated that flow accelerates up the stoss side of ripples and decelerates on the lee side, with intensified flow occurring over the crest. Following [Huettel and Gust, 1992], the resulting horizontal pressure gradients drive fluid exchange across the sediment-water interface in sediments with permeabilities greater than $K > 2 \cdot 10^{-11}$ m^2, which is consistent with the seabed model's permeability of $K = 5.80 \cdot 10^{-10}$ m^2. However, in the present study, focused discharge was only observed under the intermediate and stormy wave scenarios. Although flow acceleration relative to the far-field velocity $\langle u_{top} \rangle_{\varphi}$ as the flow passed over the artificial ripples was observed for all wave scenarios, the calm scenario did not produce the same discharge pattern.

This suggests that a threshold in the pressure gradient may need to be surpassed to significantly alter the discharge characteristics under the experimental conditions, which was not the case under the calm wave scenario. Alternatively, a flow feature specific to the intermediate and the stormy wave scenario might more critically influence the discharge pattern. Under both of these scenarios, regions of high tracer concentration near the sediment-water interface, indicating strong local output, closely corresponded with areas of high TKE. These are associated with flow separation and vortex formation at the downstream slope of the ripples, as will be explained in more detail later in the text.

The aspect of unevenly emerging tracer fluid must be considered when analysing turbulent fluxes in the following, as they could only be detected where measurable amounts of tracer fluid were locally present. By definition, the magnitude of turbulent flux depends on concentration fluctuations, which in turn depend on the local presence and distribution of tracer fluid. Thus, turbulent flux is governed not only by velocity fluctuations due to turbulence but also by the spatial and temporal variations in tracer discharge, shaped by the interaction between wave dynamics and seabed topography. This relationship

determines where and when significant fluxes occur, highlighting the critical role of both wave conditions and seabed topography in driving the transport process.

Impact of the Wave Scenario

Another general finding was that the results obtained under the intermediate wave scenario closely resembled those from the stormy scenario. The maximum far-field velocities $\langle u_{top} \rangle_{\varphi}$ determined in this study differed by less than 0.05 m/s, which does not align with the value of $u_{orb,max}$ documented by [Karow, 2019], see Sections 4.2.1 and 5.1. In contrast, the period $T = 2.52$ s lies near the average of the periods $T = 1.99$ s for the calm wave scenario and $T = 3.28$ s for the stormy wave scenario. However, the intermediate scenario produced similar outcomes as the stormy wave scenario, albeit with slightly less pronounced effects in some instances. Therefore, the intermediate scenario does not represent an average between the calm and stormy conditions but rather a precursor to the latter.

Furthermore, when comparing overall results from the calm wave scenario to those from the stormy wave scenario, the differences were far more pronounced than the variations caused by differing seabed topography.
Under the calm wave scenario, a larger quantity of tracer fluid accumulates in the water layer directly above the seabed compared to the other scenarios. With less tracer fluid being transported to the upper water layers, this results in the highest time-averaged local concentration values and the strongest vertical concentration gradients. The exception is the concentrations measured above the symmetric naturally rippled seabed under the intermediate and stormy wave scenarios, where similarly high time-averaged concentrations were measured. However, these two cases exhibit considerably lower vertical gradients, meaning a smoother transition from low to high concentration values towards the seabed surface, as concentration values at the top edge of the FoV remain remarkably high. This suggests significantly enhanced tracer transport to upper water levels.
Moreover, under the calm wave scenario, the flow remains attached to the seabed surface throughout the entire wave cycle above all seabed models. Notably, this is even the case at the steep downstream slope of the asymmetric seabed, featuring the remarkable RSI of $RSI = 3$. Magnitudes of TKE and vertical turbulent flux are moderate, with the highest local values occurring at or near the bottom.
Under the intermediate and the stormy wave scenario, the spatial distribution of tracer, TKE, and vertical turbulent flux was found to be highly dependent on the wave phase, a relationship only revealed through phase- and spatially-resolved analyses. This effect was significantly more pronounced for the rippled seabed models than for the flat seabed model, as flow separation occurs in the ripple's wake under certain conditions, fundamentally altering the flow field and, consequently, the transport process.

Impact of a Rippled Seabed

The comparison of the experimental outcomes above the flat vs. the sinusoidal rippled sea bed, see 5.2, under the stormy wave scenario yields the following observations, which can be broadly applied to all rippled seabed models.
The high spatial and phase-dependent variability of the measured tracer concentration above the rippled seabeds is assumed to arise from the two main factors. First, as mentioned above, the seabed's structured surface alters the tracer fluid's discharge characteristics. As the flow interacts with the ripple, it promotes the focused release of tracer fluid from the permeable seabed at the ripple's crest and respective downstream slope. In the case that flow separation occurs during the wave cycle, a recirculation zone forms on the downstream side of the ripple, which is assumed to further facilitate the localised discharge of the tracer fluid, as the low-pressure region at the separation points extends to where the flow reattaches.
Second, turbulence plays a crucial role in determining local concentration. The presence of turbulence enables the movement of tracer fluid in the water column through turbulent transport, which can dilute the tracer fluid with the surrounding water.
The high spatial and phase-dependent variability of the measured TKE is also attributed to two factors. Firstly, high velocities reached at approximately one-quarter and three-quarters through the wave cycle contribute to increased shear stresses at the seabed, leading to the formation of Kelvin-Helmholtz instabilities, which in turn cause velocity fluctuations. Secondly, the presence of alternating recirculation zones generates significant velocity variations due to vortex formation.
The presence of high concentration values and, consequently, the potential for substantial concentration fluctuations, combined with significant variations in vertical velocity, results in increased vertical turbulent flux. This flux serves as a metric for quantifying vertical turbulent transport. Consequently, concentration and vertical transport are interdependent, influencing one another.

Flow separation dominates the velocity field above rippled seabeds, generating a recirculation zone, which is well-documented in the literature as "recirculating cell" [Ruggeri et al., 2020], "separation bubble or lee vortex" [Hare et al., 2014], "primary vortex" [Salimi-Tarazouj et al., 2021], and "coherent vortex" [Yuan and Wang, 2019], among other terms. [Hare et al., 2014], who conducted wave tank experiments with an actual sand bed, described how these vortices begin to form downstream of the ripple crest at maximum flow forcing, growing in size as the far-field velocity decreases until flow reversal occurs. They demonstrated that these vortices, in addition to the bottom, act as a significant source of turbulence. Furthermore, they observed that the "separation bubbles" became larger during higher wave orbital excursions, which coincided with an increase in the associated Reynolds stresses. These findings align well with the observations made in this study.

Regarding the impact of alternating flow separation and recirculation zones behind ripples on the transport of a tracer fluid emerging from the seabed, it proved difficult to identify

directly comparable literature, as this specific research question has - as far as known - not yet been extensively studied in this form. However, [Reidenbach et al., 2010] investigated the transport of a passive tracer using PIV and LIF, but under unidirectional flow conditions above beds composed of sand, gravel, or cobbles. They found that over the cobbly bed, where roughness elements were comparable in height to the ripples in the present study, the significantly larger roughness enhanced fluid exchange and generated localized flux hot spots. These hot spots were found to correlate with regions of boundary layer separation and reattachment along the bed, which aligns with the observations made in the present study. Furthermore, numerous numerical and experimental studies have been conducted investigating sediment transport over wave ripples, as discussed in Section 2.5. While sediment transport and passive scalar transport share some similarities in terms of flow dynamics, they are not fully analogous. Sediment transport involves the complex interaction of particle inertia, settling velocity, and bed shear stresses, which govern the entrainment, suspension, and deposition of sand particles. Nevertheless, key flow phenomena such as flow separation, recirculation zones, and near-bed turbulence influence both processes. As a result, observations from sediment transport studies can enhance the understanding of the tracer dynamics in this study. [van der Werf et al., 2007] measured velocity and suspended sand concentration fields above wave ripples in an oscillatory flow tunnel. They found, that the sand flux was dominated by a flux associated with a suspended sand cloud generated by vortex shedding from the lee slope of the ripple around the time of flow reversal. Similarly, [Thorne et al., 2009], who conducted suspended sediment measurements above steep wave ripples, observed major inputs of sediment into suspension associated with vortex entrainment occurring around flow reversal. These findings show parallels to the observations of the present study concerning near-bed transport of the emerging tracer fluid. Lee-side vortices coincide with regions of elevated tracer concentration, particularly at flow reversal when these vortices reach their maximum size. Similar to the entrainment and suspension of sand by the recirculation zone, the tracer fluid emerging from the seabed is entrained and subsequently dispersed by the prevailing turbulent motion. Notably, the difference lies in the fact that sediment is stirred up more effectively by higher shear, leading to increased sediment concentrations, while high concentrations of tracer fluid result from pressure gradients that extract the tracer fluid from the sediment.

Impact of the Ripple Shape

The comparison of outcomes above the sinusoidal rippled seabed with those above the naturally rippled seabed, see 5.3, clearly demonstrates that the ripple contour — despite both beds being symmetric — can significantly alter the discharge and transport processes. The naturally rippled seabed has a smaller radius at the crest and a larger radius at the trough compared to the sinusoidal rippled seabed. The sharper crest was observed to lead to earlier flow separation and an extended recirculation zone, which is assumed to be additionally promoted by the shallower trough allowing for the vortex to grow. These two factors significantly increased TKE levels above the naturally rippled bed. Additionally,

the sharp ripple crest caused a focused local outflow of tracer fluid, which followed the flow towards the downstream slope, becoming available for vertical transport driven by the notably extended recirculation zone. As a result, the evaluation showed substantially enhanced vertical turbulent fluxes, with time- and horizontally averaged peak values up to three times higher above the naturally rippled bed compared to the sinusoidal rippled bed. It is noteworthy that, according to the definition provided in the literature, see 2.5, the ripple steepness is identical for both seabed models with $h_R/\lambda_R = 0.12$. However, the tangential gradient of the natural ripple contour deviates locally from that of the sinusoidal contour. These small differences appear to have a significant impact on the tracer discharge behaviour and the flow separation process.

[Barr, 2004] performed three-dimensional numerical simulations of turbulent, oscillatory flow over differently shaped sand ripples using a direct numerical simulation (DNS) model of [Winters et al., 2000]. They also identified flow separation at the ripple crest as a mechanism for turbulence production in the BBL during phases of maximum flow velocity. For steeper ripples, they observed that turbulence became more concentrated in the trough and above the crest. The oscillatory forcing in their simulation resembles the intermediate wave scenario used in this study with the same maximum flow velocity of 0.2 m/s and a period of $T = 2.45$ s, compared to $T = 2.52$ s in this study. The ripple parameters were $h_R = 18.40$ mm in height and $\lambda_R = 100.00$ mm in wavelength, which is comparable to the ripple dimensions in this study: $h_R = 19.64$ mm and $\lambda_R = 159.22$ mm. They investigated the impact of three seabed contours: "sine" (sinusoidal), "gaussian," and "steep," with the latter two showing sharper crests and shallower troughs than the sinusoidal one. The two-dimensional maps of turbulent kinetic energy, averaged over the y-direction and time, reached maximum values around 0.003 m^2/s^2 for all three bed forms. For the sinusoidal bed, regions of maximum turbulent kinetic energy were located at the ripple flanks. For the steeper bed forms, the magnitude at the slopes decreased as it became more detached from the crest and more widely distributed in the trough. When averaging the phase-resolved two-dimensional TKE_{xz}-maps computed in this study, maximum values are approximately half the magnitude observed by [Barr, 2004], but are also located directly at the ripple flanks for the sinusoidal bed. For the symmetric naturally rippled seabed, which also has a steeper crest than the sinusoidal bed, maximum TKE_{xz} values reached approximately 0.003 m^2/s^2, but were found directly at the crest, with only small magnitudes in the troughs. Furthermore, for the 0.2 m/s oscillating flow over a flat bottom, [Barr, 2004] obtained laminar results with turbulent kinetic energy being close to zero, which does not align with the experimental outcome of this study. However, although complete comparability is not given due to the fact, that the values computed by [Barr, 2004] include the fluctuation of the v-velocity component, the bed form contours are not equal and the ripple wavelength is by a third shorter, the order of magnitude of turbulent kinetic energy is certainly comparable to the values calculated in this study.

Impact of Ripple Asymmetry

The comparison of results obtained above the symmetric and above the asymmetric naturally rippled seabed, see 5.4, revealed substantial qualitative and quantitative differences. The symmetric seabed models displayed similar, though mirrored, patterns in terms of flow field, tracer distribution, turbulence, and turbulent transport during the first and the second half of the wave cycle. In contrast, the asymmetric seabed introduced distinct asymmetric effects into the periodic variations, which became particularly evident under the intermediate and stormy wave scenario.

Depending on the half-cycle of the wave, the flow either crosses a gentle or steep slope, with the downstream ripple flank being correspondingly steep or flat. As a result, the flow field is characterized by either relatively early or late flow separation, leading to fundamental differences in the extent of the resulting recirculation zones. TKE and vertical turbulent transport exhibit high magnitudes during the first half-cycle and low magnitudes during the second half-cycle. The time- and horizontally averaged TKE values are similar to those observed above the symmetric seabed, as the high values in the first half-cycle are balanced by relatively low TKE values in the second half-cycle.

Phase-resolved concentration maps suggest that the tracer output at the crest and the downstream slope of the ripples is lower compared to the symmetric naturally rippled bed. This observation may be attributed to the superposition of two effects. During the first half of the wave cycle, the flow acceleration over the ripple is less rapid, resulting in a weaker pressure gradient and, consequently, a reduced tracer output at the crest. Additionally, the lee-side vortex is more vertically expanded, possibly exerting a less pronounced influence on the outflow at the downstream slope of the ripple. In the second half of the wave cycle, although the outflow at the ripple crest promoted by the pressure gradient is well-defined, flow separation - which could otherwise further enhance tracer output - occurs late on the downstream slope, again resulting in reduced local outflow.

Thus, with simultaneously low concentration values at the seabed interface, this results in time-averaged values of vertical turbulent flux that are significantly lower above the asymmetric than above the symmetric seabed. This emphasizes the previously noted relationship: high magnitudes of vertical turbulent flux can only occur when high local concentration values are available to be transported by turbulence.

Comparable literature on the measurement configuration with the asymmetric naturally rippled bed is scarce, as such a case is not common in natural environments. Asymmetric ripples typically form in unidirectional or superimposed flow fields. When an asymmetric ripple is exposed to a symmetric oscillatory flow, processes such as sand pickup and deposition gradually lead to the development of increasingly symmetric ripple contours over time. The numerical findings by [Salimi-Tarazouj et al., 2021] effectively demonstrate that an asymmetric flow over a symmetric ripple, which is the reverse of the situation in this study, results in horizontal net sediment transport. [van der Werf et al., 2007] furthermore documented, that in the case of asymmetric flows over symmetric ripples, the vortex formation on the lee side during the wave half cycle with larger flow velocity is much stronger than on the stoss side during the wave half cycle with smaller flow velocity. Consistent

with these findings, [Yuan and Wang, 2019] observed that turbulence development varies significantly between the two wave half-cycles in asymmetric flows and hypothesized that this variation affects mass transport accordingly. In the present study, although maximum flow velocities were nearly equal during both wave half-cycles, the varying steepness of the respective downstream ripple slope led to asymmetric vortex formation due to differences in the initiation of flow separation. Earlier flow separation led to higher magnitudes of TKE_{xz} in the first wave half-cycle compared to the second. In contrast to the symmetric naturally rippled seabed, the region of high TKE at the steep downstream slope of the asymmetric ripple is larger vertically but smaller horizontally, with the vortex core positioned higher above the seabed. Additionally, the flow acceleration on the stoss side is less intense, which results in reduced local tracer fluid discharge, in line with the observations of [Precht and Huettel, 2004]. The interplay of these mechanisms is assumed to contribute to the comparably low tracer concentration values and thus, c-fluctuations available at the seabed interface. Despite high vertical velocity fluctuations, this leads to lower vertical turbulent flux compared to the symmetric bed. During the second wave half-cycle, while the concentration of the tracer fluid emerging at the crest is high, the limited turbulence generation suppresses significant vertical turbulent flux.

To summarize the evaluation of the turbulent fluxes derived from the PIV and LIF measurements, it can be concluded that the highest values were recorded above the symmetric naturally rippled seabed, followed by those above the sinusoidal rippled seabed, and lastly, the values above the asymmetric naturally rippled and the flat seabed.
Although the volumetric input flow rate forcing was identical across all measurement configurations, local concentration values varied significantly, both in phase- and spatially resolved results as well as in time-averaged data. The differences observed on temporal and spatial scales indicate that even with constant forcing, the seabed topography plays a crucial role in modulating the local tracer concentration and turbulent flux behaviour.

Turbulent Mixing Lengths

The results for the calculations of the turbulent mixing length l_c above the different seabed models under all three wave scenarios revealed several key patterns.
In general, the mixing length increases steadily near the seabed and stabilizes further away, with more outliers appearing as concentration and velocity gradients weaken with bottom distance. According to the idea of Prandtl's mixing length hypothesis, the turbulent mixing length is the characteristic distance over which a fluid parcel moves as a relatively coherent structure before losing its distinctiveness by interacting and mixing with surrounding fluid parcels. Therefore, the mixing length is by definition zero at the wall, in this case, the bottom surface, and will increase towards higher water levels.
Above the flat seabed, the mixing length profile is similar for all wave scenarios, steadily rising within the first 20 mm before levelling off around 35 mm to 40 mm. While the turbulent fluxes and velocity gradients are enhanced under the intermediate and the stormy wave scenario compared to the calm wave scenario, the larger concentration gradient

present, in this case, seems to compensate for these differences, resulting in similar mixing lengths over the flat seabed across all wave scenarios.
Above the rippled seabeds - particularly the sinusoidal and the asymmetric naturally rippled seabed - the wave scenario has a greater influence on the mixing length. Near the seabed, specifically within the first 20 mm, mixing lengths are shortest under the stormy wave scenario. This indicates that fluid parcels mix rapidly with their surroundings, losing their individuality after travelling only short distances. However, under the calm wave scenario, where the flow remains mostly attached to the bottom surface and vortex formation is absent, individual fluid parcels retain their distinct properties, such as concentration gradients, over longer distances within the near-bottom water layer.
Above the symmetric naturally rippled seabed, the mixing length increases up to two ripple heights, continuing to rise under calm waves but stabilising at 45 mm to 50 mm under intermediate and stormy waves.
Above the sinusoidal and asymmetric naturally rippled seabed, mixing lengths under intermediate and stormy waves exceed those under calm conditions above approximately 20 mm of bottom distance, which resembles one ripple height. The far-field mixing length stabilises at 35 mm (calm) and 50 mm for sinusoidal ripples, while for asymmetric ripples it stabilises at 30 mm (calm) and 80 mm (intermediate and stormy, respectively).
[Nayak et al., 2015] conducted field measurements in the inner part of the coastal ocean BBL, capturing mean flow, wave activity, roughness, and turbulence statistics. They calculated the Prandtl mixing length only for momentum under varying conditions and plotted it as a function of the distance from the seabed. For non-stratified flows, the turbulent viscosity ν_t and turbulent diffusivity D_t are generally assumed to be of similar magnitude, implying $\nu_t \approx D_t$ and, consequently, a turbulent Schmidt number of $Sc_t = \nu_t / D_t \approx 1$ [Bird et al., 2007]. In this case, the mixing lengths of momentum and mass are of comparable magnitude. [Nayak et al., 2015] reported values linearly increasing from 0 to about $30 - 40$ mm within the first 90 mm of bottom distance which agrees well in magnitude with the values determined in this study.
Furthermore, laboratory experiments conducted over both smooth and rough walls, as noted by e.g. [Tomas et al., 2011], demonstrated that within the logarithmic layer, the mixing length increases linearly with height above the seabed. Beyond this region, the mixing length approaches constant values. This behaviour, characterized by a steady increase in mixing length followed by a plateau as it reaches a certain height, was also observed in the present study.

To contextualize the observations concerning the mixing length with the previously described findings on turbulent fluxes, the following points can be made. Compared to turbulent fluxes, the mixing length is less dependent on the outflow characteristics of the tracer fluid emerging from the seabed, which, as previously demonstrated, vary significantly under different conditions. While local turbulent fluxes are strongly influenced by the location and concentration of tracer fluid exiting the seabed, the mixing length is notably less impacted by these factors. Mathematically, the mixing length normalizes turbulent fluxes by the velocity and concentration gradients. Whereas turbulent fluxes

quantify the actual local transport of the passive scalar, the mixing length reflects the flow's capacity to transport and mix scalar quantities through turbulent motion. However, because vortex formation dominates the flow field above the rippled seabed models under the intermediate and stormy wave scenarios, generating significantly more turbulent motion, the mixing length characteristics are altered compared to flows that remain primarily attached to the seabed surface.

Challenges and Limitations of the Experiment

This study was the second of three phases in the sub-project H4 within the research training group Baltic TRANSCOAST. During the first phase of the project, [Karow, 2019] modified the existing flow tank for experiments with oscillatory flow and permeable beds. Additionally,PIV-LIF measurements were also conducted to quantify vertical transport, offering valuable initial insights into the challenges and limitations of the experimental setup. Based on recommendations from [Karow, 2019] and [Kandler, 2018], which suggested enhancing the resolution of the near-bed boundary layer by increasing the number of measurement points close to the bed, this study implemented optical enlargement. This was achieved by reducing the camera distance, thereby narrowing the field of view. However, this adjustment required trade-offs in terms of a broader view. As a compromise, the enlargement was limited to ensure that at least one ripple wavelength remained within the field of view. This approach ensured that the spatial variability and characteristics of the flow-topography interaction, particularly the tracer fluid transport and turbulence structures above the ripples, were adequately captured.
Furthermore, [Kandler, 2018] documented that air bubbles rising from the artificial seabed surface can introduce measurement errors by disturbing the PIV algorithm. Besides, air bubbles trapped in the foam bed may affect the flow of tracer fluid. To address this, the seabed models must be thoroughly squeezed before the experiments (see 4.3.3). In the present study, careful attention was given to this potential source of error. However, to ensure its exclusion, future experiments should similarly take precautions to control for this factor.
Another challenge addressed in the present study was the signal-to-noise ratio of the LIF measurements. This issue arises because distinct boundary conditions differently affect the mixing and thus the dilution of the emerging tracer fluid. The dye concentration of the tracer fluid directly influences the measured pixel brightness. High concentrations can quickly lead to saturation effects or overexposure, while low concentrations result in a weak signal. Overall, the range of measurable tracer concentrations was observed to be relatively narrow compared to the dynamics of the investigated process.
To avoid overexposure in the central part of the image, where the laser light sheet is brightest, while still capturing concentration values in darker areas, a multi-stage LIF processing approach based on multiple calibration curves was employed, as thoroughly described in 4.4. In addition, the dye concentrations of the injected tracer fluid $c_{\mathrm{R6G,\ Tracer}}$ were varied based on previous test measurements. For anticipated low mixing, $c_{\mathrm{R6G,\ Tracer}}$ was reduced to prevent overexposure. Conversely, for high anticipated mixing and thus

more rapid dilution, $c_{\mathrm{R6G,\ Tracer}}$ was increased to maintain a measurable signal. This approach resulted in a high signal-to-noise ratio across all measurement configurations. However, this strategy introduced a new issue, as discussed in 4.4.3. The varying $c_{\mathrm{R6G,\ Tracer}}$ introduced into the foam models likely led to dye contamination, which may have affected subsequent measurements. Although extensive rinsing with clean water was performed after measurements to address this issue, the significant deviation in the concentration average of the measurement 'FLAT, calm' suggests that the actual amount of dye available in the foam seabed model was potentially underestimated. The computation of turbulent fluxes appeared to be particularly sensitive to this factor. Therefore, the respective measurement data was corrected as described in Section 4.4.3. For the remaining measurements, no such contamination effects were observed. High tracer concentration values in these cases could be attributed to physical mechanisms, such as correlations between these values and strong velocity fluctuations or accelerations.

Consequently, foam was identified as a challenging material because it absorbs an undefined amount of dye, which can be washed out during subsequent measurements. Manufacturing new models for each experiment would be costly and time-consuming. Additionally, it was observed during the trial phase that completely new models contained residual substances from the manufacturing process. Therefore, it is necessary to pre-flush the foam models with tracer fluid before conducting measurements. Using entirely new models for every experiment would not only be cost-intensive but also inadvisable.

[Stirnweiß et al., 2024b] recently addressed the issue described above by varying the LIF camera aperture during their measurement campaign, rather than adjusting $c_{\mathrm{R6G,\ Tracer}}$ to prevent overexposure and achieved promising results. This approach avoids issues due to undefined dye residues within the foam material and can be recommended for future measurements. However, limitations regarding resolution exist, as the aperture can only be adjusted in discrete increments. Consequently, saturation of the dye may be reached rapidly, hindering the achievement of optimal image exposure at higher f-number values. In contrast, the concentration of the tracer fluid can be adjusted with greater flexibility, offering a more adaptable approach for the measurements. Therefore, both methods offer distinct advantages and disadvantages that must be carefully considered.

While the implementation in the present study yielded reliable results, a method that eliminates the need for post-processing corrections would, of course, be preferable.

Aside from the measurement limitations, this present study is also constrained by the experimental setup and measurement technique itself. For instance, the seabed model is equivalent to a black box. While it is known how much tracer enters and where it exits, the exact processes occurring within the permeable material remain unknown. This limitation does not diminish the findings of the study, but it must be considered when interpreting the results. A measurement technique that could also capture the processes within the permeable material would be a valuable addition to the understanding of the investigated processes.

Another factor that must be kept in mind is that the introduced tracer is, to some extent, forced through the seabed model by continuous pumping with a seepage rate of $3.9 \cdot 10^{-5}$ m/s, as described in Section 4.2.3. Consequently, the fluid movement within

the seabed is not solely driven by the oscillating flow above. Despite this forcing, the tracer can still be considered passive in the sense that its presence does not noticeably impact the captured flow field due to the relatively low seepage rate. While the tracer fluid's path within the seabed is slightly influenced by the pumping process, its transport within the water column remains substantially unaffected. This factor should be considered when interpreting the results. However, given the passive nature of the tracer and the low seepage rate, the interpretation of the study results, which attribute the observed phenomena to flow-topography interactions within the BBL, is not compromised. Furthermore, in natural environments, SGD and PWE are overlapping and interacting phenomena, occurring at the same place and time as well, as detailed in Section 2.1.
The spatial limitations of the experiment should also be considered. While the wave tank is relatively large, it equals a closed system with a finite volume, leading to an increase in the average tracer concentration throughout the tank over prolonged measurement durations. This factor was taken into account when determining the measurement duration. The chosen duration represents a compromise between ensuring the convergence of velocity averages and avoiding an excessive increase in the average tracer concentration, which could distort the calculated fluctuation values and, thus, affect the results for the vertical turbulent fluxes.
Additionally, the permeable seabed model is relatively shallow - the minimum thickness was 50 mm - due to spatial constraints and does not fully represent the natural thickness of sediment layers. According to [Moore, 2010], the depth of the sediment layer influenced by advective exchange depends on the size and spacing of the ripples, typically extending to about twice the ripple wavelength in homogeneous sediments, but generally not exceeding 50 mm to 100 mm. Based on the observations made in this study, it can be assumed that the flow conditions additionally influence the depth of the affected sediment layer. Future studies could benefit from more accurate modelling of sediment thickness, especially when further investigating sediment-internal transport processes. However, the current limitations do not significantly affect the validity of the key findings. As with any experimental setup, compromises between various limitations must be made to ensure the most reliable results possible.

Contributions

Keeping these limitations in mind, however, the present study has successfully contributed to testing the underlying hypotheses. The study demonstrated how different seabed topographies significantly influence the transport and mixing of a tracer fluid emerging from the seabed. This includes both the transport of the fluid within the permeable seabed model, which was made evident through varying discharge patterns, as well as the transport within the water column. The research found that the interaction between seabed topography and oscillating flow generates varying degrees of turbulence, a key factor influencing fluid transport and local concentration values. In particular, vertical turbulent fluxes were found to be sensitive to changes in ripple contour and ripple asymmetry, which affect the initialization of flow separation and vortex formation. These findings emphasize

the importance of considering seabed features in models of passive scalar transport within the BBL.

Furthermore, it was observed that the transition from the calm to the stormy wave scenario significantly affected the spatial and temporal variability of tracer fluid discharge and transport within the water column. The study indicates that under strong oscillatory flow forcing, tracer fluid emerges more concentrated at specific locations. [Huettel et al., 1996] or [Precht and Huettel, 2004] attribute this phenomenon to the Bernoulli principle. [Santos et al., 2012] identified flow- and topography-induced pressure gradients as one of the twelve main driving forces of pore- and groundwater flow in permeable coastal sediments in their review paper. However, the results of the present study suggest that flow acceleration cannot be the sole determining factor. Rather, the presence or absence of flow separation and vortex formation appears to play a significant role in shaping the discharge characteristics. This complexity is further underscored by the observation that the symmetric naturally rippled seabed exhibited significantly higher vertical turbulent fluxes compared to the other rippled seabeds, despite featuring the same ripple height, and wavelength.

Since the experimental setup and research focus of this study represent an approach that, to the best of our knowledge, has not been applied previously, directly comparable literature was not available. However, similar studies were reviewed, and their findings support the results of this research.

The present study contributes to understanding and modelling turbulence and passive scalar transport within the BBL by demonstrating how seabed topography and wave conditions affect fluid dynamics. These factors, in turn, proved to affect the transport and mixing of tracer fluids emerging from the seabed. Notably, this research is the first to quantify turbulent fluxes and the turbulent mixing length specifically for tracer transport above rippled seabeds, offering new insights into the mechanisms that govern the distribution and movement of solutes in coastal environments and providing parameters to model these processes in numerical simulations.

Lastly, this study contributed to the improvement of the experimental setup, the measurement procedure, and the evaluation of the measured quantities. This includes successfully eliminating vertical movements of the wave tank bottom installation (see section 4.1), preventing inaccuracies caused by start-up and end effects during the experiment (see section 4.3.3) or correcting errors in the concentration fields introduced by masking in Dynamic Studio (see section 4.4). These advancements lay a solid foundation for future studies, enabling more precise and reliable data collection and analysis in similar experimental setups.

Chapter 7

Conclusion

Coastal zones, representing the dynamic interface between land and sea, play a crucial role in global biodiversity and ecological functions. While they are highly sensitive environments, they are also under strong anthropogenic pressure. Understanding the processes present in these areas can facilitate the development of strategies aimed at enhancing resilience and sustainability in coastal ecosystems.
From a fluid mechanical perspective, coastal regions are particularly intriguing, as shallow and intermediate water depths allow ocean waves to interact with the seabed, generating complex flow dynamics. The inner continental shelf, largely covered by permeable sandy sediments [Hall, 2002], facilitates significant flow rates at the sediment-water interface, making coastal sediments essential for the transport of terrestrial and sediment-originated matter [Taniguchi et al., 2019]. The discharge of pore- and groundwater through the seabed is largely influenced by wave-driven flow regimes interacting with seabed topography, such as sand ripples [Santos et al., 2012]. While the dynamics of wave-ripple interactions have been studied extensively related to sediment or momentum transport, their effect on the transport and mixing of fluids emerging from the seabed and spreading in the water column remains comparatively unattended.
To address this gap, this study conducted controlled wave tank experiments to replicate the transport processes of tracer fluid emerging from the seabed induced by wave-ripple interaction. Synchronized particle image velocimetry (PIV) and laser-induced fluorescence (LIF) measurements were employed to capture velocity and concentration fields, respectively. These data were used to investigate the vertical transport of a discharging fluid near the sediment-water interface based on the spatial tracer fluid distribution, turbulent kinetic energy, vertical turbulent fluxes and turbulent mixing lengths.

The study is based on the underlying hypothesis that the interaction between seabed topography and oscillating flow generates turbulence, which in turn influences fluid transport and the resulting local concentration values in the water column. In addition to the effect of varying wave conditions, three specific seabed characteristics were examined.
First, the general effect of a rippled seabed was investigated. Therefore, a generic sinusoidal rippled seabed was compared to a flat seabed. Under calm wave conditions, the fluid discharge and vertical transport were similar in both cases, with the tracer emerging spatially uniform from the seabed. However, under the intermediate and the stormy wave scenario, the rippled seabed surface induced a significant spatial and temporal variability of tracer discharge, with tracer fluid emerging concentrated at ripple crests and downstream slopes. Areas of elevated tracer concentrations aligned with regions of high turbulent kinetic energy linked to flow separation and vortex formation occurring at the

ripple's downstream slope. This led to considerably enhanced vertical turbulent transport emphasising the importance of seabed topography in the dynamics of fluid transport.
Second, the influence of the ripple shape was investigated by comparing the generic sinusoidal rippled seabed to a seabed developed from in-situ microtopography scans. The latter is characterised by sharper crests and wider troughs and is referred to as "naturally rippled". Alterations in ripple shape affected the timing and location of flow separation and the shape of the resulting lee vortex, which were identified as key factors influencing fluid discharge characteristics and transport within the water column. Earlier flow separation resulted in enlarged recirculation zones, promoting tracer discharge and vertical transport.
Third, the impact of ripple asymmetry on fluid dynamics and transport was analysed by comparing the symmetric naturally rippled seabed to an asymmetric version. The asymmetric seabed introduced distinct asymmetric effects into the periodic variations of the computed quantities. However, while ripple asymmetry showed significant effects in the phase-resolved findings, its overall influence diminished when averaged over an entire wave cycle.
A general finding was that the transition from calm to stormy wave conditions had a more substantial impact on fluid transport than the seabed characteristics, which highlights the crucial role of wave dynamics on the transport of sediment-originated fluids.
In summary, despite maintaining an identical volumetric flow rate forcing across all measurement configurations, the local concentration values exhibited considerable variability, evident in the phase-resolved results, as well as in time-averaged data. The observed differences across temporal and spatial scales indicate that even with constant forcing, the interaction between flow and topography significantly influences local tracer concentration and turbulent flux behaviour.
For all measurement configurations, the turbulent mixing lengths increased steadily with height above the seabed but approached constant values beyond a certain bottom distance. Above the flat seabed, the mixing length profile was not considerably affected by the wave scenarios. In contrast, above the rippled seabeds, the wave scenario had a greater influence on the mixing length: Under strong wave forcing, the occurring vortices led to comparably low mixing length, as they trapped and rapidly mixed the discharging tracer fluid with the surrounding fluid.
The study demonstrated that while local turbulent fluxes are strongly influenced by the location and concentration of tracer fluid exiting the seabed, the mixing length is notably less impacted by these factors, as it normalises turbulent fluxes by the velocity and concentration gradients. Whereas turbulent fluxes quantify the actual local transport of the passive scalar, the mixing length reflects the flow's capacity to transport and mix scalar quantities through turbulent motion.

The results have practical implications for environmental management and engineering, particularly regarding changes in seabed morphology due to natural processes or human activities, and their effects on water quality and solute transport dynamics. The knowledge acquired from this study can facilitate further investigations into the interactions

between fluid dynamics and seabed characteristics, potentially resulting in new discoveries regarding solute transport and its ecological impacts.
The study employed advanced experimental techniques, such as synchronous PIV and LIF, to quantify the fluid dynamics. The experimental setup and procedure were considerably improved upon previous studies. Furthermore, the evaluation and analysis were refined. This methodological approach can serve as a reference for future investigations and has already been applied and further updated by [Stirnweiß et al., 2024b].
The findings align well with comparable literature and emphasize the need to incorporate seabed topography into fluid dynamics and solute transport models. By demonstrating the effect of seabed topography and wave conditions on fluid dynamics, this study enhances the understanding of turbulence and passive scalar transport within the benthic boundary layer. Notably, it is the first to quantify turbulent fluxes and the turbulent mixing length specifically for tracer transport above rippled seabeds, providing new parameters for modelling these processes in numerical simulations.
Furthermore, the study highlights the importance of considering seabed topography in solute transport models and emphasizes the need for further research on the interactions between seabed morphology and fluid behaviour. Future research directions could explore less asymmetric profiles to assess if effects remain visible, investigate the effect of wave-current superposition, and examine other topographical features such as gravel [Stirnweiß et al., 2024a] or the influence of macrofauna through bioturbation and -irrigation building on studies such as [Meysman et al., 2007]. Lastly, it would be interesting to complement the transport processes in the bottom water layer, as investigated in the present study, by also determining and visualizing the fluid transport within the permeable seabed.

List of Figures

List of Tables

Nomenclature

Mathematical Operators

$\overline{\gamma}$	time-averaged value of γ
$\widetilde{\gamma}$	periodic variation of γ
γ'	fluctuation value of γ
$\langle\gamma\rangle$	phase-averaged value of γ (general notation)
$\langle\gamma\rangle_\varphi$	phase-averaged value of γ, specifically defined by the method applied in this thesis, see Section 4.4.1
$\langle\gamma\rangle_x$	horizontally averaged value of γ
$\langle\overline{\gamma}\rangle_x$	time- and horizontally averaged value of γ
$\Delta\gamma$	absolute difference of γ
$//$	integer division

Latin Characters

A	m^2	area
a	m	wave amplitude
a_P	$\mathrm{m/s}^2$	wave generator piston acceleration
c	$\mathrm{L/m}^3$	(tracer fluid) concentration
$c_{\mathrm{R6G,Tracer}}$	µg/L	Rhodamine 6G concentration of injected tracer fluid
c_{R6G}	µg/L	Rhodamine 6G concentration measured in the water column
d	m	water depth
D_m	m^2/s	molecular diffusivity
D_t	m^2/s	turbulent diffusivity
E_{pb}		number of entries of a specific phase bin
F		fluorescence intensity
f_i	$\mathrm{kg\ m/s}^2$	external forces
g	$\mathrm{m/s}^2$	gravitational acceleration
H	m	wave height
h	m	water level
H_E	m	Ekman height
h_R	10^{-3} m	ripple height

I		pixel intensity value at coordinates (m, n)
I'		pixel intensity value at coordinates $(m + x, n + z)$
I_{sat}		saturation intensity
K	m^2	permeability
k	/m	wave number
k_f	m/s	hydraulic conductivity
L	m	length
l_c	10^{-3} m	turbulent mixing length of concentration
l_t	m	turbulent mixing length of momentum
M		number of IA pixels in x-direction
m		pixel index in the x-direction
N		number of IA pixels in z-direction
n		pixel index in the z-direction
N_{pb}		number of phase bins
n_{pb}		numbering of phase bin
p	$\mathrm{kg/m/s}^2$	pressure
u_i	m/s	velocity vector
Q	m^3/s	volumetric flow rate
q	m/s	seepage rate
r_C	m	ripple crest radius
r_T	m	ripple trough radius
R_{II}		cross-correlation value
Re		Reynolds number
Re_W		wave Reynolds number
$RMSD$	m/s	root mean square deviation of horizontal velocity
RSI		ripple symmetry index
s_{lee}	(°)	ripple lee slope
s_{stoss}	(°)	ripple stoss slope
T	s	wave period
t	s	time
t_{zc}	s	exact time of zero crossing
TKE	$\mathrm{m}^2/\mathrm{s}^2$	turbulent kinetic energy
TKE_{xz}	$\mathrm{m}^2/\mathrm{s}^2$	in-plane turbulent kinetic energy
u	m/s	horizontal velocity component
u_D	m/s	Darcy velocity
$\widetilde{u}_{rms}$	m/s	root-mean-squared oscillatory velocity
u_W	m/s	wave speed
$u_{orb,max}$	m/s	maximum bottom orbital velocitiy
v_P	m/s	wave generator piston velocity
w	m/s	vertical velocity component
x		Cartesian coordinate in horizontal direction
x_P	m	wave generator piston feed

X_{FoV}		number of data entries in horizontal direction of data array
z		Cartesian coordinate in vertical direction
z^*	10^{-3} m	bottom distance
z_0	10^{-3} m	bottom height of the artificial seabed

Greek Characters

α	10^{-3} m	ripple stoss side length
β	10^{-3} m	ripple lee side length
γ		arbitrary scalar or vector quantity
λ	m	wavelength
λ_R	10^{-3} m	ripple wavelength
ν	m^2/s	kinematic viscosity
ν_t	m^2/s	turbulent viscosity
ω	/s	wave angular frequency
ρ	kg/m^3	density
τ_{ij}	$kg/m/s^2$	Reynolds stress tensor
φ	rad	phase angle
φ_{ts}	rad	phase angle of a specific time step
η	kg/m/s	dynamic viscosity
ζ	m	displacement of water surface

Acronyms

ASYM	asymmetric naturally rippled seabed model
AWAC	acoustic wave and current profiler
BBL	benthic boundary layer
CAD	computer-aided design
CCD	charge-coupled device
CNC	computerized numerical control
DFG	Deutsche Forschungsgemeinschaft - German Research Foundation
DNS	direct numerical simulation
FLAT	generic flat seabed model
FoV	field of view
FSGD	fresh submarine groundwater discharge
FTF	fluorescent tracer fluid

IA	interrogation area
IOW	Leibniz-Institut für Ostseeforschung Warnemünde
LES	large eddy simulation
LIF	laser-induced fluorescence
NaN	not a number
NASA	National Aeronautics and Space Administration
NAT	symmetric naturally rippled seabed model
Nd:YAG	neodymium-doped yttrium aluminum garnet
PIV	particle image velocimetry
PLIF	planar laser-induced fluorescence
PMMA	polymethylmethacrylate
POM	polyoxymethylen
PU	polyurethane
PWE	pore water exchange
RANS	Reynolds-averaged Navier-Stokes equations
RMSD	root mean square deviation
RSI	ripple symmetry index
SBM	permeable artificial seabed model
SGD	submarine groundwater discharge
SIN	generic sinusoidal rippled seabed model
STE	subterranean estuaries
TKE	in-plane turbulent kinetic energy

Bibliography

[Airy, 1845] Airy, G. B. (1845). Tides and waves. *Encyclopedia Metropolitana*, pages 241–396.

[Amos et al., 2018] Amos, C. L., Kassem, H., and Friend, P. L. (2018). Ripple marks. In Finkl, C. W. and Makowski, C., editors, *Encyclopedia of Coastal Science*, Encyclopedia of Earth Sciences Series, pages 1–8. Springer International Publishing, Cham.

[Ayrton and Ayrton, 1910] Ayrton, H. and Ayrton, W. E. (1910). The origin and growth of ripple-mark. *Proceedings of the Royal Society of London. Series A. Mathematical and Physical Sciences*, 84(571):285–310.

[Bagnold, 1946] Bagnold, R. A. (1946). Motion of waves in shallow water. interaction between waves and sand bottoms. *Proceedings of the Royal Society of London. Series A. Mathematical and Physical Sciences*, 187(1008):1–18.

[Barr, 2004] Barr, B. C. (2004). Numerical simulation of turbulent, oscillatory flow over sand ripples. *Journal of Geophysical Research*, 109(C9).

[Bear, 1988] Bear, J. (1988). *Dynamics of fluids in porous media*. Courier Corporation.

[Berg et al., 2022] Berg, P., Huettel, M., Glud, R. N., Reimers, C. E., and Attard, K. M. (2022). Aquatic eddy covariance: The method and its contributions to defining oxygen and carbon fluxes in marine environments. *Annual review of marine science*, 14:431–455.

[Berg et al., 2003] Berg, P., Røy, H., Janssen, F., Meyer, V., Jørgensen, B. B., Huettel, M., and de Beer, D. (2003). Oxygen uptake by aquatic sediments measured with a novel non-invasive eddy-correlation technique. *Marine Ecology Progress Series*, 261:75–83.

[Bestier, 2016] Bestier, T. (2016). *Bestimmung von Geschwindigkeits- und Konzentrationsfeldern mittels PIV/LIF Verfahren am Grundwasseraustritt in einer marinen Bodengrenzschicht*. Student research project, Universität Rostock, Rostock.

[Bird et al., 2007] Bird, R. B., Stewart, W. E., and Lightfoot, E. N. (2007). *Transport phenomena*. J. Wiley, New York, rev. 2nd ed. edition.

[Bokuniewicz, 1980] Bokuniewicz, H. (1980). Groundwater seepage into great south bay, new york. *Estuarine and Coastal Marine Science*, 10(4):437–444.

[Bonan, 2015] Bonan, G. (2015). Turbulent fluxes. In Bonan, G., editor, *Ecological Climatology*, pages 209–217. Cambridge University Press.

[Boudreau and Jørgensen, 2001] Boudreau, B. P. and Jørgensen, B. B. (2001). *The benthic boundary layer: Transport processes and biogeochemistry*. Oxford University Press, Oxford and New York.

[Boussinesq, 1878] Boussinesq, J. (1878). Complément à une étude intitulée « essai sur la théorie des eaux courantes » (publiée dans les tomes xxiii, xxiv du « recueil des savants étrangers »), et à un mémoire « sur l'influence des frottements dans les mouvements réguliers des fluides » (inséré au tome xiii du « journal de mathématiques pures et appliquées », 2e série, 1868). *Journal de Mathématiques Pures et Appliquées*, (Serie 3, Volume 4):pp. 335–376.

[Burnett et al., 2003] Burnett, W. C., Bokuniewicz, H., Huettel, M., Moore, W. S., and Taniguchi, M. (2003). Groundwater and pore water inputs to the coastal zone. *Biogeochemistry*, 66(1/2):3–33.

[Cardenas et al., 2008] Cardenas, M. B., Cook, P. L., Jiang, H., and Traykovski, P. (2008). Constraining denitrification in permeable wave-influenced marine sediment using linked hydrodynamic and biogeochemical modeling. *Earth and Planetary Science Letters*, 275(1-2):127–137.

[Clifton and Dingler, 1984] Clifton, H. and Dingler, J. R. (1984). Wave-formed structures and paleoenvironmental reconstruction. *Marine Geology*, 60(1-4):165–198.

[Combest et al., 2011] Combest, D. P., Ramachandran, P. A., and Dudukovic, M. P. (2011). On the gradient diffusion hypothesis and passive scalar transport in turbulent flows. *Industrial & Engineering Chemistry Research*, 50(15):8817–8823.

[Cook et al., 2018] Cook, P. G., Rodellas, V., and Stieglitz, T. C. (2018). Quantifying surface water, porewater, and groundwater interactions using tracers: Tracer fluxes, water fluxes, and end–member concentrations. *Water Resources Research*, 54(3):2452–2465.

[Cooley et al., 2023] Cooley, S., Schoeman, D., Bopp, L., Boyd, P., Donner, S., Ghebrehiwet, D. Y., Ito, S.-I., Kiessling, W., Martinetto, P., Ojea, E., Racault, M.-F., Rost, B., Skern-Mauritzen, and M. (2023). Oceans and coastal ecosystems and their services. In Pörtner, H.-O., Roberts, D. C., Tignor, M., Poloczanska, E. S., Mintenbeck, K., Alegría, A., Craig, M., Langsdorf, S., Löschke, S., Möller, V., Okem, A., and Intergovernmental Panel on Climate Change, editors, *Climate Change 2022 – Impacts, Adaptation and Vulnerability*, pages 379–550. Cambridge University Press.

[Crimaldi, 2008] Crimaldi, J. P. (2008). Planar laser induced fluorescence in aqueous flows. *Experiments in Fluids*, 44(6):851–863.

[Dantec Dynamics A/S,] Dantec Dynamics A/S. Measurement principles of planar-lif.

[Dantec Dynamics A/S, 2021] Dantec Dynamics A/S (2021). Dynamicstudio user's guide.

[Darwin, 1883] Darwin, G. H. (1883). I. on the formation of ripple-mark in sand. *Proceedings of the Royal Society of London*, 36(228-231):18–43.

[Davies and Thorne, 2005] Davies, A. G. and Thorne, P. D. (2005). Modeling and measurement of sediment transport by waves in the vortex ripple regime. *Journal of Geophysical Research*, 110(C5).

[Davies and Thorne, 2008] Davies, A. G. and Thorne, P. D. (2008). Advances in the study of moving sediments and evolving seabeds. *Surveys in Geophysics*, 29(1):1–36.

[Dean and Dalrymple, 2001] Dean, R. G. and Dalrymple, R. A. (2001). *Coastal Processes with Engineering Applications*. Cambridge University Press, Cambridge.

[Ferziger and Perić, 2008] Ferziger, J. H. and Perić, M. (2008). *Numerische Strömungsmechanik*. Springer, Berlin.

[Garrison and Ellis, 2018] Garrison, T. and Ellis, R. (2018). *Essentials of oceanography*. National Geographic Learning and Cengage Learning, Australia and Brazil and Mexico and Boston, MA, eighth edition, student edition edition.

[Gaskin, 1995] Gaskin, S. J. (1995). *Single buoyant jets in a crossflow and the advected line thermal*. Dissertation, University of Canterbury, Canterbury.

[Gili et al., 2020] Gili, J.-M., Vendrell-Simón, B., Arntz, W., Sabater, F., and Ros, J. (2020). The benthos: the ocean's last boundary? *Scientia Marina*, 84(4):463–475.

[Grant and Madsen, 1986] Grant, W. D. and Madsen, O. S. (1986). The continental-shelf bottom boundary layer. *Annual Review of Fluid Mechanics*, 18(1):265–305.

[Hall, 2002] Hall, S. J. (2002). The continental shelf benthic ecosystem: current status, agents for change and future prospects. *Environmental Conservation*, 29(3):350–374.

[Hare et al., 2014] Hare, J., Hay, A. E., Zedel, L., and Cheel, R. (2014). Observations of the space-time structure of flow, turbulence, and stress over orbital-scale ripples. *Journal of Geophysical Research: Oceans*, 119(3):1876–1898.

[Heimbuch, 2014] Heimbuch, M. (2014). *Auslegung, Fertigung und Erprobung eines Wellengenerators*. Bachelorarbeit, Universität Rostock, Rostock.

[Hjertager et al., 2003] Hjertager, L. K., Hjertager, B. H., Deen, N. G., and Solberg, T. (2003). Measurement of turbulent mixing in a confined wake flow using combined piv and plif. *The Canadian Journal of Chemical Engineering*, 81(6):1149–1158.

[Hjertager Osenbroch et al., 2008] Hjertager Osenbroch, L. K., Hjertager, B. H., and Solberg, T. (2008). Experimental and computational studies of turbulent mass transfer in a mixing channel. *International Journal of Chemical Reactor Engineering*, 6(1).

[Hölting and Coldewey, 2019] Hölting, B. and Coldewey, W. G. (2019). *Hydrogeology*. Springer Berlin Heidelberg, Berlin, Heidelberg.

[Huettel et al., 2014] Huettel, M., Berg, P., and Kostka, J. E. (2014). Benthic exchange and biogeochemical cycling in permeable sediments. *Annual review of marine science*, 6:23–51.

[Huettel and Gust, 1992] Huettel, M. and Gust, G. (1992). Solute release mechanisms from confined sediment cores in stirred benthic chambers and flume flows. *Marine Ecology Progress Series*, 82:187–197.

[Huettel et al., 1996] Huettel, M., Ziebis, W., and Forster, S. (1996). Flow-induced uptake of particulate matter in permeable sediments. *Limnology and Oceanography*, 41(2):309–322.

[Hugenschmidt, 2007] Hugenschmidt, M. (2007). *Lasermesstechnik: Diagnostik der Kurzzeitphysik ; mit 12 Tabellen*. Springer-Lehrbuch. Springer, Berlin and Heidelberg and New York.

[Johannes, 1980] Johannes, R. E. (1980). The ecological significance of the submarine discharge of groundwater. *Marine Ecology Progress Series*, 3:365–373.

[Jurasinski et al., 2018] Jurasinski, G., Janssen, M., Voss, M., Böttcher, M. E., Brede, M., Burchard, H., Forster, S., Gosch, L., Gräwe, U., Gründling-Pfaff, S., Haider, F., Ibenthal, M., Karow, N., Karsten, U., Kreuzburg, M., Lange, X., Leinweber, P., Massmann, G., Ptak, T., Rezanezhad, F., Rehder, G., Romoth, K., Schade, H., Schubert, H., Schulz-Vogt, H., Sokolova, I. M., Strehse, R., Unger, V., Westphal, J., and Lennartz, B. (2018). Understanding the coastal ecocline: Assessing sea–land interactions at non-tidal, low-lying coasts through interdisciplinary research. *Frontiers in Marine Science*, 5:2473.

[Kandler, 2018] Kandler, L. (2018). *Bestimmung der Transportkoeffizienten von ausgetretenem Bodengrundwasser in der marinen Bodengrenzschicht bei verschiedenen Hangneigungen*. Master's thesis, University of Rostock, Rostock.

[Kandler et al., 2021] Kandler, L., Grundmann, S., and Brede, M. (2021). Piv-lif untersuchungen von passivem skalartransport über boden- rippeln. In Fischer, A., editor, *Experimentelle Strömungsmechanik*, volume 28, pages 32.1–32.7. Deutsche Gesellschaft für Laser-Anemometrie - German Association for Laser Anemometry GALA e.V, Karlsruhe.

[Karow, 2019] Karow, N. (2019). *Waves and turbulence on wavy coastal seabeds inducing vertical scalar transport*. Dissertation, University of Rostock, Rostock, Germany.

[Kaufmann, 2015] Kaufmann, H. (2015). *Optimierung eines Wasserkanals zur Erzeugung von Oberflächenwellen*. Bachelorarbeit, Universität Rostock, Rostock.

[Kievsky et al., 2008] Kievsky, Y. Y., Carey, B., Naik, S., Mangan, N., ben Avraham, D., and Sokolov, I. (2008). Dynamics of molecular diffusion of rhodamine 6g in silica nanochannels. *The Journal of chemical physics*, 128(15):151102.

[Klettke et al., 2023] Klettke, H., Kandler, L., Brede, M., and Grundmann, S. (2023). Turbulenter transport und vermischung von submarinem grund- wasseraustritt: Der einfluss grober sedimentklassen in gemischten meeresböden. In Kähler, C. J., editor, *Experimentelle Strömungsmechanik*, volume 30, pages 39.1–39.8. GALA, Karlsruhe.

[Kohout, 1979] Kohout, F. A. (1979). Satellite observations of a geothermal submarine spring off florida west coast.

[Kraume, 2012] Kraume, M. (2012). *Transportvorgänge in der Verfahrenstechnik: Grundlagen und apparative Umsetzungen*. VDI Verfahrenstechnik. Springer Vieweg, Berlin, 2., bearb. aufl. edition.

[Lee, 1977] Lee, D. R. (1977). A device for measuring seepage flux in lakes and estuaries1. *Limnology and Oceanography*, 22(1):140–147.

[Leftheriotis and Dimas, 2022] Leftheriotis, G. A. and Dimas, A. A. (2022). Morphodynamics of vortex ripple creation under constant and changing oscillatory flow conditions. *Coastal Engineering*, 177:104198.

[Lueck et al., 2019] Lueck, R., St. Laurent, L., and Moum, J. (2019). Turbulence in the benthic boundary layer. In Cochran, J. K., Bokuniewicz, H. J., and Yager, P. L., editors, *Encyclopedia of ocean sciences*, pages 578–585. Academic Press, Amsterdam.

[Lueck et al., 2008] Lueck, R., St. Laurrent, L., and Moum, J. N. (2008). Turbulence in the benthic boundary layer. In Steele, J. H., editor, *Encyclopedia of Ocean Sciences (2nd ed.)*, pages 141–147. Academic Press.

[Luijendijk et al., 2020] Luijendijk, E., Gleeson, T., and Moosdorf, N. (2020). Fresh groundwater discharge insignificant for the world's oceans but important for coastal ecosystems. *Nature communications*, 11(1):1260.

[Malarkey et al., 2015] Malarkey, J., Magar, V., and Davies, A. G. (2015). Mixing efficiency of sediment and momentum above rippled beds under oscillatory flows. *Continental Shelf Research*, 108:76–88.

[McLachlan and Turner, 1994] McLachlan, A. and Turner, I. (1994). The interstitial environment of sandy beaches. *Marine Ecology*, 15(3-4):177–212.

[Meissner, 2020] Meissner, A. (2020). *Entwicklung einer Methode zur Realisierung von Meeresbodenmodellen auf Grundlage von Unterwasser- Mikrotopografie-Messungen*. Studienarbeit, Universität Rostock, Rostock.

[Merzkirch, 2011] Merzkirch, W. (2011). Particle image velocimetry. In Mayinger, F., editor, *Optical measurements*, Heat and mass transfer, pages 337–353. Springer, Berlin.

[Meysman et al., 2007] Meysman, F. J. R., Galaktionov, O. S., Cook, P. L. M., Janssen, F., Huettel, M., and Middelburg, J. J. (2007). Quantifying biologically and physically induced flow and tracer dynamics in permeable sediments. *Biogeosciences*, 4(4):627–646.

[Moore, 1996] Moore, W. S. (1996). Large groundwater inputs to coastal waters revealed by 226ra enrichments. *Nature*, 380(6575):612–614.

[Moore, 2010] Moore, W. S. (2010). The effect of submarine groundwater discharge on the ocean. *Annual review of marine science*, 2:59–88.

[Moosdorf et al., 2021] Moosdorf, N., Böttcher, M. E., Adyasari, D., Erkul, E., Gilfedder, B. S., Greskowiak, J., Jenner, A.-K., Kotwicki, L., Massmann, G., Müller-Petke,

M., Oehler, T., Post, V., Prien, R., Scholten, J., Siemon, B., Ehlert von Ahn, C. M., Walther, M., Waska, H., Wunderlich, T., and Mallast, U. (2021). A state-of-the-art perspective on the characterization of subterranean estuaries at the regional scale. *Frontiers in Earth Science*, 9.

[Moosdorf and Oehler, 2017] Moosdorf, N. and Oehler, T. (2017). Societal use of fresh submarine groundwater discharge: An overlooked water resource. *Earth-Science Reviews*, 171:338–348.

[Nayak et al., 2015] Nayak, A. R., Li, C., Kiani, B. T., and Katz, J. (2015). On the wave and current interaction with a rippled seabed in the coastal ocean bottom boundary layer. *Journal of Geophysical Research: Oceans*, 120(7):4595–4624.

[Nelson et al., 2013] Nelson, T. R., Voulgaris, G., and Traykovski, P. (2013). Predicting wave–induced ripple equilibrium geometry. *Journal of Geophysical Research: Oceans*, 118(6):3202–3220.

[Nielsen, 1992] Nielsen, P. (1992). *Coastal botton boundary layers and sediment transport*, volume 4 of *Advances Series on Ocean Engineering*. World Scientific, Singapore[etc].

[Oertel et al., 2012] Oertel, H., Böhle, M., and Prandtl, L. (2012). *Prandtl - Führer durch die Strömungslehre: Grundlagen und Phänomene*. Springer Fachmedien Wiesbaden, Wiesbaden and s.l., 13., überarb. aufl. 2012 edition.

[Ostermann et al., 2015] Ostermann, F., Woszidlo, R., Nayeri, C. N., and Paschereit, C. O. (2015). Phase-averaging methods for the natural flowfield of a fluidic oscillator. *AIAA Journal*, 53(8):2359–2368.

[Ourmières and Chaplin, 2004] Ourmières, Y. and Chaplin, J. R. (2004). Visualizations of the disturbed-laminar wave-induced flow above a rippled bed. *Experiments in Fluids*, 36(6):908–918.

[Oxford English Dictionary, 2024] Oxford English Dictionary, editor (2024). *Oxford English Dictionary: s.v. "ripple mark (n.)"*. Oxford University Press.

[Pomeroy et al., 2017] Pomeroy, A. W. M., Lowe, R. J., Ghisalberti, M., Storlazzi, C., Symonds, G., and Roelvink, D. (2017). Sediment transport in the presence of large reef bottom roughness. *Journal of Geophysical Research: Oceans*, 122(2):1347–1368.

[Pope, 2000] Pope, S. B. (2000). *Turbulent flows*. Cambridge University Press, Cambridge and New York.

[Precht and Huettel, 2003] Precht, E. and Huettel, M. (2003). Advective pore-water exchange driven by surface gravity waves and its ecological implications. *Limnology and Oceanography*, 48(4):1674–1684.

[Precht and Huettel, 2004] Precht, E. and Huettel, M. (2004). Rapid wave-driven advective pore water exchange in a permeable coastal sediment. *Journal of Sea Research*, 51(2):93–107.

[Racasa et al., 2021] Racasa, E. D., Lennartz, B., Toro, M., and Janssen, M. (2021). Submarine groundwater discharge from non-tidal coastal peatlands along the baltic sea. *Frontiers in Earth Science*, 9.

[Raffel et al., 2018] Raffel, M., Willert, C. E., Scarano, F., Kähler, C. J., Wereley, S. T., and Kompenhans, J. (2018). *Particle Image Velocimetry: A Practical Guide*. Springer International Publishing and Imprint and Springer, Cham, 3rd ed. 2018 edition.

[Reidenbach et al., 2010] Reidenbach, M. A., Limm, M., Hondzo, M., and Stacey, M. T. (2010). Effects of bed roughness on boundary layer mixing and mass flux across the sediment–water interface. *Water Resources Research*, 46(7).

[Reynolds, 1883] Reynolds, O. (1883). An experimental investigation of the circumstances which determine whether the motion of water shall be direct or sinuous, and of the law of resistance in parallel channels. *Philosophical Transactions of the Royal Society of London*, 174:935–982.

[Reynolds, 1895] Reynolds, O. (1895). On the dynamical theory of incompressible viscous fluids and the determination of the criterion. *Philosophical Transactions of the Royal Society of London. (A.)*, 186:123–164.

[Rodi, 1993] Rodi, W. (1993). On the simulation of turbulent flow past bluff bodies. *Journal of Wind Engineering and Industrial Aerodynamics*, 46-47:3–19.

[Rosenberry and Morin, 2004] Rosenberry, D. O. and Morin, R. H. (2004). Use of an electromagnetic seepage meter to investigate temporal variability in lake seepage. *Ground water*, 42(1):68–77.

[Ruggeri et al., 2020] Ruggeri, A., Musumeci, R. E., and Faraci, C. (2020). Wave-current flow and vorticity close to a fixed rippled bed. *Journal of Marine Science and Engineering*, 8(11):867.

[Salimi-Tarazouj et al., 2021] Salimi-Tarazouj, A., Hsu, T.-J., Traykovski, P., Cheng, Z., and Chauchat, J. (2021). A numerical study of onshore ripple migration using a eulerian two–phase model. *Journal of Geophysical Research: Oceans*, 126(2).

[Santos et al., 2012] Santos, I. R., Eyre, B. D., and Huettel, M. (2012). The driving forces of porewater and groundwater flow in permeable coastal sediments: A review. *Estuarine, Coastal and Shelf Science*, 98:1–15.

[Schade, 2019] Schade, H. (2019). Sediment permeability, huetelmoor: E-mail.

[Schaumstoffe Wegerich GmbH, 2021] Schaumstoffe Wegerich GmbH (2021). fabrication tolerance of foam cnc-cutting, foam bulk density and shore hardness: E-mail 01.02.21.

[Schlichting et al., 2006] Schlichting, H., Gersten, K., and Krause, E. (2006). *Grenzschicht-Theorie*. Springer, Berlin, 10., überarb. aufl. edition.

[Schönke et al., 2017] Schönke, M., Feldens, P., Wilken, D., Papenmeier, S., Heinrich, C., von Deimling, J. S., Held, P., and Krastel, S. (2017). Impact of lanice conchilega on seafloor microtopography off the island of sylt (german bight, se north sea). *Geo-Marine Letters*, 37(3):305–318.

[Selley, 2000] Selley, R. C. (2000). *Applied sedimentology*. Academic Press, San Diego, 2nd ed. edition.

[Shum, 1995] Shum, K. T. (1995). A numerical study of the wave-induced solute transport above a rippled bed. *Journal of Fluid Mechanics*, 299:267–288.

[Sigloch, 2017] Sigloch, H. (2017). *Technische Fluidmechanik*. Springer Vieweg, Berlin, Heidelberg, 10., aktualisierte auflage edition.

[Smith et al., 2009] Smith, A. J., Herne, D. E., and Turner, J. V. (2009). Wave effects on submarine groundwater seepage measurement. *Advances in Water Resources*, 32(6):820–833.

[Socolofsky and Jirka, 2005] Socolofsky, S. A. and Jirka, G. H. (2005). Special topics in mixing and transport processes in the environment. engineering-lectures [online].

[Soulsby et al., 2012] Soulsby, R. L., Whitehouse, R., and Marten, K. V. (2012). Prediction of time-evolving sand ripples in shelf seas. *Continental Shelf Research*, 38:47–62.

[Southard, 2024] Southard, J. (2024). *Introduction to Fluid Motions and Sediment Transport*. LibreTexts Project.

[Spurk and Aksel, 2010] Spurk, J. H. and Aksel, N. (2010). *Strömungslehre: Einführung in die Theorie der Strömungen*. Springer-Lehrbuch. Springer-Verlag Berlin Heidelberg, Berlin, Heidelberg, 8. aufl. edition.

[Stirnweiß et al., 2024a] Stirnweiß, H., Kandler, L., Grundmann, S., and Brede, M. (2024a). The impact of wave-topography interaction on submarine groundwater discharge - transport, turbulence, and mixing over rough seabeds. *(Manuscript accepted for publication in the Journal of Hydrology).*

[Stirnweiß et al., 2024b] Stirnweiß, H., Kandler, L., Grundmann, S., and Brede, M. (2024b). A wave tank study of passive turbulent transport and mixing above gravelly sands. *(Manuscript submitted to the Journal of Geophysical Research: Oceans).*

[Taniguchi et al., 2002] Taniguchi, M., Burnett, W. C., Cable, J. E., and Turner, J. V. (2002). Investigation of submarine groundwater discharge. *Hydrological Processes*, 16(11):2115–2129.

[Taniguchi et al., 2019] Taniguchi, M., Dulai, H., Burnett, K. M., Santos, I. R., Sugimoto, R., Stieglitz, T., Kim, G., Moosdorf, N., and Burnett, W. C. (2019). Submarine groundwater discharge: Updates on its measurement techniques, geophysical drivers, magnitudes, and effects. *Frontiers in Environmental Science*, 7.

[Tanner, 1967] Tanner, W. F. (1967). Ripple mark indices and their uses. *Sedimentology*, 9(2):89–104.

[Thorne et al., 2009] Thorne, P. D., Davies, A. G., and Bell, P. S. (2009). Observations and analysis of sediment diffusivity profiles over sandy rippled beds under waves. *Journal of Geophysical Research*, 114(C2).

[Tipler et al., 2019] Tipler, P. A., Mosca, G., Kersten, P., and Wagner, J. (2019). *Physik*. Springer Berlin Heidelberg, Berlin, Heidelberg.

[Tomas et al., 2011] Tomas, S., Eiff, O., and Masson, V. (2011). Experimental investigation of turbulent momentum transfer in a neutral boundary layer over a rough surface. *Boundary-Layer Meteorology*, 138(3):385–411.

[van der Werf et al., 2007] van der Werf, J. J., Doucette, J. S., O'Donoghue, T., and Ribberink, J. S. (2007). Detailed measurements of velocities and suspended sand concentrations over full–scale ripples in regular oscillatory flow. *Journal of Geophysical Research*, 112(F2).

[Wiberg and Harris, 1994] Wiberg, P. L. and Harris, C. K. (1994). Ripple geometry in wave–dominated environments. *Journal of Geophysical Research*, 99(C1):775–789.

[Winters et al., 2000] Winters, K. B., Seim, H. E., and Finnigan, T. D. (2000). Simulation of non-hydrostatic, density-stratified flow in irregular domains. *International Journal for Numerical Methods in Fluids*, 32(3):263–284.

[Yarborough, 1974] Yarborough, J. M. (1974). cw dye laser emission spanning the visible spectrum. *Applied Physics Letters*, 24(12):629–630.

[Yuan and Wang, 2018] Yuan, J. and Wang, D. (2018). Experimental investigation of total bottom shear stress for oscillatory flows over sand ripples. *Journal of Geophysical Research: Oceans*, 123(9):6481–6502.

[Yuan and Wang, 2019] Yuan, J. and Wang, D. (2019). An experimental investigation of acceleration–skewed oscillatory flow over vortex ripples. *Journal of Geophysical Research: Oceans*, 124(12):9620–9643.

Appendices

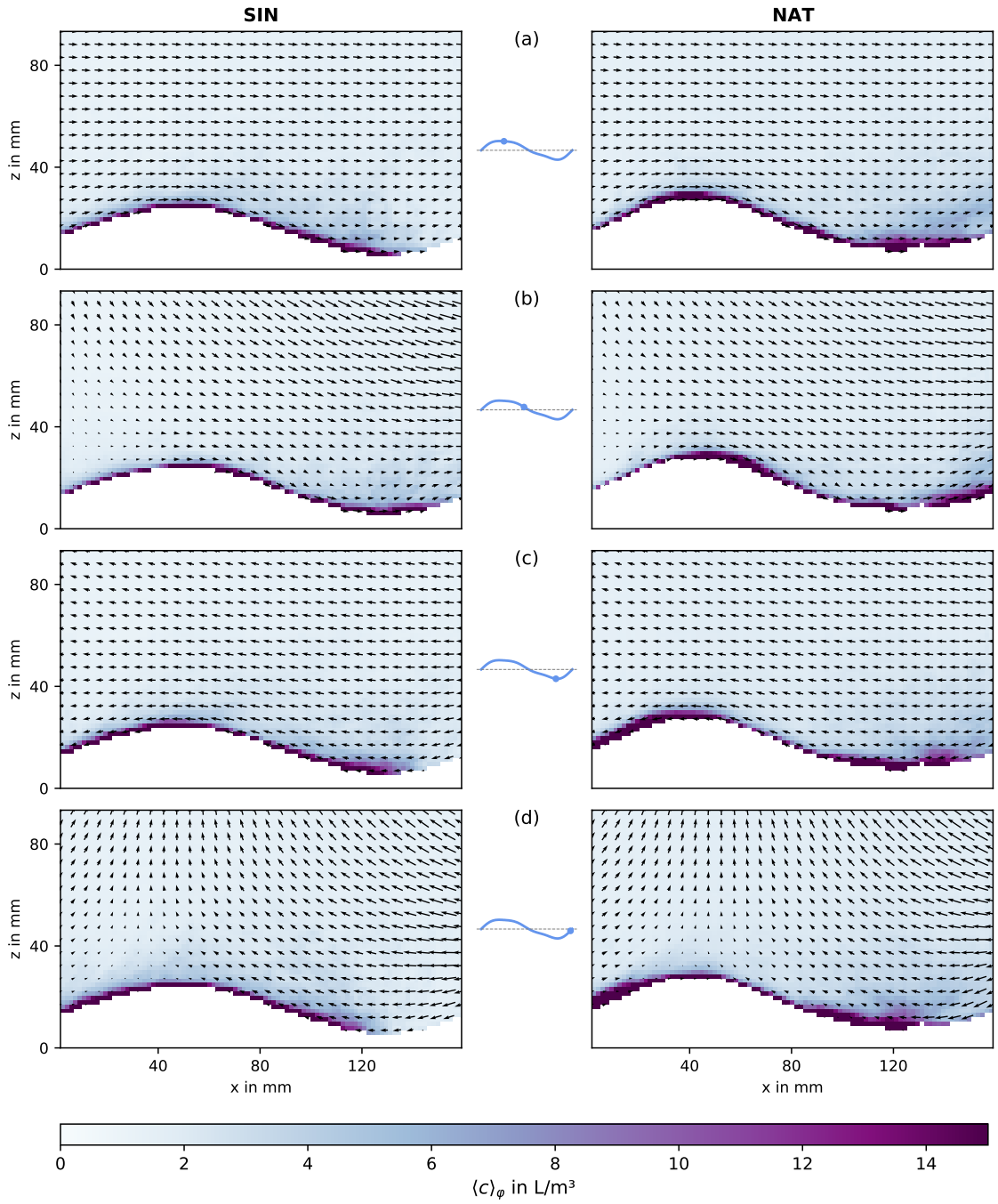

Figure A.1: Tracer distribution $\langle c \rangle_\varphi$ and velocity fields $\langle \mathbf{u} \rangle_\varphi$ for specific phases of the wave cycle under the calm wave scenario above both the sinusoidal (left) and the naturally rippled sea bed (right). The middle column plot indicates the corresponding phase's position within the wave cycle. The absolute concentration was normalised with the dye concentration $c_{\mathrm{R6G,\ Tracer}}$ of the injected tracer fluid.

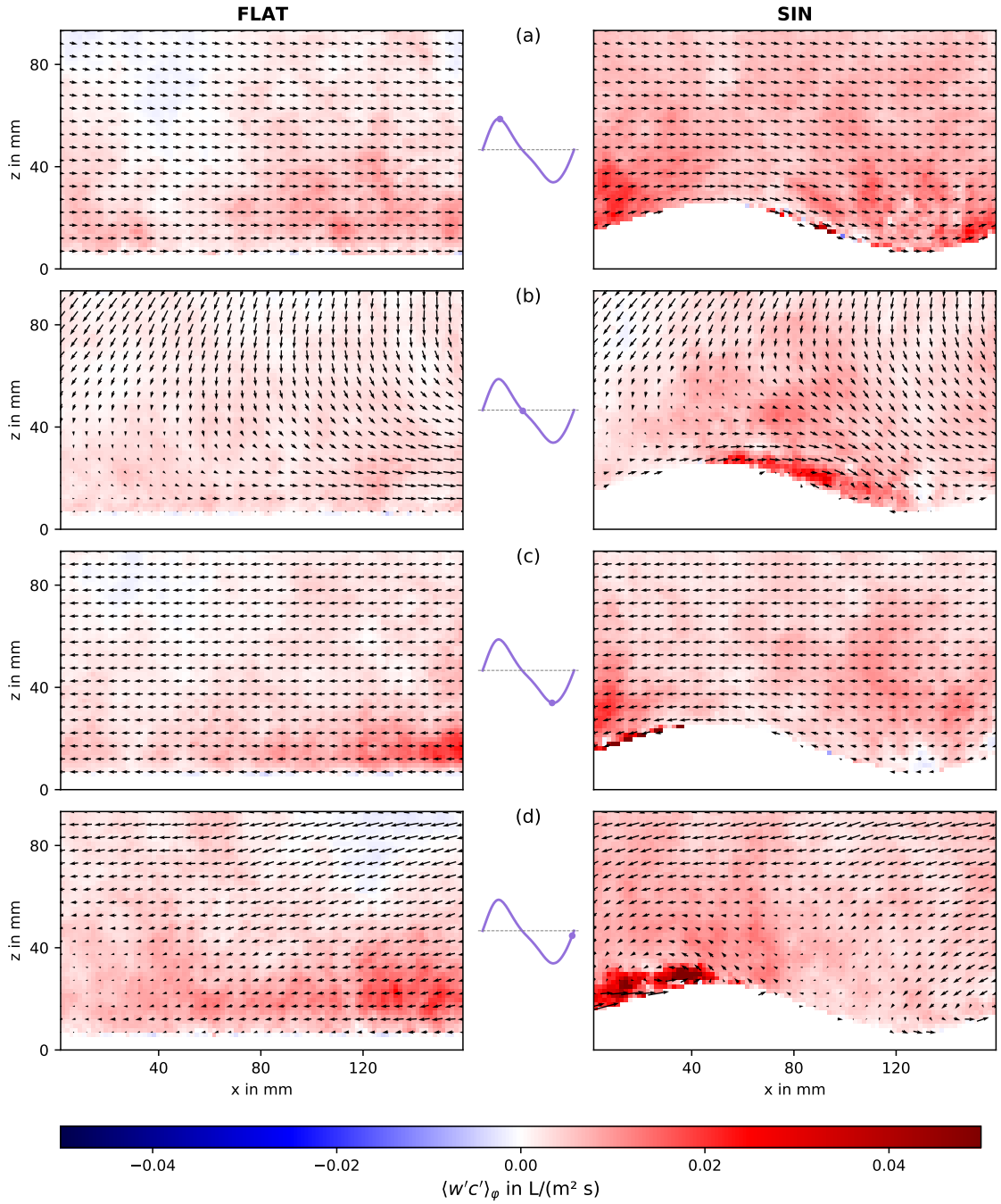

Figure A.2: Phase averaged vertical turbulent transport $\langle w'c' \rangle_\varphi$ and velocity fields $\langle \mathbf{u} \rangle_\varphi$ for specific phases of the wave cycle under the intermediate wave scenario above the flat (left) and the sinusoidal rippled sea bed (right). The middle column plot indicates the corresponding phase's position within the wave cycle.

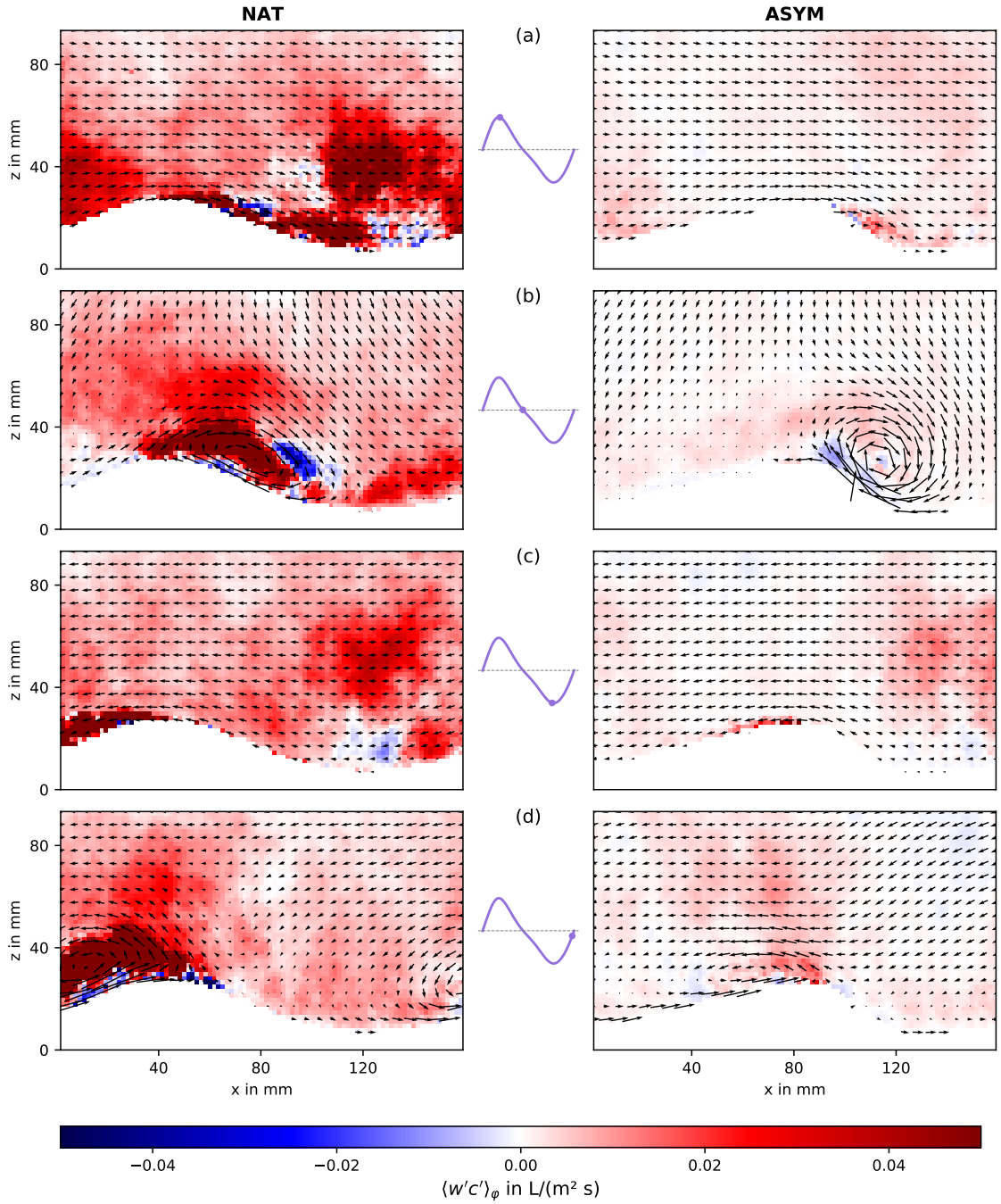

Figure A.3: Phase averaged vertical turbulent transport $\langle w'c' \rangle_\varphi$ and velocity fields $\langle \mathbf{u} \rangle_\varphi$ for specific phases of the wave cycle under the intermediate wave scenario above the symmetric (left) and the asymmetric naturally rippled sea bed (right). The middle column plot indicates the corresponding phase's position within the wave cycle.

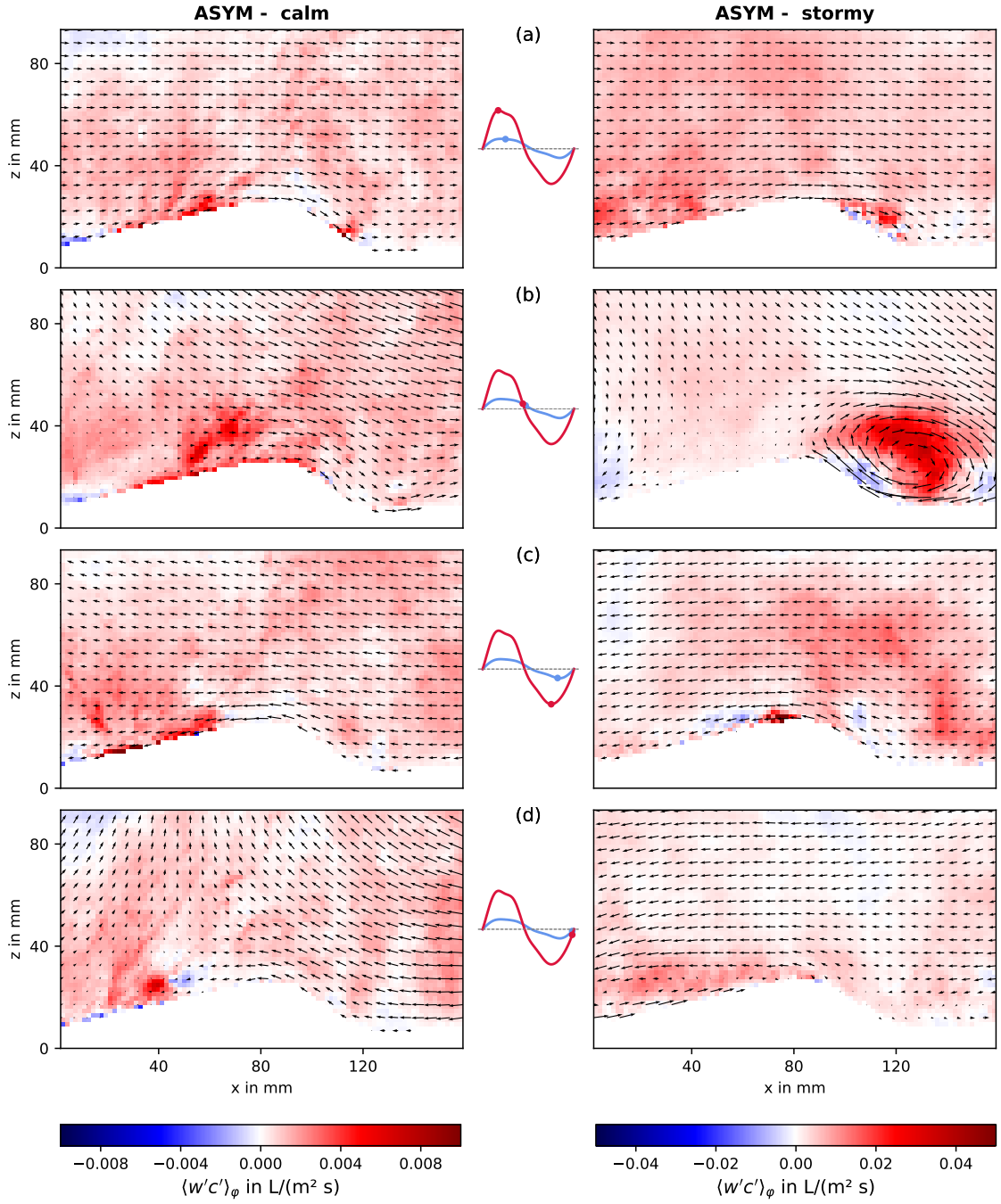

Figure A.4: Phase averaged vertical turbulent flux $\langle w'c' \rangle_\varphi$ and velocity fields $\langle \mathbf{u} \rangle_\varphi$ for specific phases of the wave cycle under the calm (left) and the stormy (right) wave scenario above the asymmetric naturally rippled sea bed. The middle column plot indicates the corresponding phase's position within the wave cycle. Note that the colorbar of the right-hand plots is scaled by a factor of 5.

Table A.1: Compilation of protocols for the measurements conducted in this study: WS - wave scenario, sf - PIV scale factor, I_p - recorded electric current of the tracer fluid pump, U_p - preset voltage of the tracer fluid pump, T_a - ambient temperature, T_w - temperature of the water in the wave tank, T_t - temperature of the injected tracer, Δt_{PIV} time difference between the PIV-double frames, f/N - aperture of the PIV- and LIF-camera, respectively, C_t - dye concentration in the tracer fluid (1 mL of dye solution contained $0.1 \cdot 10^{-3}$ g/mL Rhodamine 6G), t_E - experiment duration, t_0 start of PIV-LIF-measurement after starting the tracer fluid pump (which, in turn, corresponds to the start of the experiment), 1st to 3rd refill - instances at which the tracer fluid storage tank had to be refilled; the end of the experiment was determined by the completion of the PIV-LIF-measurement

Date	SBM	WS	sf	I_p	U_p	T_a	T_w	T_t	Δt_{PIV}	f/N	f/N	C_t	t_E	t_0	1st refill	2nd refill	3rd refill
				A	V	°C	°C	°C	s	(PIV)	(LIF)	mL/L					
29/06/2021	NAT	storm	14.3	1.41	6	22.1	18.8	19	4,000	5.6	2.8	2	21m30s	10m10s	6m	11m50s	16m30s
30/06/2021	NAT	interm.	14.3	1.35	6	22	18.9	19.1	5,000	5.6	2.8	2	-	9m55s	6m	12m	17m30s
01/07/2021	NAT	calm	14.3	1.64	6	21.1	18.9	19	15,000	5.6	2.8	2	21m30s	9m50s	6m	11m30s	17m30s
04/07/2021	ASYM	storm	14.3	1.38	6	21.6	18.9	19	4,000	5.6	2.8	6	21m30s	10m10s	5m30s	11m40s	17m50s
05/07/2021	ASYM	interm.	14.3	1.45	6	21.3	19	19	5,000	5.6	2.8	6	21m15s	9m35s	5m30s	1m20s	17m30s
07/07/2021	ASYM	calm	14.3	1.4	6	20.4			15,000	5.6	2.8	6	21m15s	10m5s	5m30s	11m30s	17m
10/07/2021	FLAT	storm	14.3	1.33	6	20.8	18.8	18.8	4,000	5.6	2.8	12	21m10s	9m40s	5m30s	11m20s	17m10s
11/07/2021	FLAT	interm.	14.3	1.22	6	21.9	19.1	19.1	5,000	5.6	2.8	12	21m10s	9m45s	5m35s	11m25s	17m15s
15/07/2021	FLAT	calm	14.3	1.51	6	22.1	20.3	20.5	15.000	5.6	2.8	2	21m20s	9m50s	5m30s	11m20s	17m15s
19/07/2021	SIN	storm	14.3	1.55	6	21.7			4,000	5.6	2.8	2	21m5s	9m45s	5m25s	11m15s	16m25s
20/07/2021	SIN	interm.	14.3	1.43	6	20.9	19.8	19.8	5,000	5.6	2.8	2	21m5s	9m42s	5m30s	11m20s	17m
21/07/2021	SIN	calm	14.3	1.42	6	20.8	19.8	19.8	15,000	5.6	2.8	2	21m	9m40s	5m20s	10m50s	16m20s

Eidesstattliche Erklärung

Ich versichere eidesstattlich durch eigenhändige Unterschrift, dass ich die Arbeit selbständig und ohne Benutzung anderer als der angegebenen Hilfsmittel angefertigt habe. Alle Stellen, die wörtlich oder sinngemäß aus Veröffentlichungen entnommen sind, habe ich durch Angaben der Herkunft kenntlich gemacht. Dies gilt auch für Zeichnungen, Skizzen, bildliche Darstellungen sowie für Quellen aus dem Internet. Ich erkläre ferner, dass ich die vorliegende Arbeit in keinem anderen Prüfungsverfahren als Prüfungsarbeit eingereicht habe oder einreichen werde. Ich weiß, dass bei Abgabe einer falschen Versicherung die Prüfung als nicht bestanden zu gelten hat.

Leonie Kandler, Rostock, 29. November 2024